

**Metamorphic evolution of lower crustal xenoliths
from the Mojave Desert, southeastern California: A
petrochronologic approach**

Kirsten E. Costello

A thesis submitted to the Department of Earth Sciences in partial fulfillment of the requirements for the degree of Master of Science (Geology).

Memorial University of Newfoundland

Abstract

A suite of lower crustal xenoliths brought to the surface in a mid-Tertiary andesitic dike in the North Piute Mountains of the Mojave Desert, southeastern California, preserve fundamental geologic information about the pre-extensional Tertiary lower crust that is otherwise inaccessible for direct study. This xenolith suite consists of aluminous, quartzose, quartzofeldspathic, and mafic rocks, interpreted to represent Paleoproterozoic crustal material that experienced granulite facies metamorphism and anatexis during Mesozoic crustal thickening.

The aluminous xenoliths, the primary focus of this study because of their mineralogy and thus suitability for thermobarometric calculations, consist of quartz + garnet + rutile + plagioclase + K-feldspar + biotite + kyanite + sillimanite, and trace zircon, monazite, and apatite. The mineralogy and microstructures are consistent with biotite dehydration melting in the kyanite stability field, significant anatectic melt loss at granulite facies conditions, and minor melt crystallization with kyanite and sillimanite upon cooling. Microstructures and mineral chemistry integrated with phase equilibria modelling suggest a P–T path with peak P of 1.2 to 1.3 GPa, and T of 850 to 870 °C, consistent with a pre-extensional Tertiary lower crustal depth of about 44 to 48 km, followed by decompression.

Inheritance and timing of metamorphism are constrained by U–Pb and Lu–Hf isotopes in zircon, and U–Pb and Sm–Nd isotopes in monazite. Zircon cores preserve Archean and Proterozoic isotopic inheritance linked to formation of the Mojave crust. Zircon rims and monazites yield late Cretaceous U–Pb dates consistent with the timing of the Laramide Orogeny and metaluminous to peraluminous granite crystallization in the Mojave. Initial ϵ_{Hf}

and ϵ_{Nd_i} values for zircon rim and monazite are consistent with growth from a melt extracted from an evolved crustal reservoir. The U-Pb dates suggest that decompression following peak P-T can most likely be attributed to crustal thinning after the Laramide Orogeny. Trace element composition of zircon and monazite provide a link between U-Pb dates and prograde garnet growth which in turn are used to establish a cohesive P-T-t history for the Mojave xenolith suite.

Acknowledgements

First and foremost, I would like to thank my supervisor Dr. Aphrodite Indares for her guidance throughout this project and for the invaluable career and life advice she has given me during my graduate degree. I consider myself extremely fortunate to have been given the opportunity to have worked with such a talented and knowledgeable individual. I also thank Dr. John Hanchar who provided the samples and input on the project.

I would also like to thank Aphrodite's research group, Susan Strowbridge, Daniela Marin Mendoza, Elliot Hoyle, and Caroline Lotout, for chatting, listening to any research issues I had, and just keeping me motivated during the Covid-19 global pandemic over weekly coffee breaks on Google Hangouts.

For the analytical aspect of this project, I would like to thank David Grant, Dylan Goudie, Wanda Aylward, Markus Wälle, and Rebecca Lam for helping me acquire data and image/map of the minerals I studied.

Many others have provided much support and encouraged me along the way including fellow MUN Earth Sciences graduate students, my friends, my family, and my fiancée. I am extremely grateful for the financial support I have received from my supervisors, the MUN School of Graduate Studies, the Alfred K. Snelgrove Memorial Scholarship, and the Buchans Scholarship Fund of ASARCO Incorporated.

Table of Contents

Abstract.....	ii
Acknowledgements	iv
List of Figures.....	vii
List of Appendices.....	x
Chapter 1: Introduction and Overview	1
1.1 Introduction.....	1
1.2 Geological Setting and Previous Work.....	3
1.3 Research Statement.....	5
1.4 Thesis Overview	7
References.....	8
Chapter 2: Metamorphic evolution of lower crustal xenoliths from the Mojave Desert, southeast California: A petrochronologic approach	14
2.1 Introduction.....	14
2.2 Regional Geology	17
2.3 Methods	20
2.3.1 Documentation of microstructures and mineral chemistry	20
2.3.2 Phase equilibria modelling.....	22
2.3.3 Zircon and monazite analyses	24
2.4 Results.....	26
2.4.1 Metamorphic microstructures revealed by optical microscopy and SEM–MLA	26
2.4.2 Metamorphic microstructures revealed by xCLent CL maps of aluminosilicates ...	33
2.4.3. Insights on anatexis based on microstructures	35
2.4.4 Mineral chemistry	38
2.4.5 Phase equilibria modelling.....	44
2.4.6 U–Pb and Hf in zircon.....	53
2.4.7 U–Pb and Nd in monazite	61
2.4.8 Trace elements in zircon and monazite	64
2.5 Discussion.....	68
2.5.1 P–T path and melt composition predictions.....	68
2.5.2 Inheritance and Metamorphic Ages for the Mojave Xenoliths	79

2.6 Conclusions.....	83
References.....	85
Chapter 3: Summary and conclusions	97
References.....	99

List of Figures

- Figure 1.** (a) Map of the North American geological provinces after Buchan et al., 2000. (b) Geologic map of the Old Woman–Piute Mountain Range modified from Fisher et al. (2017) Abbreviations: NP – North Piute pluton, EP – East Piute pluton, PR – Painted Rock granite, OW – Old Woman granodiorite, LD – Lazy Daisy pluton, SW – Sweetwater Wash pluton. . **19**
- Figure 2.** Modal percent of minerals given by SEM–MLA analysis greater than 1% in the rock represented on normalized bar diagrams..... **30**
- Figure 3.** False coloured SEM–MLA thin section maps for samples XJ-150, XJ-210, XJ-21, XS-41a, and NPX-17-03A..... **31**
- Figure 4.** Petrographic and SEM–MLA images highlighting significant microstructures. Legend for false colours on SEM–MLA images are found in figure 3. (a): rounded quartz domain containing blebby interstitial K-feldspar and late carbonate within matrix plagioclase from XJ-150. (b): Large resorbed kyanite blades adjacent to smaller prismatic sillimanite in a quartzofeldspathic matrix from XJ-21. (c): Prismatic sillimanite surrounded by K-feldspar interstitial to quartz from XJ-21. (d): Small prismatic sillimanite inclusions within garnet in XJ-41a. (e): Bands of amalgamated kyanite oriented perpendicular to individual grain orientation from NPX-17-03A. (f): intergrowth of quartz and plagioclase within K-feldspar matrix from NPX-17-03A. (g): heavily resorbed kyanite crystal surrounded by a rim of K-feldspar XS-41a. (h): garnet proximal to dike contact with thick coronas of biotite, magnetite, and chlorite from XJ-150..... **32**
- Figure 5.** Cathodoluminescence (CL) maps of aluminosilicate phases. (a): Resorbed kyanite separated from quartz (blue) by a very low CL rim of K-feldspar. Internal structure of kyanite lacks distinct core and rim boundaries and CL intensities are mottled/smeared. (b): Grains of kyanite amalgamated into an elongated band associated with garnet and rutile (black), and quartz (blue). Individual grains have a mottled/smeared CL pattern. (c): Zoned kyanite crystal (upper left) adjacent to a kyanite where zoning is less defined. The zoned crystal preserves a high-CL resorbed core (orange) with a low-CL rim overgrowth (light blue) surrounded by K-feldspar (black) interstitial to quartz (dark blue). (d): Prismatic sillimanite (shades of blue)

surrounded by K-feldspar (blue) interstitial to quartz (green). Sillimanite preserves concentric growth zoning revealed in CL by different shaded ellipses of blue and green.	34
Figure 6. Illustration of kyanite CL map from sample NPX-17-03A demonstrating the growth history by means of three metamorphic reactions.	37
Figure 7. Average composition of garnet in end member percentages for each sample plotted on a $X_{\text{alm}}-X_{\text{grs}}-X_{\text{prp}}$ ternary diagram.	39
Figure 8. Examples garnet end-member zoning profiles with their corresponding SEM-MLA images obtained from SEM.	40
Figure 9. Scatter plot comparing biotite compositions in matrix, near garnet, and included within garnet in terms of X_{Mg} vs. Ti (per 11 oxygens).	41
Figure 10. Average feldspar compositions plotted on a An-Or-Ab ternary diagram. K-feldspar compositions were grouped based on their textural setting which is directly related to having either relatively high (97-99%), moderate (70-86%), or low (53-70%) orthoclase Or content. Plagioclase compositions display less variation and therefore were averaged per sample with exception of nearly pure albite compositions which were averaged separately. .	42
Figure 11. P-T pseudosections calculated using the bulk composition of each sample.	46
Figure 12. Isomodes and isopleths overlain on the P-T pseudosections of Figure 11.	48
Figure 13. Pseudosections with aluminosilicate isomodes, grossular, and X_{Fe} in garnet isopleths calculated using the melt-reintegrated composition for each sample.	51
Figure 14. CL images of characteristic zircon grains	54
Figure 15. U-Pb isotope diagrams for zircon rims in xenoliths XC-9F, XJ-9, and XJ-150. ..	58
Figure 16: ϵ_{Hf} vs. time diagram for Concordant zircon rim.	59
Figure 17. Concordia diagrams for xenolith zircon cores	61
Figure 18: BSE images of characteristic monazite grains	62
Figure 19. Monazite U-Pb isotopic ratios plotted on a Concordia diagram.	63
Figure 20. Initial ϵ_{Nd} vs. time plot for monazite.	64
Figure 21. Chondrite-normalized REE plots for zircon rim and core.	67
Figure 22. Monazite REE data from samples XC-9F and XJ-60 plotted on a chondrite-normalized diagram using chondrite values from Anders and Grevasse (1990).	68
Figure 23. Predicted P-T paths for each sample overlain with melt-reintegrated pseudosections.	71

Figure 24. K ₂ O vs. Na ₂ O binary diagram for modelled anatectic melts and average Cretaceous metaluminous and peraluminous granite compositions from Miller and Wooden (1994). Oxides are in wt%.	75
Figure 25. Na ₂ O+CaO vs. K ₂ O vs. FeO+MgO diagram in wt % oxides.....	76
Figure 26. SiO ₂ wt. % oxide vs. ASI (alumina saturation index) binary diagram modified from Frost and Frost (2008).....	77
Figure 27. Normative alkali feldspar (orthoclase) vs. quartz vs. plagioclase ternary diagram with granitoid classification of plutonic rocks from International Union of Geological Sciences (IUGS). Normative mineralogy is calculated using scheme from Kelsey (1965).....	78
Figure 28. Zircon core ²⁰⁷ Pb/ ²⁰⁶ Pb dates plotted in age-order compared with documented Archean-Proterozoic events in the Mojave. Weighted mean dates shown in boxes are calculated from coloured data points and overlap with major geologic events known in the Mojave that occurred from the Precambrian to the Neoproterozoic.	82

List of Appendices

Appendices are provided in a separate document.

Appendix I: Petrography

Appendix II: SEM–MLA maps

Appendix III: Modal mineralogy of entire thin section from SEM–MLA

Appendix IV: Modal mineralogy of the xenolith area in thin section from SEM–MLA

Appendix V: Cathodoluminescence and EPMA X-ray maps of aluminosilicate minerals

Appendix VI: Electron microprobe analyzer standards

Appendix VII: Mineral chemistry from EPMA*

Appendix VIII: Xenolith bulk composition calculation*

Appendix IX: Remarks on THERMOCALC database

Appendix X: CL images of zircon

Appendix XI: BSE images of monazite

Appendix XII: Details on laser ablation split stream

Appendix XIII: Laser ablation split stream analytical standards*

Appendix XIV: Zircon U–Pb data from LASS*

Appendix XV: Zircon Lu–Hf data from LASS*

Appendix XVI: Zircon major element data from EPMA*

Appendix XVII: Zircon trace element data from LA-ICP-MS*

Appendix XVIII: Monazite U–Pb data from LASS*

Appendix XIX: Monazite Sm–Nd data from LASS*

Appendix XX: Monazite major element data from EPMA*

Appendix XXI: Monazite trace element data from LA-ICP-MS*

*Contents of these appendices are provided in a separate folder

Chapter 1: Introduction and Overview

1.1 Introduction

Anatexis in the lower crust and melt segregation to higher levels is a significant driver for crustal evolution (Vielzeuf et al., 1990; Brown, 2010). The lower crust largely consists of granulite facies metamorphic rocks that are only directly accessible as either; 1) surface outcrops in exhumed granulite terrains or 2) small fragments of rock called xenoliths which are carried upwards from great depths in magma chambers and volcanic conduits (Rudnick & Taylor, 1987; Rudnick, 1992; Rudnick & Fountain, 1995). A suite of lower crustal xenoliths from the Mojave Desert consists of quartzose, quartzofeldspathic, aluminous, and mafic rocks and preserves peak granulite facies metamorphic assemblages, evidence of lower crustal anatexis, and isotopic signatures that may be linked to Cretaceous metamorphism and Proterozoic inheritance. This xenolith suite is thought to provide insight into the geologic history and the pressure, temperature and time P–T–t evolution of the pre-Tertiary extensional lower Mojave Province crust otherwise inaccessible for direct observation (Miller et al., 1992; Hancher et al., 1994; Miller & Wooden, 1994).

In lower crustal, high grade metamorphic environments, anatectic melt is typically produced under fluid-absent conditions, by means of muscovite and biotite dehydration reactions in aluminous rocks (Thompson, 1982; Vielzeuf & Holloway, 1988; Spear et al., 1999; White & Powell, 2002). At upper amphibolite to lower granulite-facies, muscovite commonly breaks down by the following discontinuous, melt-producing reaction:



If the temperature of the system continues to increase once muscovite is consumed, biotite begins to break down by means of the following continuous melting reaction:



If more than 7% of melt is produced from these reactions, there is a high potential for melt to escape and segregate into the upper crust (Brown, 2007; 2010). Any remaining melt in the rock after melt loss would eventually be consumed by the reverse of the biotite dehydration reaction leading to the formation of new biotite, kyanite or sillimanite (depending on the depth of melt crystallisation), and ‘pseudomorphs’ of melt composed of quartz and feldspar that imitate the behaviour of melt interacting with solid grains (Brown, 2002).

The purpose of this study is to decipher the metamorphic history of the xenolith suite and constrain ages related to inheritance, melting, and metamorphism. This encompasses P–T constraints, modelled anatectic melting trends, inheritance of zircon cores, the timing of metamorphism based on U–Pb and trace elements from zircon rim and monazite, and the hypothesized source-melt relationship with several peraluminous granites in the Mojave Desert (Miller et al., 1992). The P–T and melting history is constrained using only the aluminous xenoliths because they contain P–T sensitive mineral assemblages and are the most fertile with respect to melting (Spear et al., 1999). Additionally, aluminous rocks preserve an array of unique microstructures revealed by modern imaging techniques that may be linked to anatectic melt production, loss, and crystallization. These microstructures, along with quantitative mineral chemistry data are interpreted within the framework of P–T pseudosection phase diagrams calculated for specific bulk rock compositions, in terms of the prograde history, peak P–T, the retrograde path, melt crystallization, and anatectic melting

trends. Isotopic compositions were measured using Laser Ablation Split Stream (LASS) Inductively Coupled Plasma Mass Spectrometry (ICP-MS) to simultaneously determine U–Pb and Lu–Hf in zircon, U–Pb and Sm–Nd in monazite in the same ablation volumes, and trace element compositions in both zircon and monazite, from aluminous and quartzose xenoliths. U–Pb dates are constrained to either inheritance or melting and metamorphism. Initial ϵ_{Hf} and ϵ_{Nd} are compared with the ϵ_{Hf} and ϵ_{Nd} values from nearby Cretaceous peraluminous granites in the Old Woman Mountains (OWM) (i.e., the Sweetwater Wash pluton) (Fisher et al., 2017) to determine if a source-melt relationship can be established.

1.2 Geological Setting and Previous Work

The Mojave Province formed in the Paleoproterozoic along the edge of ancient supercontinent Laurentia in a marine arc environment overlying enriched mantle. The Mojave crust was further build as a result of the Ivanpah orogeny and widespread Paleoproterozoic (1.79 – 1.64 Ga) magmatism of potassic and intermediate to felsic plutons (Barth et al., 2000; Duebendorfer, 2015). Once the Mojave crust was stable several other magmatic events occur throughout the remainder of the Proterozoic. Those include granitoid magmatism between 1.43 and 1.40 Ga (Anderson & Bender, 1989), anorthosite–mangerite–charnockite–granite (AMCG) suite emplacement between 1.21 and 1.18 Ga (McLelland et al., 2010), diabase dike intrusions around 1.09 Ga (Barth et al., 2001; Bright et al., 2014), and the onset of crustal extension which proceeded into the Cambrian (Wooden et al., 2012). From the Cambrian to the Triassic period, the Mojave was a part of a passive margin and thick sedimentary sequences were deposited (Barth et al., 2009). A change in tectonic regime due to the breakup of supercontinent Pangea resulted in crustal thickening, magmatism, and orogenesis throughout the Mesozoic. In the Tertiary, basin and range tectonism initiated due to the onset

of the San Andres transform fault resulting in voluminous intrusions of felsic and mafic magmas, dike swarms, and crustal extension.

The Mojave lower crustal xenolith suite was first discovered and documented by Staude (1987) and was further studied by Hanchar et al (1994). This study by Hanchar et al (1994) provided a comprehensive background into the classification, metamorphism, petrogenesis, and the origin of the xenolith suite. The xenoliths were divided into four main categories based on their primary mineral assemblage. Over 50% of the xenoliths fall into the quartzofeldspathic category, followed by 25% mafic, 13% quartzose, and 10% aluminous. Based on rock types, the protoliths for the xenoliths are inferred to include sedimentary lithologies (i.e., quartz arenites, pelites, and greywackes), intermediate to mafic igneous rocks, and quartzofeldspathic rocks (i.e., psammites and felsic intrusive rocks). The whole-rock geochemistry of the xenoliths was compared with the estimates of global lower crustal compositions presented by Weaver and Tarney (1984), Taylor and McLennan (1985), and Shaw et al. (1986). Results from this show that the SiO₂ and mafic content is consistent with the global lower crust estimate. The xenolith compositions differ in that they are more peraluminous, have lower Mg#, and higher TiO₂, Nb, Zr, Hf, light and heavy REE, Y, Cr, and Ni (Hanchar et al., 1994). These geochemical differences indicate that the Mojave lower crust reflects a strong metasedimentary and residual heritage relative to the lower crustal estimates from Weaver and Tarney (1984), Taylor and McLennan (1985), and Shaw et al. (1986). Using conventional thermobarometry methods, Hanchar et al. (1994) proposed a preliminary *P-T* estimate for peak metamorphism of 1.0–1.2 GPa and 750–800 °C. These estimates suggest that peak metamorphism and anatexis occurred before the Mojave lower crust thinned to < 30 km in the Tertiary period. The results from Rb–Sr, Sm–Nd, U–Pb, and Pb isotopic analysis of

the xenoliths demonstrate high $^{87}\text{Sr}/^{86}\text{Sr}$, low $^{143}\text{Nd}/^{144}\text{Nd}$, and Pb/Pb ages of 1.7 Ga consistent with the xenolith protoliths originating in the Proterozoic Mojave Crust (Hanchar et al., 1994). Unreasonably old Sr and Nd model ages suggests a recent, late Phanerozoic disturbance in parent and daughter isotopic ratios. The most likely interpretation for this disturbance is that the lower crust underwent widespread melting leading to granitoid emplacement in the Mesozoic (Miller et al., 1992; Hanchar et al., 1994). An alternate interpretation from Hanchar et al. (1994) is isotopic disturbance was caused by felsic and basaltic volcanism in the mid-Tertiary.

1.3 Research Statement

The purpose of this research is to elucidate the metamorphic evolution of the eastern Mojave xenolith suite through the interpretation of metamorphic microstructures, mineral chemistry, phase equilibria modelling, isotopes, and trace elements. Metamorphic conditions are constrained using microstructures and mineral chemistry integrated with phase equilibria modelling to depict the prograde, retrograde, and anatectic melting history on a P–T trajectory. The analysis of Lu–Hf and U–Pb isotopes in zircon and Sm–Nd and U–Pb in monazite allows for the age and crustal source of metamorphism and inheritance to be constrained. Trace element concentrations in metamorphic zircon rim and monazite provide a link between predicted metamorphic conditions based on garnet behavior and measured U–Pb ages to constrain the P–T–t evolution of the eastern Mojave xenolith suite.

The xenolith suite may record significant crustal melting in the Mojave lower crust because of their good preservation of peak granulite facies and residual mineralogy, microstructures related to partial melt production, loss, and crystallization, and lack of

retrograde assemblages (Sawyer, 2001; Brown, 2002; White and Powell., 2002; Holness and Sawyer, 2008; Vernon, 2011). Xenoliths are hypothesized to represent the residue of a crustal melt which produced several Cretaceous peraluminous and metaluminous granites in the Old Woman – North Piute mountain range in the Mojave Desert (Miller et al., 1992; Hanchar et al., 1994). An important component of this study is to build onto this hypothesis by determining the timing of lower crustal anatexis and crust formation ages (i.e., ϵ_{Nd} and ϵ_{Hf}) for the xenoliths and comparing with that of the Cretaceous granites (Fisher et al., 2017) to better constrain a source-melt relationship.

Metamorphic microstructures critical for P–T path interpretation were documented using traditional optical petrography, scanning electron microscope – mineral liberation analysis (SEM–MLA) mapping of entire thin sections, and CL mapping of aluminosilicate minerals, kyanite and sillimanite. Bulk compositions for each sample were calculated using modal mineralogy obtained from SEM–MLA mapping and quantitative mineral chemistry measured using an electron probe microanalyzer (EPMA) (Indares et al., 2008). Phase equilibria modelling and the construction of P–T pseudosection phase diagrams was done using THERMOCALC 3.33 software (Holland & Powell, 2011). Isotopes and trace element concentrations were measured in zircon and monazite using Laser ablation inductively coupled plasma mass spectrometry (LA-ICP-MS). Compositions of two isotopic systems (i.e. Lu–Hf and U–Pb in zircon and Sm–Nd and U–Pb in monazite) were simultaneously collected with a laser ablation split stream (LASS) technique using a Thermo-Finnigan Element XR inductively coupled plasma mass spectrometry (ICP-MS) and a Thermo-Finnigan Neptune Multicollector ICP-MS. Isotopic and trace element data was reduced using Iolite software (Paton et al., 2011). All imaging, mapping and analytical measurements were done at either

the Earth Resource Research and Analysis Facility (TERRA) or the Micro Analysis Facility (MAF-IIC) at Memorial University of Newfoundland.

1.4 Thesis Overview

This thesis is comprised of three chapters. Chapter 1 introduces the project, previous work, and a brief research statement. Chapter 2 is a manuscript-style chapter which will be submitted for publication at a later time in an international peer-reviewed scientific journal under the title “Metamorphic evolution of lower crustal xenoliths from the Mojave Desert, southeast California: a petrochronologic approach”. The purpose of this chapter is to constrain the P–T–t path recorded by the aluminous xenoliths of the Mojave suite using microstructures, mineral chemistry, U–Pb dates, and trace element concentrations of zircon and monazite integrated with phase equilibria modelling techniques. Initial ϵ_{Hf} from zircon and ϵ_{Nd} from monazite are linked with significant geological events in the Mojave in addition to U–Pb dates to fit the metamorphic history of the xenoliths into regional context. Lastly, chapter 3 provides a summary and conclusion of the thesis. The full set of data is available in the Appendices.

References

- Anderson, J. L., & Bender, E. E. (1989). Nature and origin of Proterozoic A-type granitic magmatism in the southwestern United States of America. *Lithos*, 23(1–2), 19–52. [https://doi.org/10.1016/0024-4937\(89\)90021-2](https://doi.org/10.1016/0024-4937(89)90021-2)
- Barth, A. P., Wooden, J. L., & Coleman, D. S. (2001). SHRIMP-RG U-Pb Zircon Geochronology of Mesoproterozoic Metamorphism and Plutonism in the Southwesternmost United States. *Journal of Geology*, 109(3), 319–327.
- Barth, A. P., Wooden, J. L., Coleman, D. S., & Vogel, M. B. (2009). Assembling and disassembling California: A zircon and monazite geochronologic framework for proterozoic crustal evolution in southern California. *Journal of Geology*, 117(3), 221–239. <https://doi.org/10.1086/597515>
- Barth, P., Wooden, L., Coleman, D. S., & Fanning, C. M. (2000). Geochronology of the Proterozoic basement of the southwesternmost North America, and the origin and evolution of the Mojave crustal province. *Tectonics*. 19(4), 616–629
- Bright, R.M., Amato, J.M., Denyszyn, S.W. and Ernst, R.E., 2014. U-Pb geochronology of 1.1 Ga diabase in the southwestern United States: Testing models for the origin of a post-Grenville large igneous province. *Lithosphere*, 6(3), pp.135-156.
- Brown, M. (2002) Retrograde processes in migmatites and granulites revisited. *Journal of Metamorphic Geology*, 20(1), 25–40. <https://doi.org/10.1046/j.0263-4929.2001.00362.x>.

- Brown, M. (2007) Crustal melting and melt extraction, ascent, and emplacement in orogens: Mechanisms and consequences. *Journal of the Geological Society*, 164(4), 709–730.
<https://doi.org/10.1144/0016-76492006-171>.
- Brown, M. (2010) Melting of the continental crust during orogenesis: The thermal, rheological, and compositional consequences of melt transport from lower to upper continental crust. *Canadian Journal of Earth Sciences*, 47(5), 655–694.
<https://doi.org/10.1139/E09-057>.
- Duebendorfer, E. M. (2015). Refining the early history of the mojave-yavapai boundary zone: Rifting versus arc accretion as mechanisms for paleoproterozoic crustal growth in southwestern laurentia. *Journal of Geology*, 123(1), 21–38.
<https://doi.org/10.1086/678950>
- Fisher, C. M., Hanchar, J. M., Miller, C. F., Phillips, S., Vervoort, J. D., and Whitehouse, M. J.(2017) Combining Nd isotopes in monazite and Hf isotopes in zircon to understand complex open-system processes in granitic magmas. *Geology*, 45(3), 267–270.
<https://doi.org/10.1130/G38458.1>.
- Hanchar, J. M., Miller, C. F., Wooden, J. L., Bennett, V. C., and Staude, J. M. G. (1994) Evidence from xenoliths for a dynamic lower crust, eastern mojave desert, California. *Journal of Petrology*, 35(5), 1377–1415. <https://doi.org/10.1093/petrology/35.5.1377>.
- Holland, T. J. B., and Powell, R. (2011) An improved and extended internally consistent thermodynamic dataset for phases of petrological interest, involving a new equation of state for solids. *Journal of Metamorphic Geology*, 29(3), 333–383.
<https://doi.org/10.1111/j.1525-1314.2010.00923.x>

Holness, M. B., and Sawyer, E. W. (2008) On the pseudomorphing of melt-filled pores during the crystallization of migmatites. *Journal of Petrology*, 49(7), 1343–1363.

<https://doi.org/10.1093/petrology/egn028>.

Indares, A., White, R. W., and Powell, R. (2008) Phase equilibria modelling of kyanite-bearing anatectic paragneisses from the central Grenville Province. *Journal of*

Metamorphic Geology, 26(8), 815–836. <https://doi.org/10.1111/j.1525->

[1314.2008.00788.x](https://doi.org/10.1111/j.1525-1314.2008.00788.x).

McLelland, J. M., Selleck, B. W., Hamilton, M. A., & Bickford, M. E. (2010). Late- to post-tectonic setting of some major proterozoic anorthosite - mangerite - charnockite - granite (AMCG) suites. *Canadian Mineralogist*, 48(4), 729–750.

<https://doi.org/10.3749/canmin.48.4.729>

Miller, C. F., Hanchar, J. M., Wooden, J. L., Bennett, V. C., Harrison, T. M., Wark, D. A., and Foster, D. A. (1992) Source region of a granite batholith: Evidence from lower crustal xenoliths and inherited accessory minerals. *Special Paper of the Geological Society of America*, 272, 49–62. <https://doi.org/10.1130/SPE272-p49>.

Miller, C. F., and Wooden, J. L. (1994) Anatexis, hybridization, and the modification of ancient crust: Mesozoic plutonism in the Old Woman Mountains area, California. *Lithos*, 32(1–2), 111–133. [https://doi.org/10.1016/0024-4937\(94\)90025-6](https://doi.org/10.1016/0024-4937(94)90025-6).

Paton, C., Hellstrom, J., Paul, B., Woodhead, J., and Hergt, J. (2011) Iolite: Freeware for the visualisation and processing of mass spectrometric data. *Journal of Analytical Atomic Spectrometry*, 26(12), 2508–2518. <https://doi.org/10.1039/c1ja10172b>.

- Rudnick, R. L. (1992) Xenoliths—samples of the lower continental crust. In: Fountain, D. M., Arculus, R. J., & Kay, R. W.(eds.) *The Continental Lower Crust*. New York: Elsevier, pp. 269-316.
- Rudnick, R. L., & Taylor, S. R. (1987). The composition and petrogenesis of the lower crust: A xenolith study. *Journal of Geophysical Research: Solid Earth*, 92(B13), 13981–14005.
<https://doi.org/10.1029/jb092ib13p13981>
- Rudnick, R. L., and Fountain, D. M. (1995) Nature and composition of the continental crust: a lower crustal perspective. *Reviews of Geophysics*, 33(3), 267–309.
<https://doi.org/10.1029/95rg01302>.
- Sawyer, E. W. (2001) Melt segregation in the continental crust: Distribution and movement of melt in anatectic rocks. *Journal of Metamorphic Geology*, 19(3), 291–309.
<https://doi.org/10.1046/j.0263-4929.2000.00312.x>.
- Shaw, D. M., Cramer, J. J., Higgins, M. D., and Truscott, M. G. (1986) Composition of the Canadian Precambrian shield and the continental crust of the earth. In: Dawson, J. B., Carswell, D. A., Hall, J., & Wedepohl, K. H. (eds.) *The Nature of the Lower Continental Crust. Geological Society Special Publication*, 24, 257-282.
- Spear, F. S., Kohn, M. J., and Cheney, J. T. (1999) P-T paths from anatectic pelites. *Contributions to Mineralogy and Petrology*, 134(1), 17–32.
<https://doi.org/10.1007/s004100050466>.
- Staude, J. M. G., (1987). Lower crustal xenoliths from a mixed magma dike, Piute Mountains, southeastern California. B. S. Thesis, Pomona College, Claremont, CA, 96 pp. Taylor,

S. R., and McLennan, S. M. (1985) *The Continental Crust: Its Composition and Evolution*. Boston, MA: Blackwell Scientific, 312 pp.

Taylor, S R, & McLennan, S M. The continental crust: Its composition and evolution. United States.

Thompson, A. B. (1982) Dehydration melting of pelitic rocks and the generation of H₂O-undersaturated granitic liquids. *American Journal of Science*, (Vol. 282, Issue 10, pp. 1567–1595). <https://doi.org/10.2475/ajs.282.10.1567>.

Vernon, R. H. (2011) Microstructures of melt-bearing regional metamorphic rocks. *Memoir of the Geological Society of America*, 207(01), 1–11. [https://doi.org/10.1130/2011.1207\(01\)](https://doi.org/10.1130/2011.1207(01)).

Vielzeuf, D., Clemens, J. D., Pin, C., & Moinet, E. (1990) Granites, granulites, and crustal differentiation. In D. Vielzeuf & PH. Vidal (Ed.) *Granulites and crutsal evolution*. Kluwer Academic Publishers.

Vielzeuf, D., and Holloway, J. R. (1988) Experimental determination of the fluid-absent melting relations in the pelitic system. *Contributions to Mineralogy and Petrology*, 98(3), 257–276. <https://doi.org/10.1007/bf00375178>.

Weaver, B. L., and Tarney, J. (1984) Empirical approach to estimating the composition of the continental crust. *Nature*, 310, 575-577.

White, R. W., and Powell, R. (2002) Melt loss and the preservation of granulite facies mineral assemblages. *Journal of Metamorphic Geology*, 20(7), 621–632.

<https://doi.org/10.1046/j.1525-1314.2002.00206.x>.

White, R. W., Powell, R., and Clarke, G. L. (2002) The interpretation of reaction textures in Fe-rich metapelitic granulites of the Musgrave Block, Central Australia: Constraints from mineral equilibria calculations in the system. *Journal of Metamorphic Geology*, 20(1), 41–55. <https://doi.org/10.1046/j.0263-4929.2001.00349.x>.

Wooden, J. L., Barth, A. P., & Mueller, P. A. (2012). Crustal growth and tectonic evolution of the Mojave crustal province: Insights from hafnium isotope systematics in zircons. *Lithosphere*, 5(1), 17–28. <https://doi.org/10.1130/L218.1>

Chapter 2: Metamorphic evolution of lower crustal xenoliths from the Mojave Desert, southeast California: A petrochronologic approach

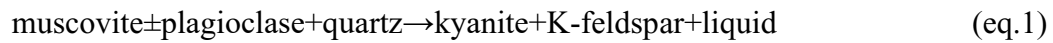
2.1 Introduction

Partial melting and extraction of melt in the lower continental crust is a critical process for crustal evolution (Vielzeuf et al., 1990; Brown, 2010). The lower crust is considered to consist of granulite facies metamorphic rocks (Rudnick & Fountain, 1995). These deep crustal rocks are directly accessible as either: 1) surface outcrops in exhumed granulite terrains; or 2) xenoliths which are carried upwards from great depths in magma chambers and volcanic conduits (Rudnick & Taylor, 1987; Rudnick, 1992; Rudnick & Fountain, 1995). A suite of lower crustal xenoliths from the Mojave Desert in southeastern California preserves evidence for partial melting under granulite facies metamorphic conditions and contain zircon and monazite that may be linked to metamorphism and isotopic inheritance. Such evidence in turn provides insight into the geologic history and the P–T–t evolution of the pre-Tertiary extensional lower Mojave crust otherwise inaccessible for direct observation.

The xenoliths were collected from an east-west trending Miocene dike in the Old Woman – Piute Mountain Range in the eastern Mojave Desert in southeastern California (Hancher et al., 1994). This region is geologically a part of the Basin and Range Province of the southwestern United States. The suite consists of four types of rocks: 1) quartz-rich; 2) quartzofeldspathic; 3) metapelitic (aluminous); and 4) mafic. Quartzofeldspathic xenoliths are the most abundant comprising of >50% of the whole suite followed by 25% mafic, 13% quartzose, 10% aluminous rocks (Hancher et al., 1994). The compositional variability of the North Piute xenolith suite reflects the initial protolith(s) in the lower crust, the varying degrees

of melt loss during an inferred Mesozoic anatectic event and any sample bias from the available samples that were exposed in the dyke and thus collected (Hanchar et al., 1994). The aluminous xenoliths have been hypothesized to be the residual counterpart (restite) of several strongly peraluminous Cretaceous plutons in the region, including the Sweetwater Wash (SWP), North Piute (NPP), and Painted Rock (PRP) plutons (Hanchar et al., 1994; Miller and Wooden, 1994).

Aluminous, lower crustal granulites contain a predominantly anhydrous mineral assemblage due to muscovite and biotite dehydration melting at fluid absent conditions (Thompson, 1982; Vielzeuf and Holloway, 1988; Spear et al., 1999; White and Powell, 2002). At high pressure conditions this melting occurs by reactions such as:



and, at higher temperatures:



If metamorphism occurs in a dynamic environment, at melt proportions above 5 to 7% (Rosenberg and Handy, 2005), melt is expected to migrate into the upper crust forming granitic plutons and leaving a refractory lower crust (Brown, 2010). During subsequent cooling, any remaining melt in the rock would eventually be consumed by the reverse of the biotite dehydration reaction leading to the formation of new biotite, aluminum silicate, and melt ‘pseudomorphs’ of quartz and feldspar that imitate the habit of melt interacting with solid grains (Brown, 2002).

The purpose of this study is to depict the metamorphic evolution of the xenolith suite and constrain inheritance and the timing of metamorphism. This encompassed pressure and temperature P–T constraints, modelled anatexis melting trends, and the interpretation of U–Pb dates, trace elements and initial ϵ_{Hf} from zircon and ϵ_{Nd} from monazite. The aluminous xenoliths in the suite are most useful in constraining the P–T and melting history because they contain P–T sensitive mineral assemblages, the most fertile with respect to melting (Spear et al., 1999), and preserve microstructures linked to anatexis melt production, loss, and crystallization. Microstructures revealed by modern imaging techniques (e.g., back-scattered electron [BSE] and cathodoluminescence [CL]), along with quantitative mineral chemistry are integrated with phase equilibria modelling techniques. Results are interpreted in the framework of P–T pseudosection diagrams to predict the prograde history, peak P–T, the retrograde path, melt crystallization, and modelled anatexis melting trends for the xenolith suite. Isotopes and trace elements were measured in zircon and monazite from aluminous, quartzose, and quartzofeldspathic xenoliths using laser ablation inductively coupled plasma mass spectrometry (LA–ICP–MS). The isotope systems U–Pb and Lu–Hf in zircon and U–Pb and Sm–Nd in monazite were simultaneously measured with laser ablation split stream (LASS). U–Pb dates from inherited zircon cores reflect orogenic and magmatic events occurring from the Archean to the Mesoproterozoic. The timing of melting and metamorphism are constrained by U–Pb dates, from zircon rims and monazite and HREE patterns of zircon. Initial ϵ_{Hf} and ϵ_{Nd} will be compared with the initial ϵ_{Hf} and ϵ_{Nd} values from a Cretaceous peraluminous granite, the SWP (Fisher et al., 2017), in order to try to establish a source–melt relationship.

2.2 Regional Geology

The Mojave province is a component of the southern Laurentian Craton (Fig. 1a) and is thought to have formed in a marginal marine arc environment overlying enriched mantle in the Paleoproterozoic (Barth et al., 2000; Wooden et al., 2012). The Mojave Province contains recycled Archean and Paleoproterozoic crustal components ranging in age from 3.42 to 1.8 Ga (Bennett & DePaolo, 1987; Barth et al., 2000; Wooden et al., 2012) and the oldest exposed basement rocks have dominant detrital zircon dates of 1.9 to 1.8 Ga (Wooden et al., 2012). New material was added to the Mojave crust through widespread Paleoproterozoic (1.79–1.64 Ga) magmatism of potassic and intermediate to felsic plutons (Wooden et al., 2012). During the same time interval, the Mojave and Yavapai province formed new continental crust during the Ivanpah orogeny between 1.71 and 1.69 Ga (Barth et al., 2000; Duebendorfer, 2015). Following the Ivanpah orogeny was a period of alkaline plutonism between 1.69 and 1.64 Ga and then deposition of Pinto Mountain Group sediments between 1.63–1.45 Ga marking the stabilization of the Mojave crust (Barth et al., 2009). For the remainder of the Proterozoic, the Mojave crust underwent granitoid magmatism between 1.43 and 1.40 Ga (Anderson & Bender, 1989), anorthosite-mangerite-charnockite-granite (AMCG) suite emplacement between 1.21 and 1.18 Ga (McLelland et al., 2010), diabase dike intrusions around 1.09 Ga (Barth et al., 2001), and the onset of crustal extension which proceeded into the Cambrian (Wooden et al., 2012). During this time of extension, basement rocks were overlain by discrete siliciclastic-carbonate sequences, recording the transition from stable Mojave crust to the rifted Cordilleran margin (Barth et al., 2009). From the Cambrian until the Triassic period, major tectonic activity settled, and the Mojave was part of a passive margin resulting in deposition of a thick miogeocline sequence (Stewart, 1972). The Mojave crust was

remobilized to a compressional regime due to subduction of the Farallon plate beneath the North American plate beginning in the mid-Mesozoic (Burchfiel & Davis, 1972). This resulted in crustal thickening, low- to high-grade metamorphism, and widespread plutonism responsible for the formation of the Cretaceous Old Woman–Piute Mountain Range and the emplacement of metaluminous and peraluminous granites within the Old Woman Mountains (Fig. 1b) (Foster et al., 1992; Miller et al., 1992; Miller & Wooden, 1994). Near the end of the Cretaceous period into the Paleogene (80–60 Ma), the Farallon plate flattened beneath the North American Plate causing migratory magmatism and deformation (i.e., Laramide Orogeny) (Copeland et al., 2017). Shallowing of the angle of the Farallon Plate subduction also caused the Mojave province to undergo rapid uplift, unroofing, and cooling (Foster et al., 1992). The crust was reactivated by basin and range tectonism in the mid-Tertiary resulting in voluminous intrusions of felsic and mafic magmas, dike swarms, and major extension (Eaton, 1982). In the eastern Mojave, extension is thought to have spanned 23–15 Ma and thinned the crust from ~ 40 to ~20 km (Davis and Lister, 1988).

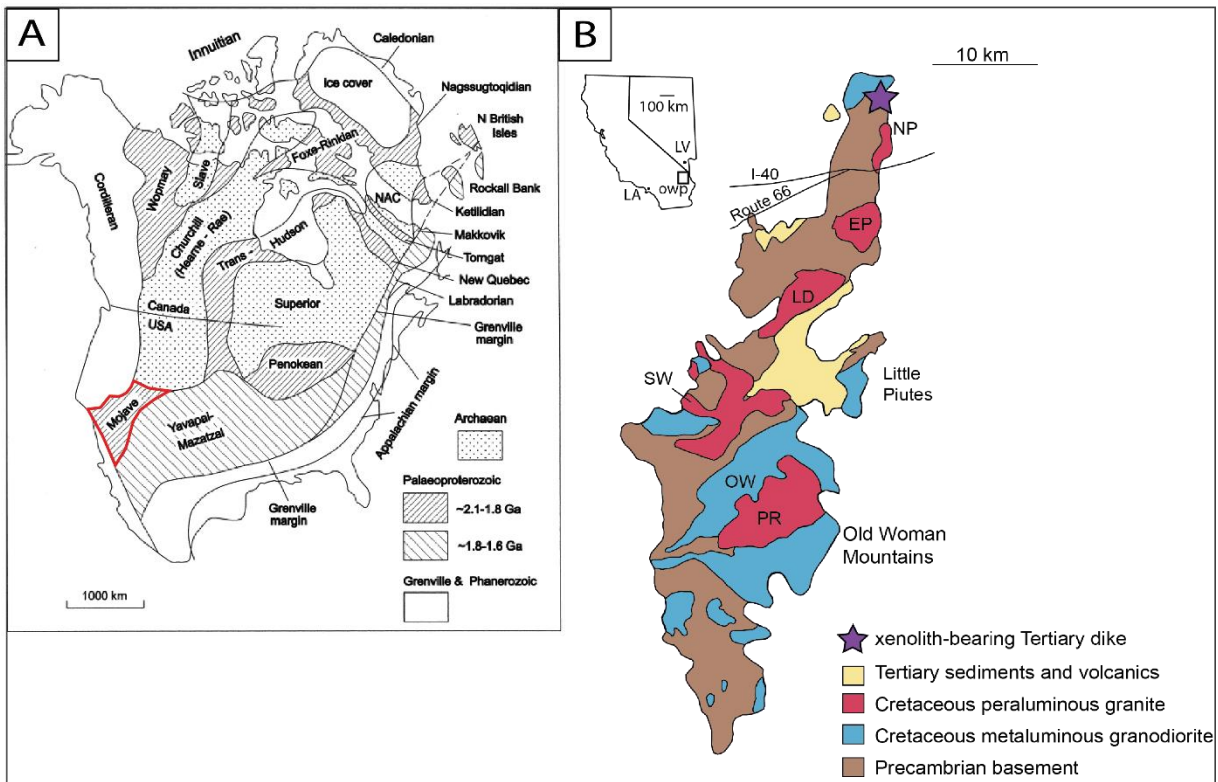


Figure 1. (a) Map of the North American geological provinces after Buchan et al., 2000. (b) Geologic map of the Old Woman–Piute Mountain Range modified from Fisher et al. (2017) Abbreviations: NP – North Piute pluton, EP – East Piute pluton, PR – Painted Rock granite, OW – Old Woman granodiorite, LD – Lazy Daisy pluton, SW – Sweetwater Wash pluton.

The xenolith bearing North Piute dike in the Old Woman–Piute Mountains is thought to be related to a mid-Tertiary dike swarm which extends into the southern end of the Piute Range (Old Woman Mountains), the Homer Mountains, the northern Sacramento Mountains, and parts of the Dead and Newberry Mountains. (Spencer, 1985). The dike has a rhyolitic to rhyodacitic core with basaltic to andesitic margins and cross cuts the Goffs Pluton (GP) (Cretaceous metaluminous granite) and the Proterozoic Fenner Gneiss (Precambrian basement) (Fig. 1b) (Hanchar et al., 1994). Unlike most dikes in the mid-Tertiary dike swarm, the North Piute dike contains lower crustal xenoliths that are the subject of this study

(Hanchar et al., 1994). The xenolith suite is comprised of quartz-rich, felsic, aluminous, and mafic garnet-amphibole granulites. Based on thermobarometry calculations, Hanchar and others (1994), proposed that these xenoliths last equilibrated at 750 +/- 50 °C and 1.0 +/- 0.2 GPa in the pre-extensional lower crust of the Mojave Desert. In addition, U–Pb geochronology multi-grain isotope dilution–thermal ionization mass spectrometry (ID–TIMS) on zircon from a quartz-rich sample suggests that the xenoliths originated within the Proterozoic crust of the eastern Mojave Desert and that they were affected by a major event in the Mesozoic (i.e., Laramide Orogeny) (Hanchar et al., 1994).

2.3 Methods

Representative aluminous xenolith samples were used for studying the metamorphic microstructures, mineral chemistry, and phase equilibria modeling to constrain the P–T history. In addition, U–Pb, Lu–Hf, and trace elements in zircon grains from samples XJ-100 (quartzose), XJ-9 (quartzofeldspathic), XC-9f, XJ-60, and XJ-150 (aluminous) and U–Pb, Sm–Nd, and trace elements in monazite grains from samples XJ-60 and XC-9f, were measured to obtain information about the timing of the initial crystallization and source(s) and timing of metamorphism.

2.3.1 Documentation of microstructures and mineral chemistry

Metamorphic microstructures of the aluminous samples were imaged using optical microscopy, high-resolution false colour thin section mapping using a scanning electron microscope equipped with a mineral liberation analysis software (SEM–MLA maps), and false-colour cathodoluminescence (CL) mapping of the internal structures of aluminosilicate minerals, kyanite and sillimanite with an electron probe micro analyzer (EPMA). Using

multiple imaging methods allows for detailed documentation of melt-producing and consuming metamorphic reaction microstructures and overall characterization of the xenolith samples.

Nine SEM–MLA thin section maps of aluminous xenoliths were acquired at the Micro Analysis Facility in the Bruneau Center at Memorial University of Newfoundland using either an FEI Quanta 400 tungsten or FEI 650 FEG SEM. The SEM produces high quality back-scattered electron (BSE) maps that illustrate differences in mean atomic number between minerals in greyscale. The MLA software identifies minerals and recognizes mineral grain boundaries, by collecting X-ray spectra from mineral grains in the thin section and matches it to an internal database to identify a mineral by its composition. The MLA software works simultaneously with the SEM to generate a false colour mineral map showing the overall distribution of phases, distinct mineral grain boundaries, and fine microstructural detail. Additionally, the SEM–MLA generates a table for each thin section analysed which consists of the phases identified by the instrument matched with the corresponding false colour on the map, the area and weight percent value, and number of pixels, particles, and area in microns for each phase listed.

Cathodoluminescence (CL) imaging was used to reveal the internal structures of aluminosilicate minerals and to enhance the microstructural relationships between quartzofeldspathic minerals adjacent to aluminosilicates at their vicinity. Cathodoluminescence maps of aluminosilicate minerals were acquired using the xCLent IV system coupled to a JEOL JXA-8230 Superprobe electron probe microanalyzer (EMPA) at Memorial University of Newfoundland. Mapping conditions include an acceleration voltage of 20 kV, a beam current of 200 nA, dwell time of 80 ms per step and pixel sizes between 7.5

and 2.5um depending on the size of the area mapped. During analysis, the system collects a CL spectrum from each pixel from the ultraviolet to the infrared spectral regions and generates a polychromatic false colour map of CL intensity (MacRae et al., 2013). The different colours on the map represent the range of relative CL intensity in which red is high intensity and blue is low.

In addition, mineral compositions of garnet, biotite, plagioclase, and K-feldspar from eight aluminous xenoliths were determined using the JEOL JXA-8230 Superprobe electron probe micro analyzer (EPMA) at Memorial University of Newfoundland. The EPMA has five tuneable wavelength dispersive spectrometers (WDS) that use analytical parameters such as acceleration voltage, beam diameter, current, and count time on peak and background. The values of these parameters are found in Appendix VI and were set specific to the mineral of interest. Mineral grains to be analyzed were selected based on microstructures, on the BSE and MLA maps produced by the SEM. To account for possible compositional zoning within minerals such as biotite, plagioclase, and garnet, individual grains were mostly analyzed in different locations (e.g., core and rim). In addition, garnet was generally analyzed along transects of 10 to 20 points depending on the grain size from rim-core-rim. Mineral grains were analyzed in different microstructural settings within the thin section to detect any compositional variations with respect to textures.

2.3.2 Phase equilibria modelling

Phase equilibria modelling was done to calculate mineral equilibria diagrams or P–T “pseudosections” and to model the compositions of melt produced at different points on the P–T space. Pseudosections are a type of phase diagram calculated for a specific bulk

composition that show stability fields that represent equilibrium relationships between phases. Calculations were made with THERMOCALC software (Powell & Holland, 1988) using an internally consistent thermodynamic database of pure phases and solid solution end members and their corresponding activity models (Holland and Powell, 2011). P–T pseudosections were used here to evaluate the peak P–T conditions for the aluminous xenoliths and to predict prograde and retrograde portions of the P–T path by exploring the effect of changing P–T on the mineral assemblage. THERMOCALC allows for the calculation of stability fields of mineral assemblages, bounded by univariant lines representing stability for one specific mineral (Powell & Holland, 1988). Univariant lines are calculated by defining the variance, or degrees of freedom, of the Gibbs phase rule; a mineral assemblage; a mineral to be set to 0 mode %; a P–T range; and a P–T interval within the THERMOCALC software (Powell & Holland, 1988). The output calculations from THERMOCALC (Holland and Powell, 2011) are saved as in a script file and imported into Drawpd to produce a visual presentation of the THERMOCALC results. THERMOCALC has an internal error in the order of ± 20 °C for temperature-dependent lines and ± 0.05 GPa for pressure sensitive lines. However, the real propagated errors cannot be more explicitly quantified because there is uncertainty as to what extent the bulk compositions are representative, errors in the EPMA analyses, and uncertainties in the activity models used in the calculations (Indares et al., 2008). In addition, the software was used to calculate lines of equal mineral proportions (isomodes) and equal mineral composition (i.e., isopleths) in specific P–T fields of interest.

Pseudosections for aluminous samples XJ-150, XJ-21, XS-41a, and NPX-17-03a were constructed using THERMOCALC version 3.33 in the NCKFMASHTO ($\text{Na}_2\text{O} + \text{CaO} + \text{K}_2\text{O} + \text{FeO} + \text{MgO} + \text{Al}_2\text{O}_3 + \text{SiO}_2 + \text{H}_2\text{O} + \text{TiO}_2 + \text{O}$) system (Holland & Powell, 2011), Drawpd

version dr112, and thermodynamic database tcds55 (Holland & Powell, 1998). The a-x mixing models used include: garnet, biotite, and silicate melt from White et al. (2007), cordierite from Holland and Powell (1998), orthopyroxene from White et al. (2002) muscovite from Coggon and Holland (2002), plagioclase and K-feldspar from Holland and Powell (2003), and ilmenite from White et al. (2000). Stable phases were labelled using the following abbreviation scheme from THERMOCALC (Powell & Holland, 1988): garnet (g); biotite (bi); plagioclase (pl); rutile (ru); kyanite (ky); sillimanite (sill); K-feldspar (ksp); muscovite (mu); cordierite (cd); silicate melt (liq); quartz (q). Remarks on the NCKFMASHTO system and database tcds55 are found in Appendix IX.

2.3.3 Zircon and monazite analyses

One hundred and twelve zircon and forty monazite were separated and mounted by John Hanchar. Zircon and monazite were analyzed from xenolith samples XJ-60, and XJ-9F and only zircon was analyzed from xenoliths XJ-9, XJ-100, and XJ-150. Prior to both isotope, major element, and trace element analyses, zircon and monazite were imaged using a JEOL JSM 7100F scanning electron microscope in the Earth Resources Research and Analytics Facility at Memorial University. Cathodoluminescence imaging was used to capture zircon and BSE was used for monazite images. The morphologies and sizes of zircon posed a challenge for LASS analyses. Multiple grains in each mount were not able to be analyzed resulting in a smaller dataset than desired and some dates reflect mixing between the inner, mid, and outer cores, and between the core and rim.

Zircon U–Pb and Hf, and monazite U–Pb and Nd were analyzed by laser ablation split stream (LASS). in the Micro-Analysis Facility of the Bruneau Centre for Research and

Innovation (MAF-IIC) at Memorial University of Newfoundland, using a Thermo-Finnigan NEPTUNE multi collector (MC) ICP–MS, ThermoFinnigan ELEMENT XR magnetic sector (HR) ICP-MS, and a GEOLAS 193 nm excimer laser system. The LASS method allows for high spatial resolution, simultaneous measurements of U–Pb, Lu–Hf, and Sm–Nd isotopes (Kylander-Clark et al., 2013; Goudie et al., 2014), in zircon and monazite, respectively, in the same ablation volume. The LASS method uses a laser ablation system coupled to a magnetic-sector inductively coupled plasma mass spectrometer (HR) (ICP–MS) for measuring U–Pb isotopes, and a multi-collector (MC) ICP-MS for measuring Lu–Hf and Sm–Nd isotopes. Zircon analyses were done using a spot size of 40 μm , a laser energy density of 5 J/cm^2 , and a pulse frequency of 10 Hz per 600 pulses. Monazite analyses were done using a 20 μm spot size, a laser energy density of 3 J/cm^2 , and a pulse frequency of 5 Hz per 300 pulses. The detector configuration identical to that of Fisher et al. (2011) and Goudie et al. (2014). Further details on this method are found in appendix XI. The U–Pb results from these analyses are plotted on Concordia diagrams and weighted mean plots using IsoplotR (Vermeesch, 2018).

The EMPA analyses were completed using a JEOL JXA-8230 Superprobe EPMA in the Earth Resources Research and Analytics Facility at Memorial University of Newfoundland. Electron microprobe analyses were done on zircon and monazite prior to LA-ICPMS analysis to measure major element compositions in order to use them as the internal standard for reducing LA–ICPMS trace element data using iolite software (Paton et al., 2011). Standards and detailed operating conditions for these analyses are found in Appendix VI. A complete list of results is found in appendix XIV for zircon and appendix XVII for monazite.

Trace elements were measured in zircon and monazite on a new spot separate from radiogenic element LASS analysis. This was done using laser ablation inductively coupled plasma mass spectrometry (LA-ICP-MS) with a ThermoFinnigan ELEMENT XR magnetic sector (HR) ICP-MS, and a GEOLAS 193 nm excimer laser system in the Micro-Analysis Facility of the Bruneau Centre for Research and Innovation (MAF-IIC) at Memorial University of Newfoundland. Operating conditions are the same as that of the LASS analyses for both zircon and monazite. The data was reduced in Iolite (Paton et al., 2011) using Hf (ppm) for zircon and Ca (ppm) for monazite as measured by the EPMA. A complete list of results is found in Appendix XV for zircon and Appendix XIX for monazite. Trace element concentrations were plotted using chondrite normalized REE plots.

2.4 Results

This section contains the results of this work and in addition, the microstructures and mineral chemistry sections include some brief interpretations that are prerequisite for the phase equilibria modelling results and discussion sections.

2.4.1 Metamorphic microstructures revealed by optical microscopy and SEM-MLA

The key microstructures in the aluminous xenoliths are described here, and complete sample descriptions are given in Appendix I. Modal mineral proportions for individual samples are presented in Figure 2. Representative false colour SEM-MLA maps of thin section are shown in Figure 3, and the full set of maps and modal data are available in Appendices II to IV. Photomicrographs of microstructures related to key metamorphic reactions and melting are shown in Figure 4. The aluminous xenoliths contain a mineral assemblage of quartz + K-feldspar + plagioclase + garnet + biotite + rutile + kyanite with rare

sillimanite and accessory zircon, apatite, and monazite. Minor chlorite, hercynite spinel, and magnetite are located proximal to host rock contact. The host rock is an intermediate composition andesitic dike composed of plagioclase, quartz and clinopyroxene with minor chloritization of clinopyroxene and epidotitization of clinopyroxene and plagioclase (Hanchar et al., 1994). The importance of the dike here goes as far as being the xenolith transport mechanism and is not related to them isotopically (Hanchar et al., 1994). Therefore, the dike is excluded from the description of microstructures and modal proportions. The xenoliths overall are texturally heterogeneous and are either massive, or weakly to strongly foliated. Mineral proportions cover a wide range, and to facilitate description, the samples were divided in two types: those rich in garnet and plagioclase (e.g., samples XJ-150 and XJ 210) and those dominated by a quartz–feldspar matrix (e.g., XJ-21, XS-41a, and NPX-17-03A).

2.4.1.1 Mineral microstructures in two xenolith types

2.4.1.1.1 Garnet–plagioclase-rich aluminous xenoliths

These xenoliths are texturally massive and dominated by garnet–plagioclase domains enclosing distinct quartz pods (Fig. 3a,b). K-feldspar is in minor amounts and is associated with secondary carbonate and quartz in rounded blebs at the rims of some larger plagioclase grains (Fig. 4a) Additionally, biotite in both samples is located proximal to rims of garnet and rutile. In XJ-150 garnet forms abundant porphyroblasts in a plagioclase matrix. Kyanite grains are partially resorbed and form rare clusters in the matrix. In XJ-210, garnet forms pervasive clusters of relatively small grains. Corroded kyanite blades rimmed by K-feldspar and hercynite spinel are localized in a 5mm band separating garnet clusters into two halves on the thin section.

2.4.1.1.2 Quartz–feldspar-rich aluminous xenoliths

These samples have a matrix dominated by quartz and plagioclase feldspar with garnet porphyroblasts. The matrix of XJ-21 is composed of quartz, K-feldspar and plagioclase (Fig. 3c). This sample also contains resorbed biotite, elongated kyanite-rich domains, and rare small sillimanite (Fig. 4b and c, respectively). Sample XS-41a displays a quartz–K-feldspar dominated matrix with large kyanite grains (>3mm) and a weak foliation defined by biotite (Fig. 3d). Garnet porphyroblasts and kyanite appear in thin section to be localized near the host rock contact. Kyanite is partially resorbed and surrounded by thick films of K-feldspar. Sillimanite is present exclusively as rare prismatic grains included within garnet (Fig. 4d). Finally, sample NPX-17-03A has a quartz–K-feldspar matrix with elongated clusters of small garnet porphyroblasts and a strong foliation defined by kyanite (Fig. 3e). Kyanite blades are amalgamated to form bands that elongate perpendicular to individual grain orientation and contain tiny inclusions of K-feldspar and quartz (Fig. 4e).

2.4.1.2 Quartz and feldspar

Quartz, K-feldspar, and plagioclase are present in all samples as either aggregates in the matrix or as smaller anhedral grains interstitial to other crystals. In samples with a quartz–K-feldspar dominated matrix (e.g., XJ-41a and NPX-17-03A), patches of quartz and plagioclase exhibit symplectic texture within much larger matrix K-feldspar grains (Fig. 4f). Interstitial quartz–feldspar microstructures typically have “blebby” habits that form in pockets surrounding or interstitial to minerals such as euhedral aluminosilicate and other quartz and feldspar grains (Fig. 4a, c).

2.4.1.3 Garnet

Garnet is equant, subhedral to anhedral ranging in size from ~0.1 to ~3mm in diameter. It contains inclusions of quartz, biotite, kyanite, and rare sillimanite in addition to accessory minerals zircon, apatite, monazite, and magnetite. Garnet proximal to the host rock contact has a thick, polymineralic rim composed of chlorite, magnetite, biotite, and locally, hercynite spinel. These rims are thinner or nonexistent on garnet towards the center of the xenolith relatively distant from host rock.

2.4.1.4 Aluminosilicates

Kyanite is present as variably resorbed anhedral blades. Resorbed kyanite typically rimmed by films of K-feldspar (Fig. 4g). Larger blades contain inclusions of quartz, K-feldspar, plagioclase, garnet, rutile, zircon, and monazite. Rare sillimanite is present as 0.1 to 0.5 mm long, euhedral to subhedral acicular prisms located either in the matrix in XJ-21 or as inclusions in garnet. Matrix sillimanite is in close proximity to larger dominant kyanite blades (Fig. 4b) or clustered within anhedral K-feldspar that is interstitial to quartz (Fig. 4c).

2.4.1.5 Biotite

Biotite exists in a variety of microstructural settings. Most commonly biotite is present as anhedral to subhedral laths rimming garnet and interstitial to matrix phases (Fig. 3a, c). Subhedral to euhedral tabular biotite is observed in sample XS-41a as a part of the inequigranular quartz–feldspar matrix (Fig. 3d). Biotite included within garnet in XJ-21 is small and rounded relative to biotite outside garnet. Thick biotite coronas around garnet are located proximal to the dike contact and are amalgamated with chlorite and magnetite (Fig. 4h).

2.4.1.6 Rutile

Rutile is typically anhedral and range from 0.2 to 1 mm in length. They exist within the matrix and are commonly associated with garnet, biotite, and kyanite, but not associated with sillimanite. Fine reaction rims of ilmenite form a corona around rutile.

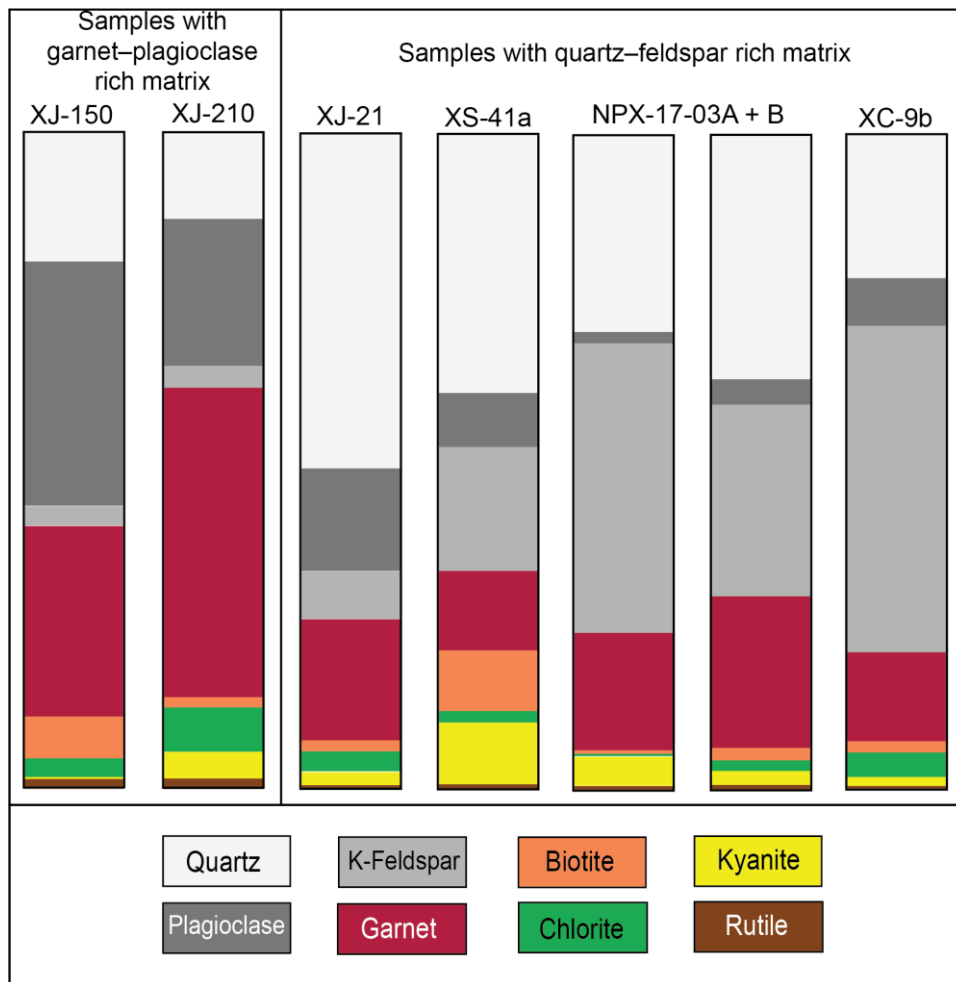


Figure 2. Modal percent of minerals given by SEM-MLA analysis greater than 1% in the rock represented on normalized bar diagrams.

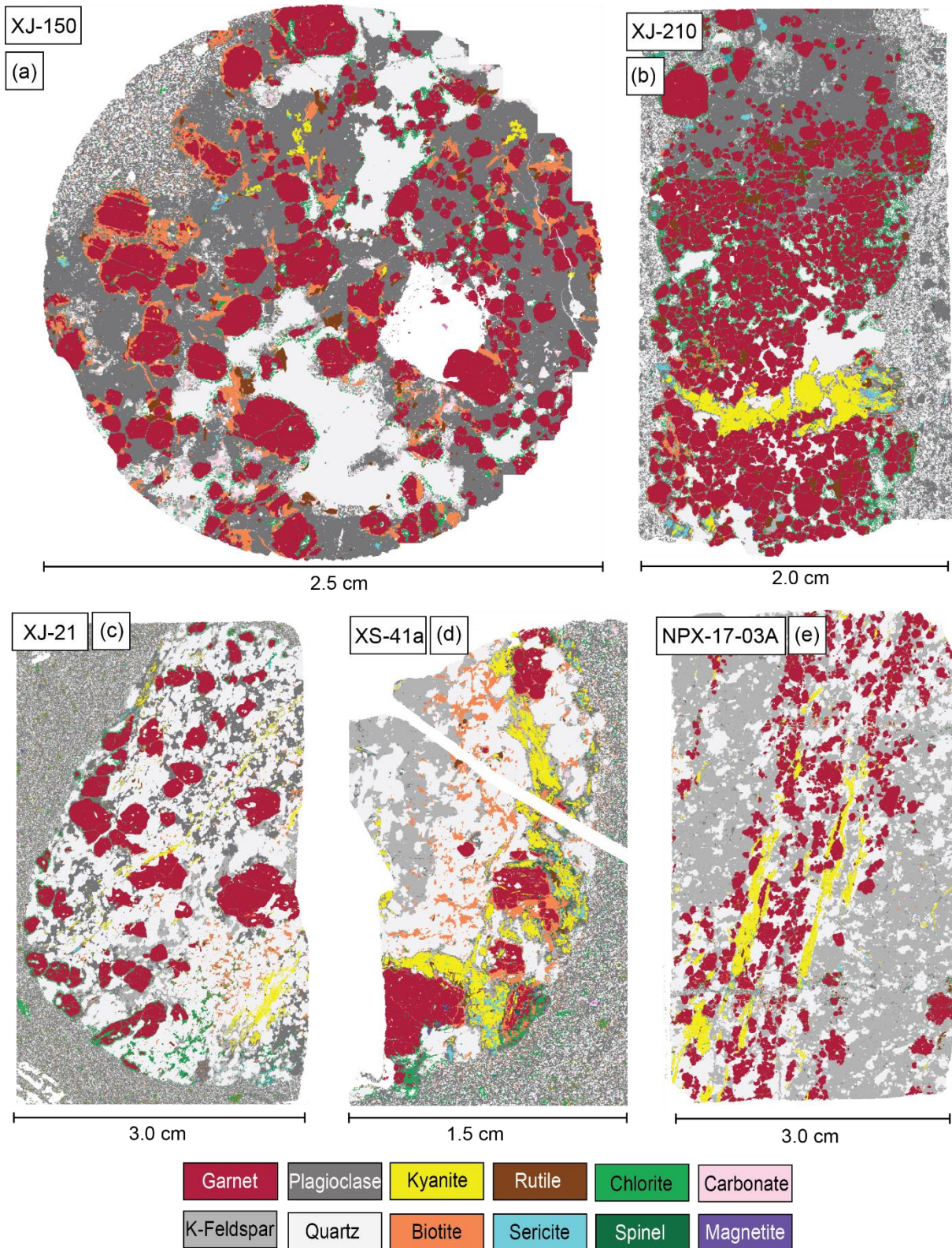


Figure 3. False coloured SEM-MLA thin section maps for samples XJ-150, XJ-210, XJ-21, XS-41a, and NPX-17-03A.

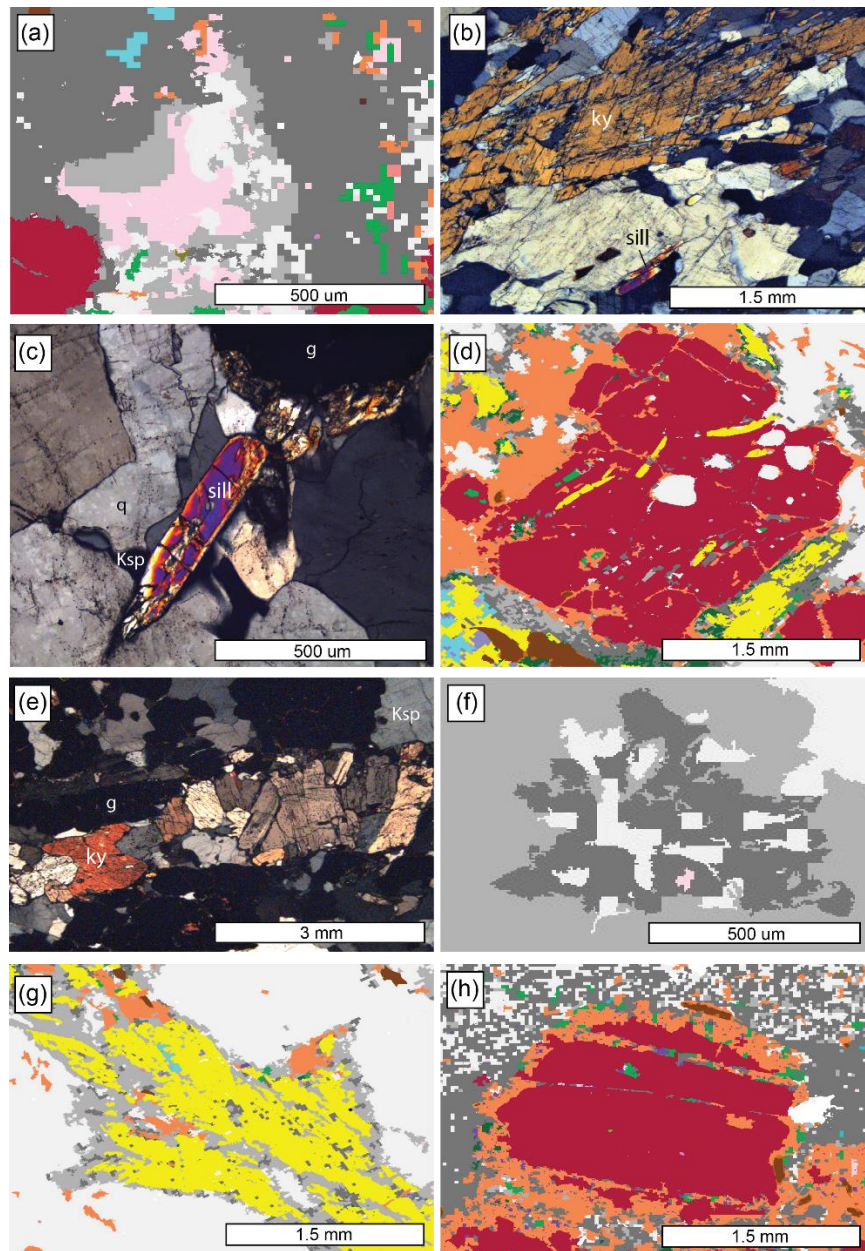


Figure 4. Petrographic and SEM–MLA images highlighting significant microstructures. Legend for false colours on SEM–MLA images are found in figure 3. (a): rounded quartz domain containing blebby interstitial K-feldspar and late carbonate within matrix plagioclase from XJ-150. (b): Large resorbed kyanite blades adjacent to smaller prismatic sillimanite in a quartzofeldspathic matrix from XJ-21. (c): Prismatic sillimanite surrounded by K-feldspar interstitial to quartz from XJ-21. (d): Small prismatic sillimanite inclusions within garnet in XJ-41a. (e): Bands of amalgamated kyanite oriented perpendicular to individual grain orientation from NPX-17-03A. (f): intergrowth of quartz and plagioclase within K-feldspar matrix from NPX-17-03A. (g): heavily resorbed kyanite crystal surrounded by a rim of K-feldspar XS-41a. (h): garnet proximal to dike contact with thick coronas of biotite, magnetite, and chlorite from XJ-150.

2.4.2 Metamorphic microstructures revealed by xCLent CL maps of aluminosilicates

Kyanite from samples XJ-21, XS-41a, and NPX-17-03a, and sillimanite from XJ-21 were mapped using the xCLent system to produce false colour CL maps.

Cathodoluminescence maps with key microstructures are presented in Figures 5a to d.

2.4.2.1 Kyanite

Kyanite grains display two main CL internal structures: 1) mottled CL colours of similar intensity; and 2) high-CL resorbed cores truncated by a thin low-CL rims. Kyanite which exclusively exhibit pattern 1 are typically larger, 4 to 6 mm sized aggregates or clusters with extreme to minor resorption of the rims. Pattern 1 kyanite have mottled colour patterns of similar CL intensities lacking distinct core and rim boundaries (Fig. 5a,b). In these images, CL intensities between adjacent grains appear to vary drastically. The varying CL intensities are likely due to differences in trace Cr^{3+} and Fe^{2+} contents in the respective growth zones within grains (Kendrick and Indares, 2017; Wojtowicz 1991). Pattern 2 is present within a smaller, isolated kyanite grain (0.5 mm) exclusively in NPX-17-03A. This pattern consists of a high-CL intensity (orange, yellow-orange) core with minor patches of relatively higher CL (red) overgrowths on the edge of the core (Fig. 5c). Truncating the entire high-CL core is a thin, low intensity CL (blue) overgrowth with slight concentric zonation. The shape of the low-CL overgrowth matches that of surrounding K-feldspar film interstitial to quartz matrix.

2.4.2.2 Sillimanite

A cluster of sillimanite about 0.5 mm in length in sample XJ-21 are surrounded by anhedral K-feldspar interstitial to surrounding granular quartz. The elongated grain has a low

CL emission with peaks of relatively higher CL sillimanite in concentric, growth zones (Fig. 5d).

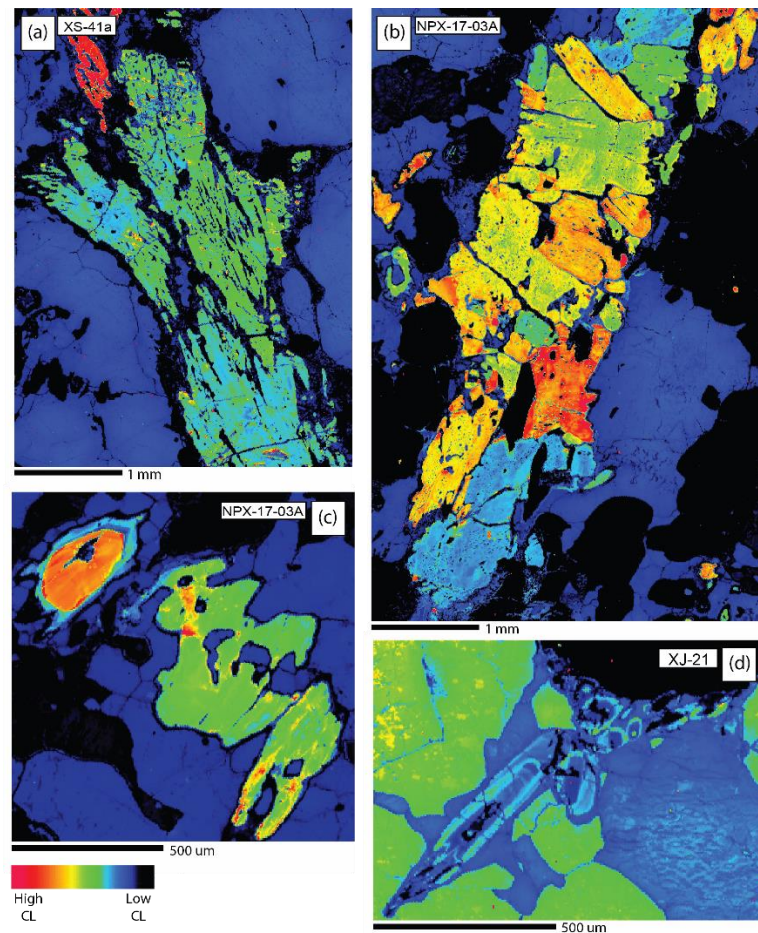


Figure 5. Cathodoluminescence (CL) maps of aluminosilicate phases. (a): Resorbed kyanite separated from quartz (blue) by a very low CL rim of K-feldspar. Internal structure of kyanite lacks distinct core and rim boundaries and CL intensities are mottled/smeared. (b): Grains of kyanite amalgamated into an elongated band associated with garnet and rutile (black), and quartz (blue). Individual grains have a mottled/smeared CL pattern. (c): Zoned kyanite crystal (upper left) adjacent to a kyanite where zoning is less defined. The zoned crystal preserves a high-CL resorbed core (orange) with a low-CL rim overgrowth (light blue) surrounded by K-feldspar (black) interstitial to quartz (dark blue). (d): Prismatic sillimanite (shades of blue) surrounded by K-feldspar (blue) interstitial to quartz (green). Sillimanite preserves concentric growth zoning revealed in CL by different shaded ellipses of blue and green.

2.4.3. Insights on anatexis based on microstructures

The dominant mineral assemblage of quartz + garnet + kyanite + rutile + quartz + K-feldspar + plagioclase in the aluminous xenoliths reflects high-*P* granulite facies metamorphism and anatexis. Pools, pockets, films, and blebs of quartz and feldspar interstitial to larger crystals are interpreted as protoleucosomes which pseudomorphed former melt domains upon cooling (Fig. 4 a,c), and the larger crystals are interpreted to be residual or peritectic (Vernon 2011). Additionally, symplectic intergrowth patches of quartz and plagioclase are consistent with crystallization of former melt (Fig, 4f). Apart from former melt pseudomorphs and microstructures linked directly to the presence of melt, partial melting may be inferred from internal structures of aluminosilicates revealed by CL and microstructural relationships between the rock forming minerals. Such features are linked here with common fluid-absent melt-producing and melt-consuming metamorphic reactions for anatectic aluminous rocks. These reactions include the muscovite dehydration reaction:



the biotite dehydration reaction:



and the reverse of the biotite dehydration reaction (Spear et al., 1999; Vielzeuf and Holloway, 1988).

2.4.3.1 Microstructures consistent with melting of micas

The evidence for muscovite dehydration in these xenoliths is elusive. However, the presence of large kyanite blades and kyanite replacing a cluster of an earlier aluminous phase,

in XS-41a and NPX-17-03A is consistent with the occurrence of the muscovite melting reaction (eq. 3)

Biotite dehydration melting is consistent with resorption and corrosion of pre-existing kyanite grains. Evidence for this is observed in every sample that was investigated. The rocks contain small amounts of biotite (from 1 to < 10 mode %), which is texturally late. Therefore, it is inferred that prograde biotite was largely to completely consumed by partial melting. This is comparable with that of other melt-depleted aluminous granulites in the literature (Otamendi & Patiño Douce, 2001; White & Powell, 2002).

2.4.3.2 Microstructures consistent with melt-crystallization

The crystallization, during cooling, of melt present in the rock is inferred to have occurred by the reverse of the biotite dehydration reaction. The most obvious evidence for this is the presence of biotite overgrowing garnet rims and anhedral biotite interstitial to the quartz–feldspar matrix, consistent with late biotite growth during retrograde metamorphism. In addition, microstructural evidence for a second generation of kyanite growth is revealed in the CL maps. A high-CL kyanite core in sample NPX-17-03A likely formed via muscovite dehydration reaction, then resorbed by the biotite dehydration reaction, is overgrown by a low-CL kyanite rim surrounded by a melt pseudomorph (Fig. 6). Prismatic sillimanite within a protoleucosome in sample XJ-21 with concentric high-CL growth zonation also infers crystallization from a melt. The presence of kyanite and sillimanite in these microstructural settings along with pseudomorphed, melt replacement microstructures, is interpreted to represent late-stage growth from the reverse biotite dehydration melt crystallizing reaction. Evidence for late stage kyanite and sillimanite contradicts Hancher et al. (1994) which states

that all sillimanite in the xenoliths formed before the earliest kyanite generation. Although there is strong evidence for early sillimanite growth preserved as prismatic inclusions within garnet, the CL maps reveal a second late-stage sillimanite growth in the matrix. If kyanite overgrowths and new sillimanite are expected to have grown from the same metamorphic reaction, this has implications on the P–T conditions of melt crystallization depending on where in P–T space melting has occurred relative to sillimanite-kyanite-sillimanite growth.

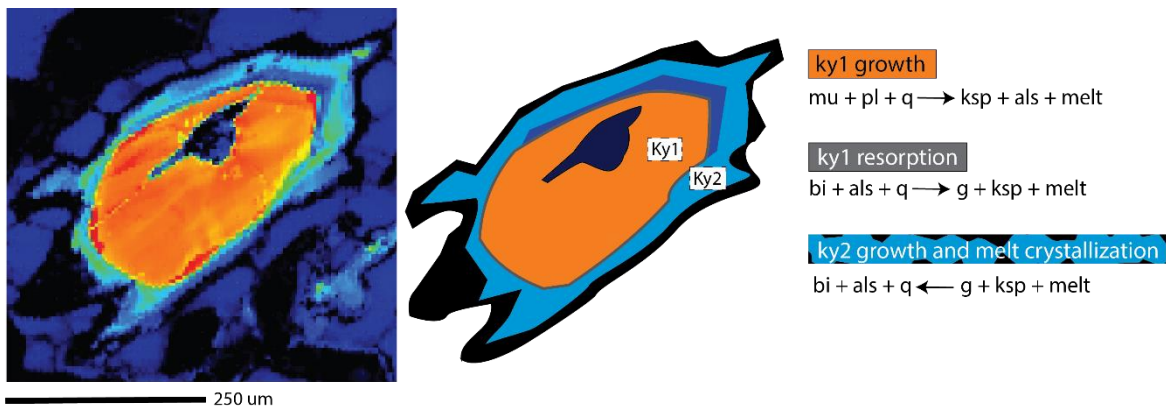


Figure 6. Illustration of kyanite CL map from sample NPX-17-03A demonstrating the growth history by means of three metamorphic reactions.

2.4.3.3 Evidence for melt loss

Well-preserved peak granulite facies assemblages in the xenoliths and limited retrograde assemblages (e.g., no late muscovite and only minor biotite), are consistent with significant melt loss, as expected for rocks experiencing partial melting in a dynamic environment (Brown, 2002; White & Powell, 2002). In addition, modal mineral proportions (Fig. 2) suggest that of a typical melt residue (Otamendi & Patiño Douce, 2001), especially in extreme cases such as the highly refractory sample XJ-210 that consists primarily of garnet,

rutile, and kyanite, with minor plagioclase and K-feldspar. Polyminerally reaction rims around garnet is attributed to external fluids from the host rock rather than retrograde metamorphism.

2.4.4 Mineral chemistry

Quantitative mineral chemistry data were acquired using EPMA for garnet, biotite, and feldspars in samples XJ-150, XJ-21, XS-41a, NPX-17-03A, NPX-17-03B, XC-9a, XC-9b, and XJ-210. Electron probe standards are listed in Appendix VI and the analytical data are in Appendix VII.

2.4.4.1 Garnet

Average garnet end member compositions are plotted on a ternary diagram (Fig. 7). Between 3 to 10 of the largest garnets were analyzed per sample in different textural settings. A preference is put on analyzing the largest grains in sample because of their greater potential for preserving growth zonation (Caddick et al., 2010). Garnet compositions were measured along transects to determine the change in end-member proportions from core to rim. In samples NPX-17-03A and XJ-210, smaller grains were analyzed in their core only because compositional zoning was not expected. In the xenolith samples analyzed, garnet is rich in almandine (52–65%), with moderate amounts of pyrope (25–42%) and low grossular and spessartine contents (4.9–13%, and 0.5–1.4%, respectively). Overall, the chemical composition of garnet is homogeneous at the grain scale, with some local variations that are linked with microstructural features. Garnet zoning profiles are shown in Figure 8 with emphasis Xgrs profiles because they show the most marked patterns relative to the other end members. In XJ-21 garnet 1 is adjacent to the quartz–feldspar matrix and shows some

embayment along the rims (Fig. 8a). This garnet is homogeneous in terms of X_{prp} and X_{alm} but shows an overall minor decrease in grossular and spessartine components towards the rims. Garnet 3 in XJ-21 was analysed along a transect from a rim adjacent to biotite to a rim adjacent to plagioclase (Fig. 8b). X_{alm} increases and X_{prp} decreases at both rims, with these changes most marked at the rim adjacent to biotite (rim 1). X_{grs} and X_{sps} also increase but only at rim 1. Garnet 2 from sample XJ-150 (Fig. 8c) is adjacent to the dike contact and surrounded by a thick rim of replacement biotite, chlorite, and Fe-Ti oxides. This garnet displays a sinusoidal X_{grs} profile as it is bell shaped in the interior and peaks towards the rims.

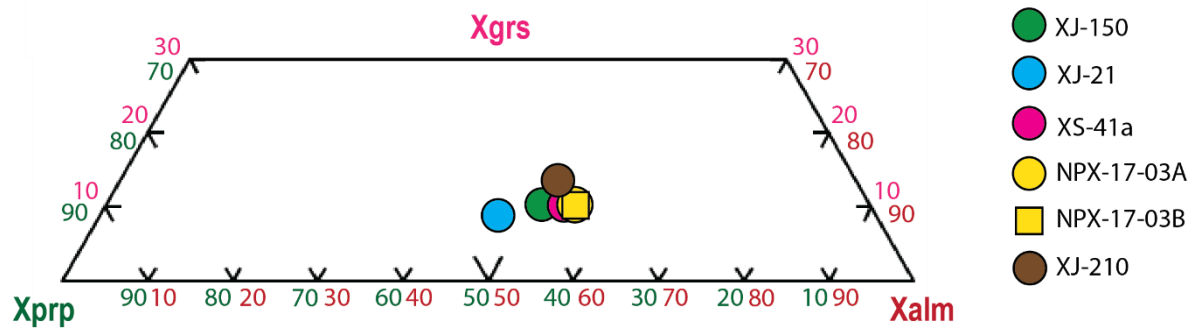


Figure 7. Average composition of garnet in end member percentages for each sample plotted on a ternary diagram. X_{prp} = molar proportion of pyrope, the Mg end member of garnet; X_{alm} = molar proportion of almandine, the Fe-end member of garnet; and X_{grs} = molar proportion of grossular, the Ca-end member of garnet.

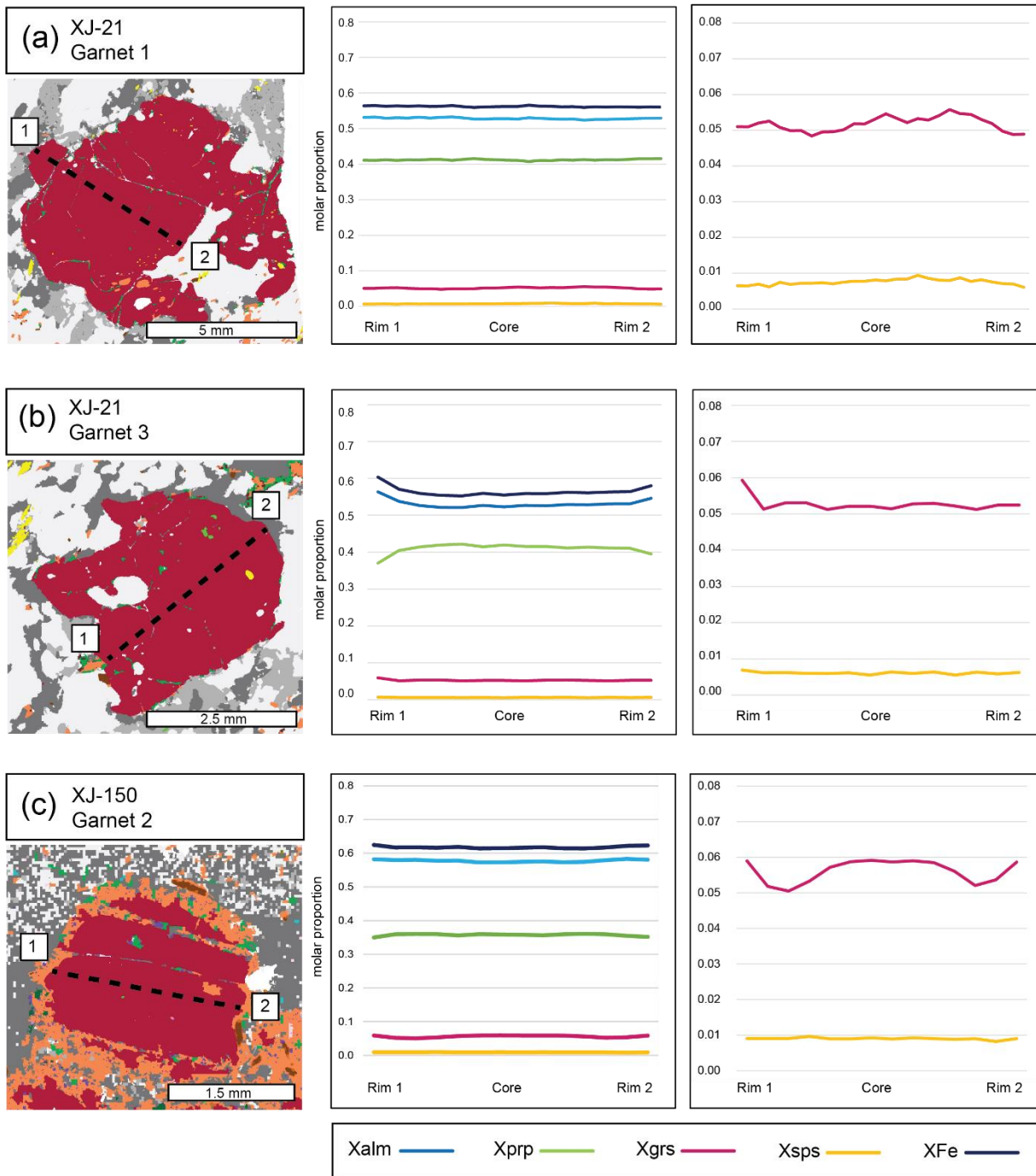


Figure 8. Examples garnet end-member zoning profiles with their corresponding SEM-MLA images obtained from SEM.

2.4.4.2 Biotite

In each thin section, between 8 and 12 grains were analyzed by EPMA in 3 textural settings: (1) isolated in the matrix; (2) adjacent to garnet; and (3) included in garnet. Ti contents range between 0.15 and 0.28 and Al^{IV} between 0.20 and 0.43 cations per formula unit. X_{Mg} mostly clusters between 0.52 and 0.76 except for XJ-21 which has higher X_{Mg} values ranging between 0.64 and 0.80. Individual grains are chemically homogeneous, but there are some differences between grains. Generally, biotite adjacent to or rimming garnet has lower Ti contents and, in some cases, higher X_{Mg} than biotite in the matrix (Fig. 9). Biotite included in garnet has the highest X_{Mg} from 73 to 80%. There is no clear relationship between Al^{IV} and the textural setting of biotite.

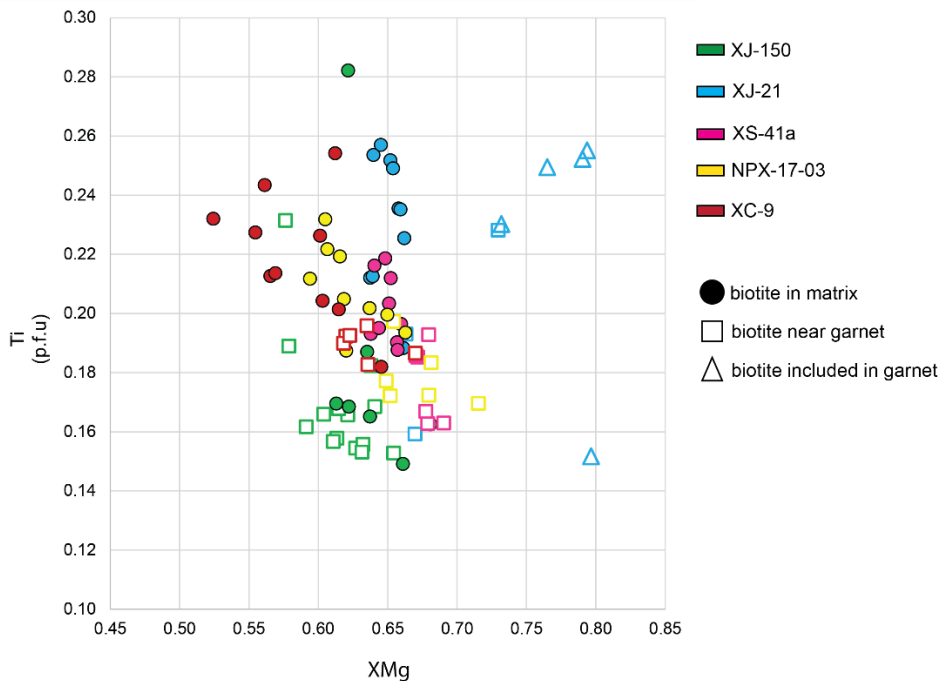


Figure 9. Scatter plot comparing biotite compositions in matrix, near garnet, and included within garnet in terms of X_{Mg} vs. Ti (per 11 oxygens).

2.4.4.3 Feldspars

Average compositions of feldspars for each sample are plotted on a ternary diagram (Fig. 10). Between 7 and 17 plagioclase and 10 and 14 K-feldspar grains were analyzed per sample, in two broad microstructural settings; As aggregates in the matrix and as interstitial blebs. Generally, plagioclase contains high proportion of Ab ranging from 62 to 83%. In addition, almost pure albite was identified in grains intergrown with quartz, adjacent to large K-feldspar in sample NPX-17-03A.

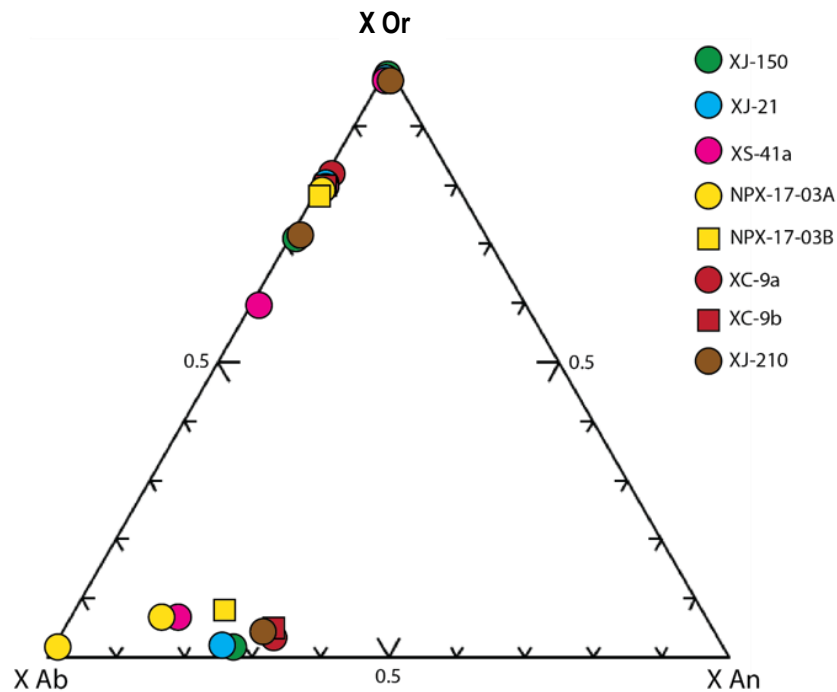


Figure 10. Average feldspar compositions plotted on a An–Or–Ab ternary diagram. K-feldspar compositions were grouped based on their textural setting which is directly related to having either relatively high (97–99%), moderate (70–86%), or low (53–70%) orthoclase Or content. Plagioclase compositions display less variation and therefore were averaged per sample with exception of nearly pure albite compositions which were averaged separately.

Proportions of Or in K-feldspar range from 53 to 99%. Highest Or contents (97–99%) were measured in K-feldspar in rounded, secondary carbonate + K-feldspar blebs associated with large plagioclase grains, and less so in garnet inclusions and K-feldspar rims around kyanite and plagioclase. Lesser proportions of Or (70–86%) were measured in matrix grains and in those rimming plagioclase and kyanite. K-feldspar with relatively low Or (53–70%) is exclusively found rimming kyanite and plagioclase.

2.4.4.4 Mineral chemistry patterns

The zoning profiles for garnet are linked here with specific microstructural features and growth conditions. Homogeneous garnet profiles particularly in the garnet interior may reflect either prograde growth at constant composition, or homogenization under high T near peak conditions facies metamorphism in the lower crust (Spear, 2014). Local rim zoning depends on the microstructural setting of garnet. Typically, zoning in X_{alm} and X_{prp} in garnet adjacent to biotite is attributed to a Fe–Mg exchange reaction between the two phases during cooling (Spear, 2014). In garnet proximal to the contact with the dike surrounded by chlorite, biotite, and magnetite coronas, the rims are also characterized by X_{grs} peaks, consistent with resorption to the benefit of biotite (Spear, 2014). Resorption of this garnet and biotite growth in this textural setting is likely due to the action of external fluids. However, biotite formation after garnet during melt crystallization cannot be excluded.

Variations in feldspar compositions in different textural settings is consistent with different episodes of feldspar formation. Nearly pure albite intergrowths can be linked to melt crystallization, whereas plagioclase with moderate albite content is either residual or peritectic. K-feldspar are interpreted to have formed under different conditions based on their

textures, spatial distribution, and chemical composition. It appears most likely that pure Or K-feldspar is restricted to melt-related microstructures and likely represents former melt. These microstructures include domains of quartz with late, euhedral secondary carbonate in samples XJ-150 and XJ-210 and rims of K-feldspar surrounding kyanite in XS-41a. Moderate Or K-feldspar is primarily a matrix phase and is interpreted to be residual or peritectic. K-feldspar rimming kyanite and plagioclase have low orthoclase grains along with pure and moderate orthoclase grains amalgamated into a single rim representing pseudomorphed melt.

2.4.5 Phase equilibria modelling

P–T pseudosections were calculated here for garnet–plagioclase rich sample XJ-150 and quartz–feldspar rich samples XJ-21, XS-41a, and NPX-17-03 to show the distribution of stable mineral assemblages in *P–T* space and use this as a framework to interpret microstructures and mineral chemistry data in terms of *P–T* paths. Pseudosections are presented in imperial units for pressure (kbar) however, the results in text will be presented in SI units (Gpa). Two sets were calculated for each sample: the first one using the xenolith bulk rock compositions; and the second using melt-reintegrated bulk rock compositions, to account for melt loss.

Xenolith bulk rock compositions were determined by combining modal proportions of minerals (estimated with SEM–MLA) and mineral chemistry data. Melt-reintegrated compositions were calculated using THERMOCALC by adding a melt portion sufficient to stabilize a water-saturated solidus (wet solidus). Details of the calculations and on the melt reintegration procedure are found in Appendix VIII.

2.4.5.1 *P–T pseudosections calculated with the bulk rock compositions of the xenoliths*

Pseudosections for these compositions were calculated at the $P–T$ range of 0.8–1.9 GPa and 640–920°C in order to simulate lower crustal conditions (Figs. 11a-d). These four pseudosections are characterized by:

- (1) a muscovite stability field restricted to high P of 1.55-1.8 GPa with a solidus coinciding with the muscovite-out line at high T except for pseudosections XJ-150 and NPX-17-03 where the solidus passes through the muscovite-in field and;
- (2) subvertical solidus and biotite-out lines at lower P and between 800 to 870°C except for pseudosection XJ-150 where disappearance of aluminosilicate at pressure below 0.8-1.3 GPa leads to increase of biotite stability to temperatures above 870°C (Fig. 11a).

The slope of the solidus line is comparable in each pseudosection, but there are variations in the position in terms of T . For instance, at 1.3 GPa sample XJ-21 has the highest solidus temperatures of 860°C and XJ-150 has the lowest at 800°C. Aluminosilicate phases and K-feldspar are stable in all fields except for XJ-150 in which aluminosilicate is eliminated at relatively lower P and K-feldspar is restricted to high P and T . This is consistent with the low proportions of these two phases in XJ-150. Plagioclase becomes unstable at high $P–T$ in XS- 41a and at lower P in NPX-17-03, consistently with the low amounts of plagioclase in these samples. In samples XJ-150 and XJ-21 plagioclase is stable in all fields.

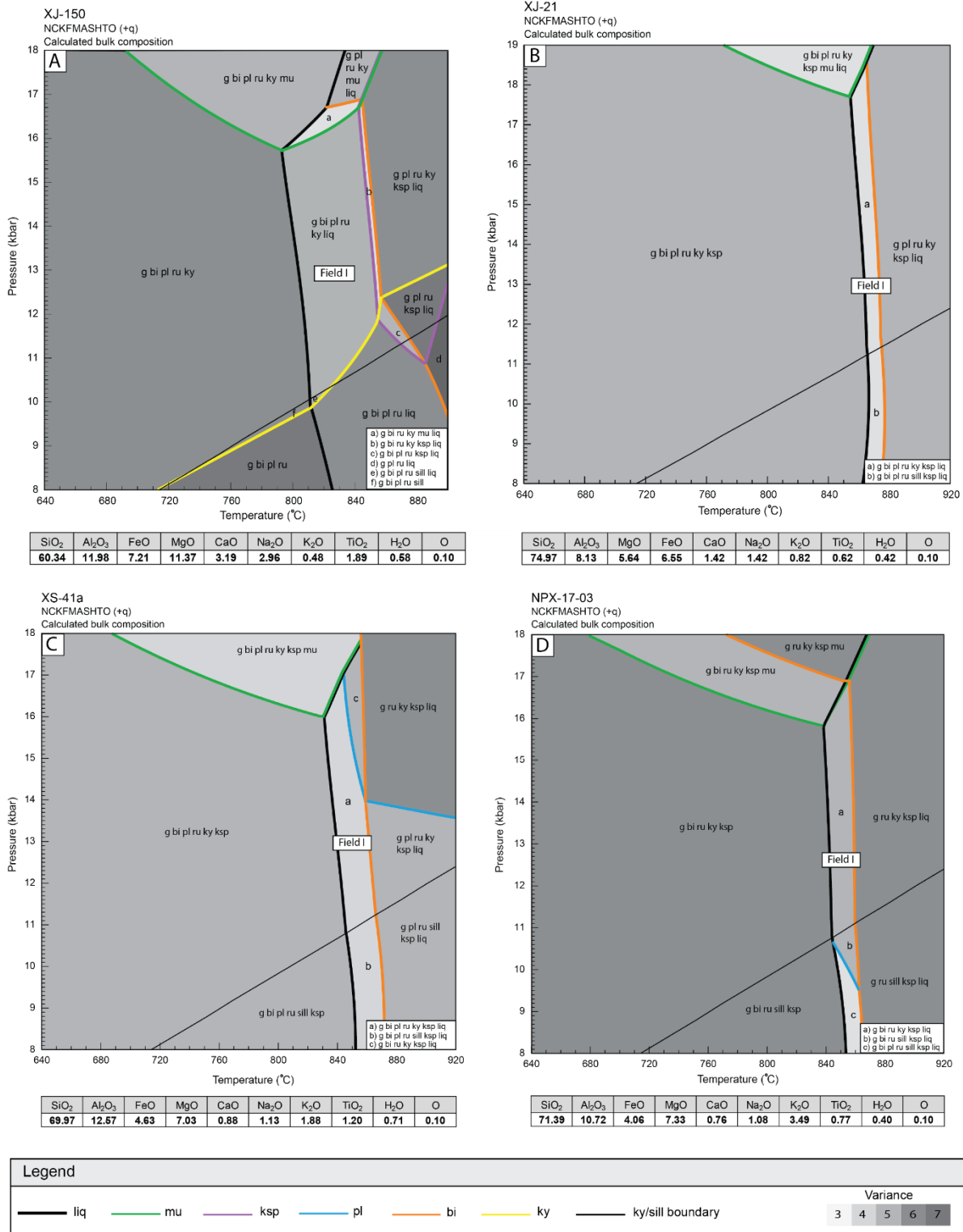


Figure 11. *P-T* pseudosections calculated using the bulk composition of each sample.

The field representing the observed assemblage of bi + g + als + ru + q + liq ± Ksp ± pl (Field I) is bound at high P of 1.55-1.8 GPa by the muscovite-out reaction line, at higher T by the biotite-out line, and at relatively lower T by the solidus line. Overall, this field is defined by the coexistence of biotite and liquid. It is a relatively narrow field on the P–T pseudosection diagram, consistently with the low modal % of biotite in the rocks, and therefore is extremely sensitive to changes in T. Sample XJ-150 has the highest proportion of biotite related to metamorphism and therefore has the widest field for this assemblage. The muscovite-stable field restricted to high-P is consistent with the lack of muscovite in the xenolith samples. Such restricted muscovite stability in an aluminous metasedimentary rock likely infers a loss of hydrous melt to the surroundings (White & Powell, 2002). Therefore, the solidus in this set of pseudosections, will be referred to as the ‘dry’ solidus.

2.4.5.2 *Isomodes and isopleths for the bulk rock compositions of the xenoliths*

For each pseudosection, isomodes for garnet, biotite, aluminosilicate, plagioclase, K-feldspar, and liquid and isopleths for grossular molar proportions and X_{Fe} (where $X_{\text{Fe}} = \text{Fe}/(\text{Fe} + \text{Mg})$) in garnet, and anorthite molar proportions in plagioclase, were calculated in the stability field of the observed mineral assemblage:



labelled as Field I in Figures 12a to d.

K-feldspar isomodes in pseudosection XJ-150 along with plagioclase isomodes (and anorthite isopleths) in NPX-17-03 are omitted. This is because these phases are not considered as part of the peak assemblage in these samples. Additionally, plagioclase isomodes are

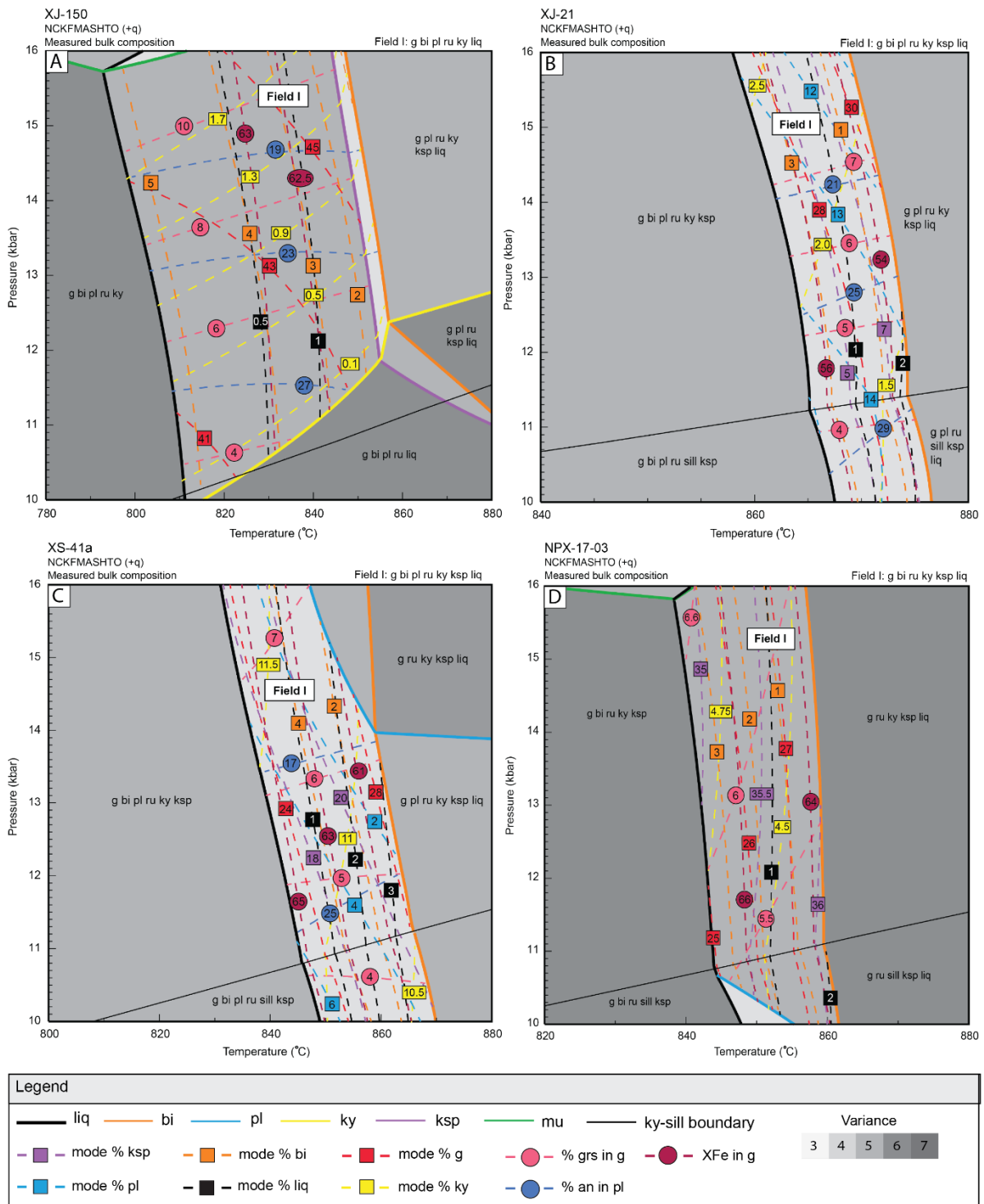


Figure 12. Isomodes and isopleths overlain on the P - T pseudosections of Figure 11.

omitted from XJ-150 because the mode % does not change within Field I in Figure 12a. Most isomodes have steep to vertical dP/dT gradients. Their distribution shows that with increasing temperature towards the biotite-out line, the proportions of garnet, K-feldspar, and liquid increase whereas those of biotite, aluminosilicate, and plagioclase generally decrease. In the pseudosection of the kyanite poorest sample XJ-150, however, kyanite isomodes have a moderate positive dP/dT gradient. Grossular and anorthite isopleths have shallow dP/dT gradients. In contrast, grossular isopleths in pseudosection NPX-17-03 have a steep gradient where anorthite is unstable. Grossular and anorthite isopleths are inversely correlated in which grossular molar proportions increase and anorthite molar proportions decrease with increasing pressure. Isopleths for X_{Fe} have a steep dP/dT gradient with values decreasing with increasing T towards the biotite-out line.

2.4.5.3 Melt-reintegrated P–T pseudosections

For these pseudosections, 25% of lost melt was added in the original bulk rock composition in order to stabilize a wet solidus (see Appendix VIII for method and melt compositions), except for sample NPX-17-03, for which 30% of melt was required without reaching a wet solidus at the P–T field of interest. Topologies for melt-reintegrated compositions show the mineral assemblages that were likely once present during prograde metamorphism prior to melt loss. Pseudosections were calculated for the same T range as the previous set of pseudosections but a lower P range of 0.6-1.6 GPa to account for potentially lower pressures during prograde metamorphism (Figs. 13a-d). Mineral stability fields in melt-reintegrated pseudosections at T above the dry solidus are similar to those calculated in the previous set of pseudosections. An exception to this is in NPX-17-03 in which the stability

field of plagioclase is present only in the melt-reintegrated pseudosection. The water-saturated solidus is calculated at temperatures typically < 680 °C at 1.2 GPa. Muscovite is stable in either multiple fields or in a single field with a wider range of P–T.

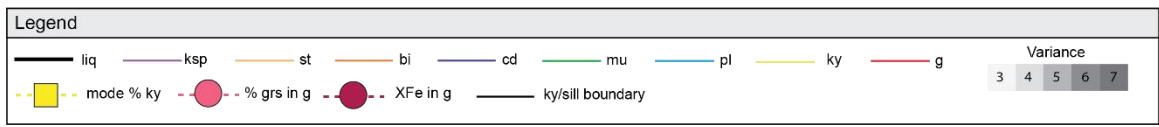
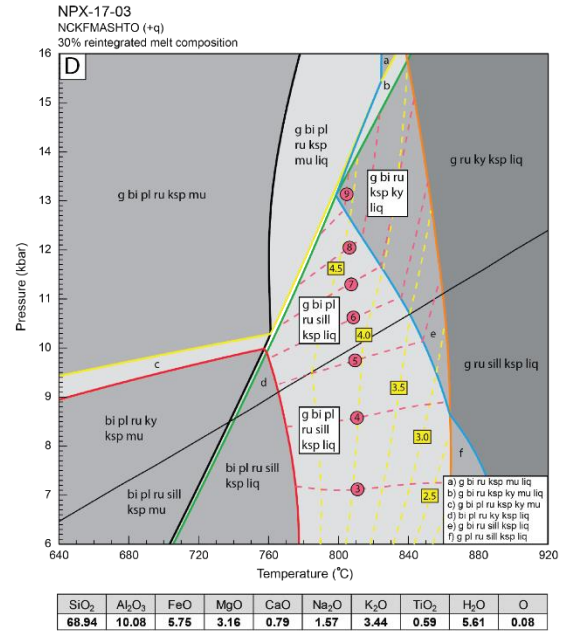
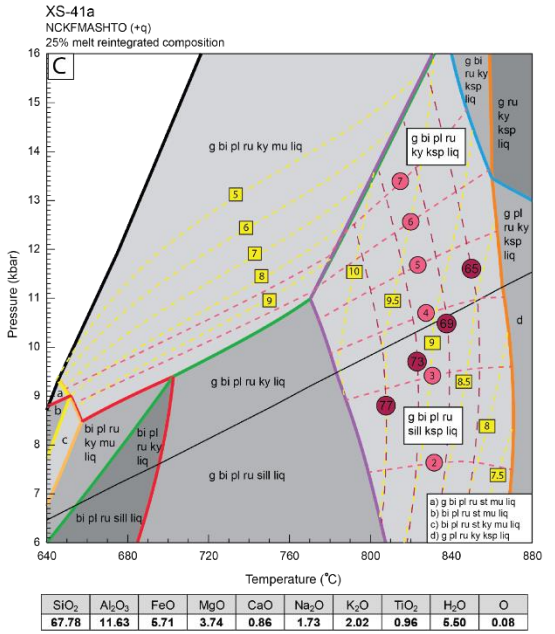
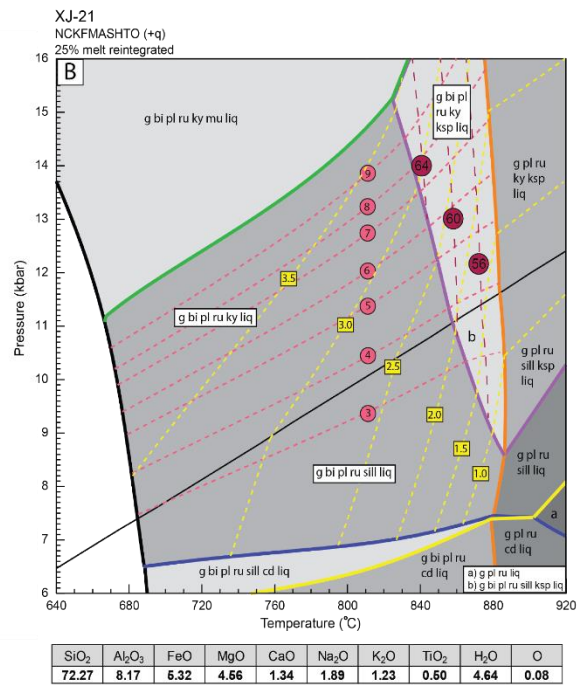
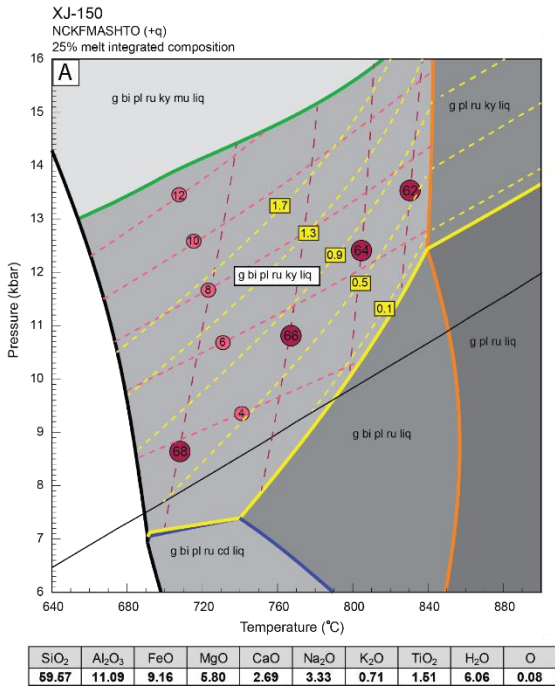


Figure 13. Pseudosections with aluminosilicate isomodes, grossular, and X_{Fe} in garnet isopleths calculated using the melt-reintegrated composition for each sample.

P–T than that in the previous set of pseudosections. Melt-reintegrated pseudosections can be divided into two groups: Group 1 consists of XJ-150 and XJ-21; and Group 2 consists of XS-41a and NPX-17-03. The pseudosections for Group 1 are primarily characterized by the muscovite stability being restricted to a single field at higher P and the appearance of aluminosilicate independent of muscovite disappearance (Figs. 13a,b). Therefore, in this group muscovite disappearance is not linked with the typical muscovite dehydration reaction:



Other common features in the pseudosections of this group include stable cordierite at low P, cordierite-out lines coinciding with sillimanite-out lines at low-P. In both pseudosections, the stability field of the assemblage $\text{g} + \text{bi} + \text{pl} + \text{ru} + \text{ky} + \text{liq}$ lies below the muscovite out-line at high P. In XJ-21 K-feldspar becomes stable at higher T , but K-feldspar is not stable in XJ-150 under the given P – T range. Group 1 pseudosections are comparable to that of an average greywacke in Yakymchuk (2017).

The pseudosections for Group 2 are characterized by muscovite stability expanding across multiple fields from low to high P (Figs. 13c,d) and limited at higher T by the reaction:



Other notable features include garnet out-lines at lower P – T , plagioclase-out lines at higher P – T . In XS-41a and at low- P in NPX-17-03A, kyanite forms before the muscovite-out reaction occurs. A notable difference between these two pseudosections is that in NPX-17-03 both K-feldspar and muscovite are stable in multiple fields, whereas in XS-41a, the two phases do not coexist as the K-feldspar-in line coincides with the muscovite-out line with increasing T . Other differences include the sizes of the kyanite-out fields, and the presence of

stable staurolite at low P – T in XS-41a. Group 2 pseudosections are comparable with the average pelite pseudosection from Yakymchuk (2017).

2.4.5.4 Isomodes and isopleths for melt-reintegrated pseudosections

For melt-reintegrated pseudosections, only isomodes of aluminosilicate and isopleths for grossular and X_{Fe} in garnet are considered here because they provide the most useful information for predicting a P – T path for the xenolith suite. In the melt-reintegrated pseudosections, aluminosilicate isomodes have a moderate to steep dP/dT gradient. In fields where muscovite is absent, the mode of aluminosilicate decreases with decreasing P and increasing T towards the biotite-out line. In Group 2 fields where muscovite is stable, modes of aluminosilicate increase with decreasing P towards the muscovite-out line. Grossular isopleths have a moderate to shallow dP/dT gradient. An exception to this is the plagioclase-absent part of Field 1 in pseudosection NPX-17-03, where grossular isopleths have a steep dP/dT gradient (Fig. 12d). Modal proportions of grossular increase with increasing P in each field of interest. X_{Fe} in garnet isopleths allow for minimum peak temperature estimates when predicting a P – T path. X_{Fe} isopleths have a steep dP/dT gradient in each sample and modal proportions decrease with increasing T towards the biotite-out line.

2.4.6 *U–Pb and Hf in zircon*

2.4.6.1 Zircon morphologies from CL imaging

One hundred and twelve zircon grains were imaged using BSE using a JEOL 7100F field-emission gun) (FEG) SEM equipped with a CL detector. Characteristic zircon images are shown in figure 14 and the full set is found in Appendix X. Zircon grains are 75–150 μm in diameter or length with distinct cores and rims separated by a sharp, ridged contact. Typically,

zircon cores are complex as some grains have inner, mid, and outer cores inferring multiple generations of growth. However, the core is generalized here as a whole because the cores are too small to date each growth generation by LASS. Zircon cores are rounded to subrounded and occasionally subangular. Most cores are either unzoned or have growth zoning and rarely have sector zoning. Zircon rims are growth zoned and typically rounded in the aluminous samples (e.g., XC-9, XJ-60, and XJ-150) and subrounded to subangular in quartzose to quartzofeldspathic samples (XJ-9 and XJ-100).

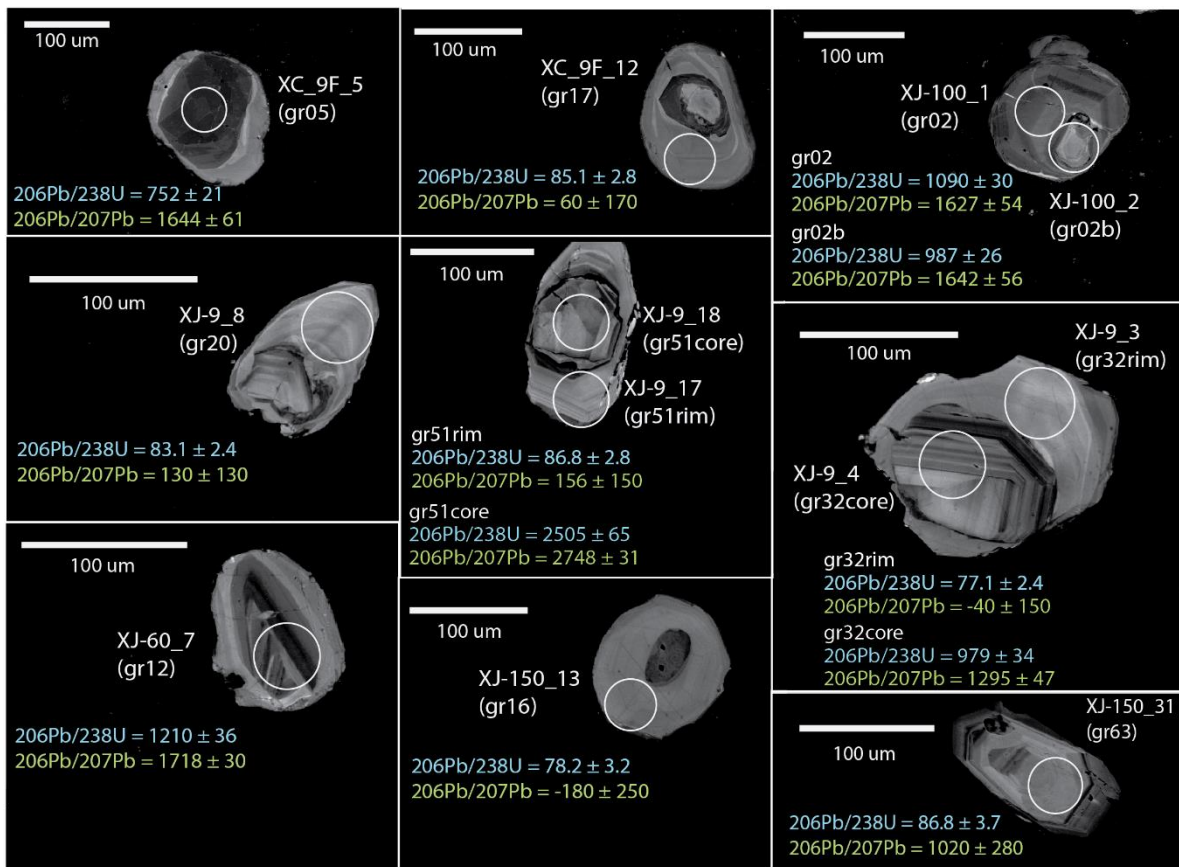


Figure 14. CL images of characteristic zircon grains. Ages are presented in Ma.

2.4.6.2 Zircon rim U–Pb dates and ϵHf

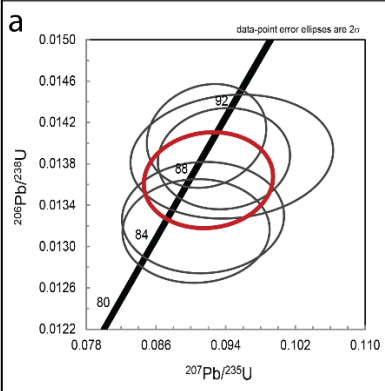
Zircon rims were analyzed to determine if U–Pb dates and Hf isotopes are consistent with the timing of crustal melting and metamorphism in the Cretaceous. Sixty analyses on zircon rims were attempted and a total of 13 were successful from xenolith samples XC-9F, XJ-9, and XJ-150. Isotopic age diagrams for rims are found in figure 15. Weighted average $^{206}\text{Pb}/^{238}\text{U}$ ages are considered the most reliable ages reported below due to analytical issues with determining the small amounts of radiogenic ^{207}Pb present at young ages. Hf isotope data is reported as an ϵHf vs. time plot for concordant zircon rims in figure 16. Data for zircon U–Pb analyses are found in Appendix XIV and data for Lu–Hf are in Appendix XV.

In xenolith sample XC-9F, there were 7 successful rim analyses out of 19. Zircon rims have two distinct concordant ages with well centered ellipses. The first older concordia age is 87.6 ± 1.8 Ma (2σ , MSDW = 1.8) on a normal Concordia diagram (Fig. 15a) and 87.8 ± 1.1 Ma (2σ , MSWD = 1.6) on an inverse concordia, Tera-Wasserburg diagram (Fig. 15b). The weighted average $^{206}\text{Pb}/^{238}\text{U}$ age for the concordant data is 87.2 ± 3.4 Ma (2σ , MSWD = 4.0) (Fig. 15c). The second, relatively younger concordia age is 71.0 ± 1.4 Ma (2σ , MSWD = 1.19). This age and MSWD is the same on both normal Concordia and Tera-Wasserburg diagrams (Fig. 15d, e). The weighted average $^{206}\text{Pb}/^{238}\text{U}$ age is 70.5 ± 1.5 (2σ , MSWD = 0.0034) (Fig. 15f). Both groups of zircon rims have low radiogenic Hf. Older zircon rims have ϵHf values projected from the concordia age of 87 Ma that range from -12.04 to -18.73 (Fig. 16). Younger rims have ϵHf values of -39.06 and -16.71 projected from the concordia age of 71 Ma.

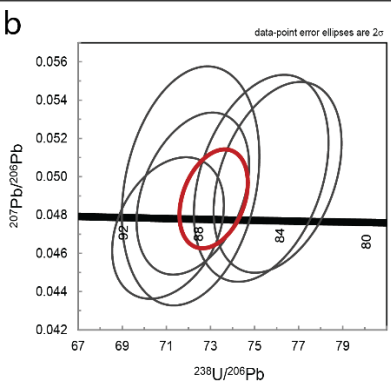
In xenolith sample XJ-9, there were 3 successful analyses out of 12. Zircon rims give a concordia age that is slightly discordant from the Concordia line. On a Concordia diagram, (Fig. 15g) rims give an age of 83.6 ± 1.3 Ma (2σ , MSWD = 4.5) and on a Tera-Wasserburg diagram, (Fig. 14h) the Concordia age is 83.2 ± 1.4 Ma (2σ , MSWD = 6.6). The weighted average $^{206}\text{Pb}/^{238}\text{U}$ age of the concordant data is 82.9 ± 1.4 Ma (2σ , MSWD = 0.29) (Fig. 15i). Rims here have low radiogenic Hf and have ϵHf values ranging from -24.93 to -26.55 with an average value of -25.68 (Fig. 16).

In xenolith sample XJ-150, there were 3 successful analyses out of 17. The zircon rims give a concordia age of 79.3 ± 1.8 Ma (2σ , MSWD = 6) in which the ellipse on the Concordia diagram is slightly off center from the Concordia line (Fig. 15j). On a Tera-Wasserburg diagram rims are discordant from the Concordia line and give a Concordia age of 79.1 ± 4.3 Ma (2σ , MSWD = 15) (Fig. 15k). The weighted average $^{206}\text{Pb}/^{238}\text{U}$ age is 77.8 ± 1.8 (2σ , MSWD = 0.69) (Fig. 15l). Radiogenic Hf is low with ϵHf values ranging from -21.01 to -18.25 with an average of -19.49 (Fig. 16).

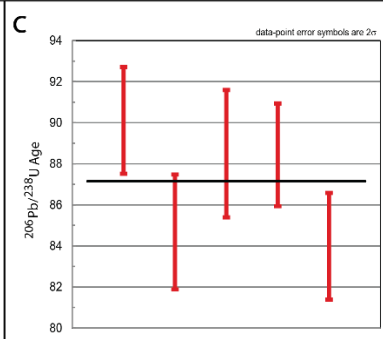
XC-9F Group A



Concordia Age = 87.6 ± 1.8 Ma,
(95% confidence, decay-const. errs included)
MSWD = 1.8, Probability = 0.17

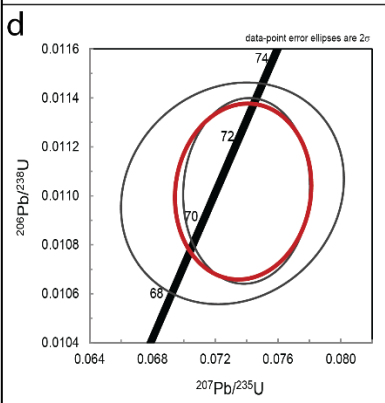


Concordia Age = 87.8 ± 1.1 Ma
(2s, decay-const. errs included)
MSWD = 1.6, Probability = 0.20

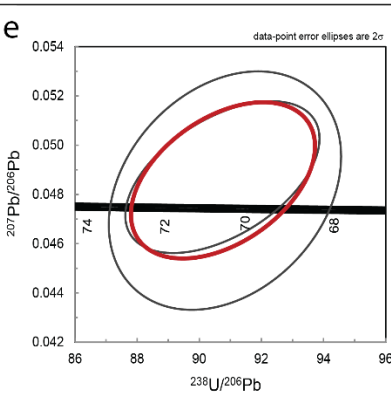


Mean = 87.2 ± 3.4 [3.9%] 95% conf.
Wtd by data-pt errs only, 0 of 5 rej.
MSWD = 4.0, probability = 0.003

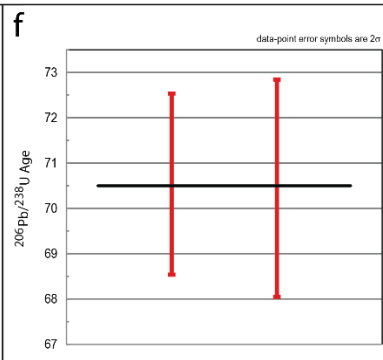
XC-9F Group B



Concordia Age = 71.0 ± 1.4 Ma
(2s, decay-const. errs included)
MSWD = 1.19, Probability = 0.28



Concordia Age = 71.0 ± 1.4 Ma
(2s, decay-const. errs included)
MSWD = 1.19, Probability = 0.28



Mean = 70.5 ± 1.5 [2.1%] 95% conf.
Wtd by data-pt errs only, 0 of 2 rej.
MSWD = 0.0034, probability = 0.95

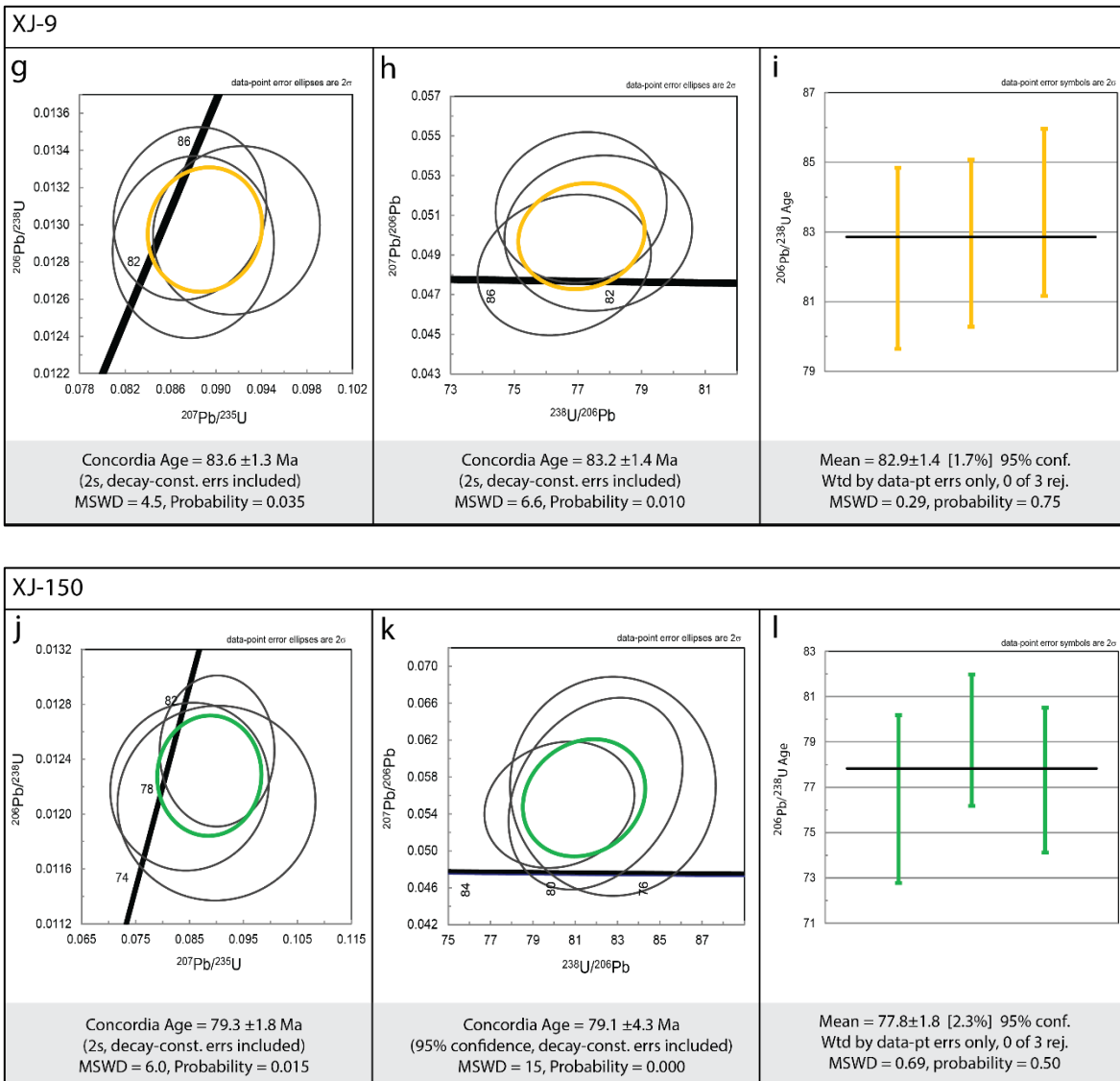


Figure 15. U–Pb isotope diagrams for zircon rims in xenoliths XC-9F, XJ-9, and XJ-150.

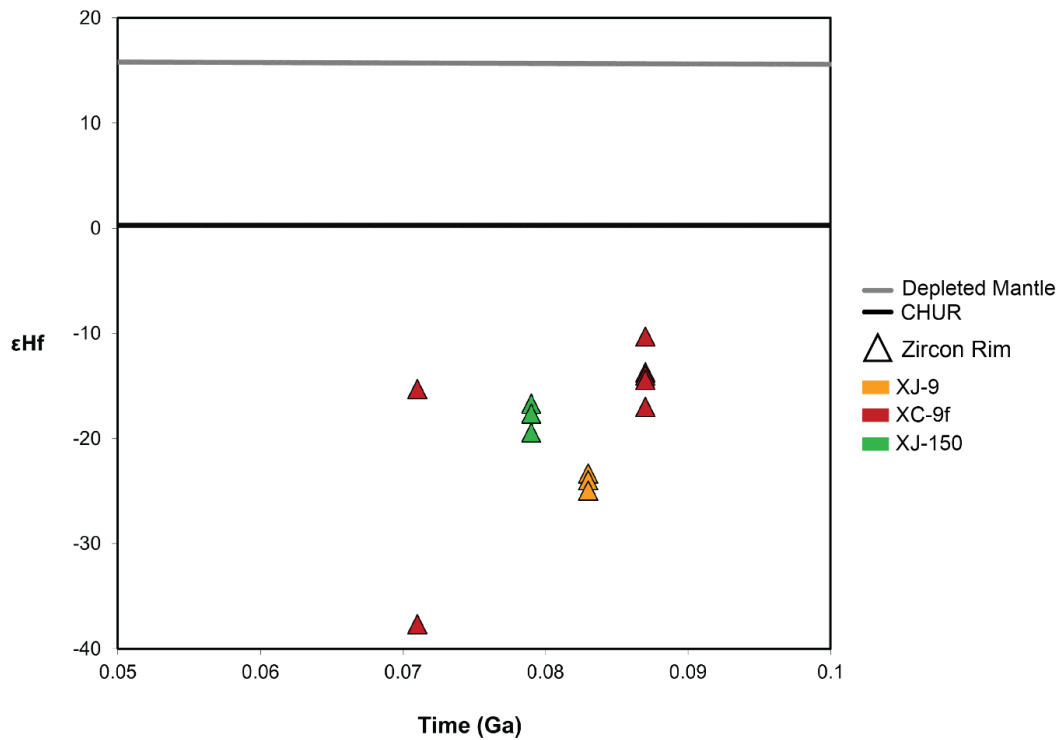


Figure 16: ϵ_{Hf} vs. time diagram for Concordant zircon rim.

2.4.6.3 Zircon core U–Pb dates and ϵ_{Hf}

Ninety-five zircon cores were analyzed to determine the initial crystallization age and the Hf isotope composition of the source that was melted that left these xenoliths behind as restite. Core ages were measured in each zircon sample; however, all ages are discordant and have high (>10) MSWD values. Errors are reported as 2σ in the age ranges and as 95% confidence intervals in weighted averages.

In xenolith zircon sample XC-9F, 15 cores were analyzed. Core $^{207}\text{Pb}/^{206}\text{Pb}$ ages range from 1258 ± 84 Ma to 1772 ± 92 Ma (Fig 17a). Zircon cores have high and low radiogenic Hf signatures with ϵ_{Hf} values ranging from -15.55 to 9.41.

Sixteen zircon cores were analyzed from XJ-9. These cores have the largest range of $^{207}\text{Pb}/^{206}\text{Pb}$ dates from 1029 ± 56 Ma to 2748 ± 31 Ma containing the youngest and oldest cores out of all the samples analyzed (Fig 17b). XJ-9 zircon cores have relatively high radiogenic Hf with ϵ_{Hf} values ranging from -0.26 to 8.18.

In XJ-150, 18 zircon cores were analyzed. Core $^{207}\text{Pb}/^{206}\text{Pb}$ ages range from 1109 ± 74 Ma to 1591 ± 74 Ma (Fig 17c). Zircon cores have relatively low radiogenic Hf with ϵ_{Hf} values ranging from -9.60 to -2.76.

Twenty-two zircon cores were analyzed in XJ-100. The $^{207}\text{Pb}/^{206}\text{Pb}$ ages range from 1571 ± 57 Ma to 1995 ± 71 Ma (Fig 17d). Radiogenic Hf in these cores is slightly low compared to the other xenolith zircon cores. ϵ_{Hf} values range from -7.75 to 1.14.

In XJ-60, 13 zircon cores were analyzed. Zircon core $^{207}\text{Pb}/^{206}\text{Pb}$ ages range from 1378 ± 91 Ma to 1990 ± 37 Ma (Fig 17e). Cores have a mix of low and high radiogenic Hf signatures. ϵ_{Hf} values range from -6.27 to 9.54.

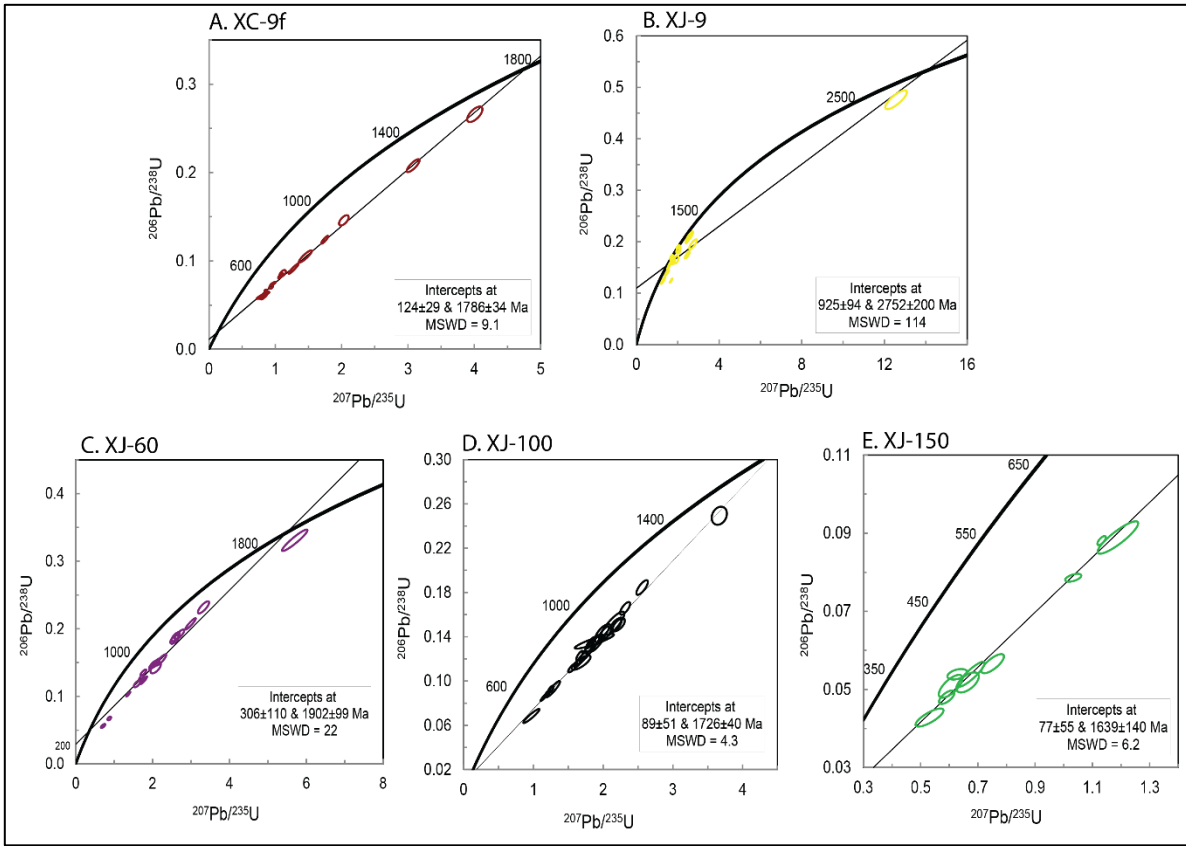


Figure 17. Concordia diagrams for xenolith zircon cores

2.4.7 U–Pb and Nd in monazite

2.4.7.1 Monazite morphologies

Forty monazite grains were imaged using BSE using a JEOL 7100F field-emission gun) (FEG) SEM. Typical images of monazite are shown in figure 18 and the full set is found in Appendix XI. Monazite grains range in diameter from 100 to 300 μm and are typically angular to subangular with rare subrounded shapes. Distinct core-rim boundaries are visible in most monazite internal structures in which the core is a darker grey than the rim. Other grains are either homogeneous or have irregular light and dark patches.

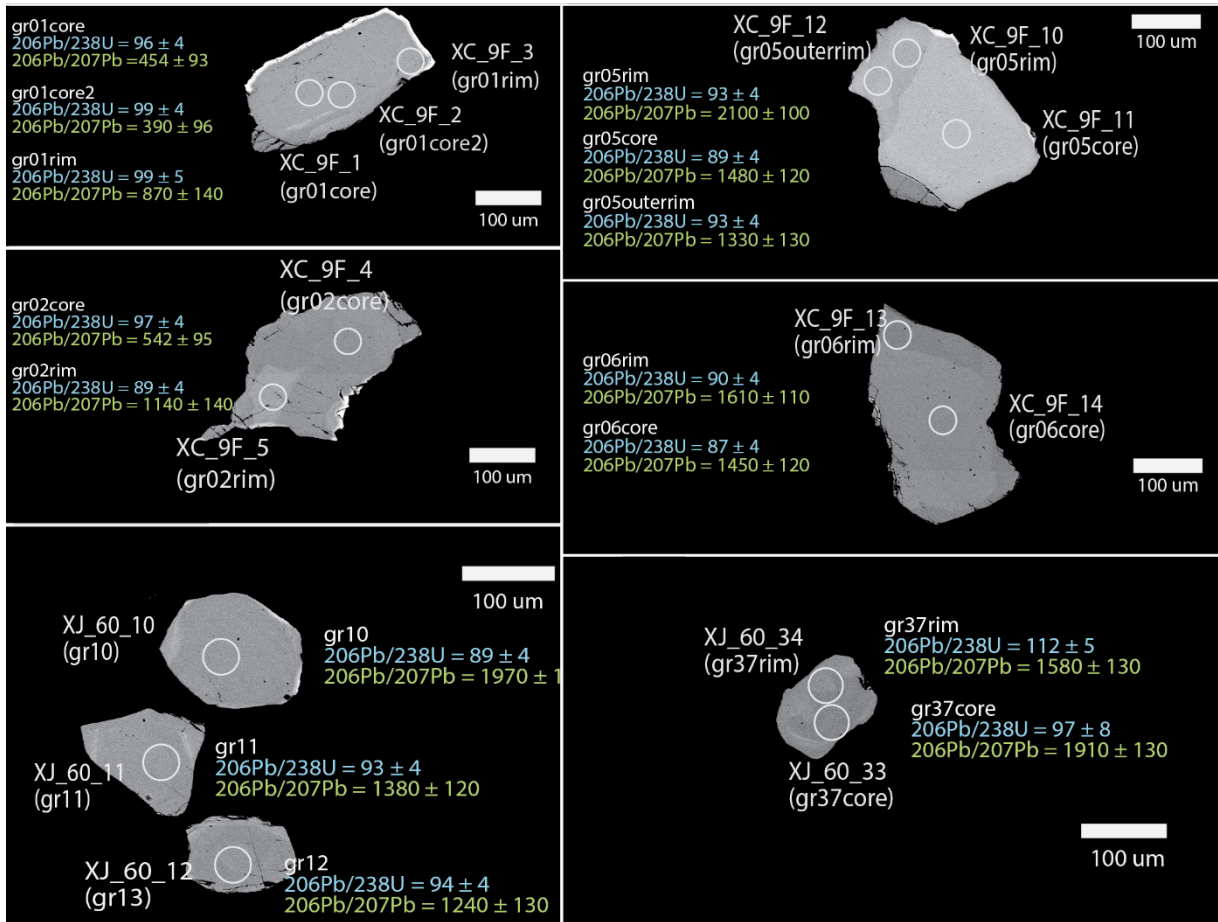


Figure 18: BSE images of characteristic monazite grains. Ages are presented in Ma.

2.4.7.2 Monazite U–Pb dates and ϵ_{Nd} ,

Monazite were analysed from xenolith samples XC-9F and XJ-60 to constrain ages and isotopic signatures consistent with crustal melting and metamorphism. Seventy-three monazite analyses were completed in total, 30 in XC-9F and 43 in XJ-60. Monazite analyses from both xenolith samples are discordant (Fig. 19). Monazite ellipses from each sample XC-9F and XJ-60 plot along a line with lower intercepts of 84.7 ± 5.6 Ma (2σ , MSWD = 5.8) and 84.0 ± 3.1 Ma (2σ , MSWD = 6.6). However, these lines are not realistic because the upper intercepts are at the age of the earth, and they don't correspond to inheritance ages. Therefore,

the lower intercept dates are questionable. The Sm–Nd isotopic data for monazite is shown on an initial ϵ_{Nd} vs time plot projected to the $^{206}\text{Pb}/^{238}\text{U}$ weighted mean age of 87.7 Ma (Fig. 20). Monazite has quite negative ϵ_{Nd} values ranging from -18.78 to -22.98 which deviate far from the CHUR line.

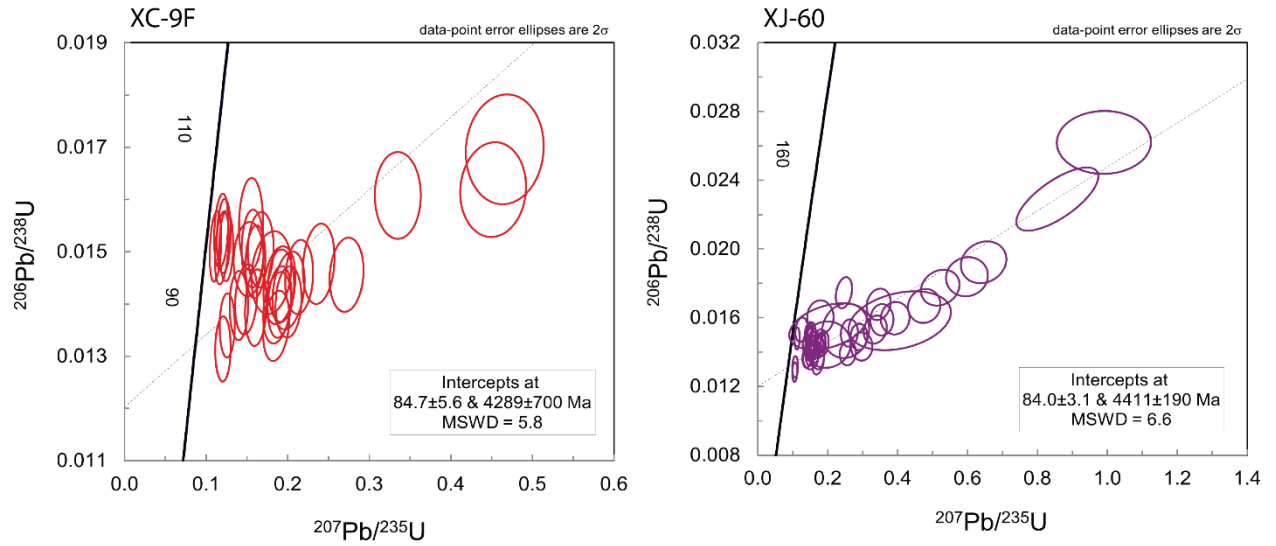


Figure 19. Monazite U-Pb isotopic ratios plotted on a Concordia diagram.

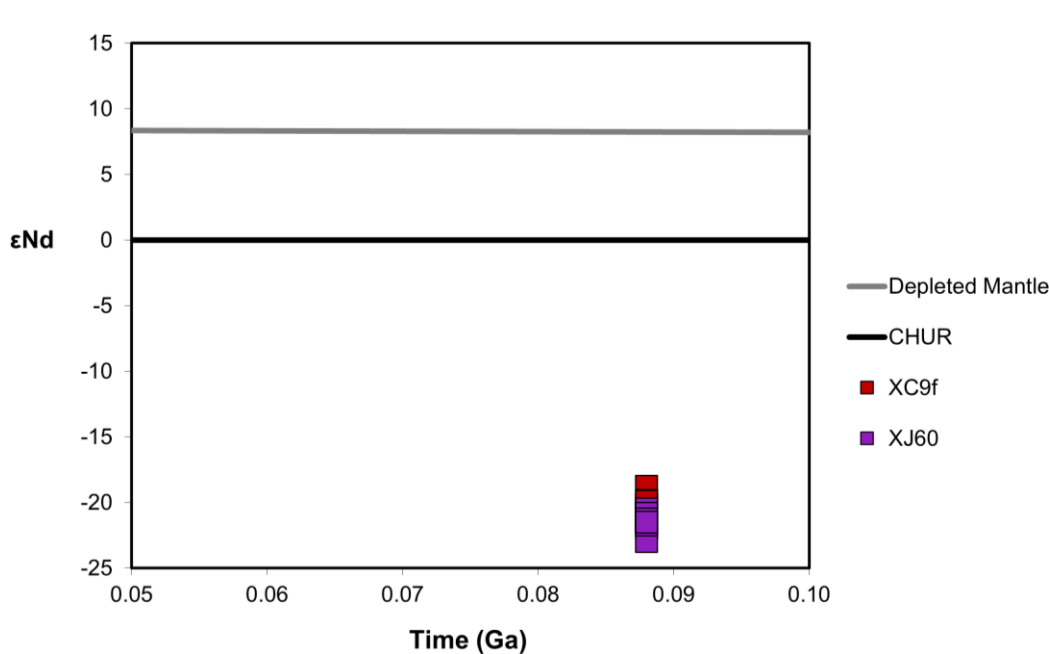


Figure 20. Initial ϵNd vs. time plot for monazite.

2.4.8 Trace elements in zircon and monazite

Trace element LA-ICP-MS analyses are reported on Chondrite-normalized REE diagrams using the Chondrite values from (Anders & Grevesse, 1989). Trace element signals were integrated using Iolite (Paton et al., 2011). The values of major elements, Hf for zircon and Ca for monazite, used in integrating trace element signals are found in Appendix XVI and XX, respectively.

2.4.8.1 Zircon

Rare earth element patterns for zircon rim analyses in sample XC-9F (Fig. 21a) follow the same trend. This trend is characterized by a positive Ce anomaly, negative La, Pr, and Eu anomalies, and flattened HREE curves. REE patterns for zircon core have a positive Ce anomaly, and negative La, Pr, and Eu like that of zircon rim. Zircon core HREE signatures

have two different trends (Fig. 21b). The most prominent HREE trend is flattened like that of the rim, and the less dominant shows a steepened, HREE enriched trend.

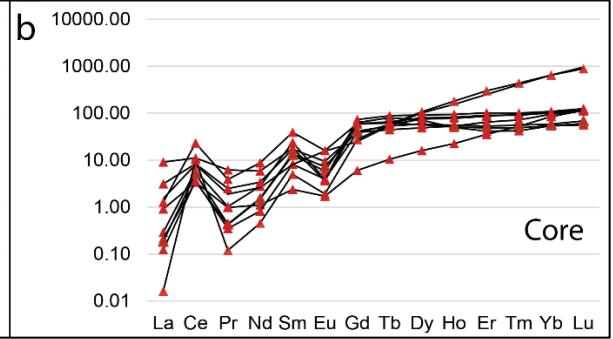
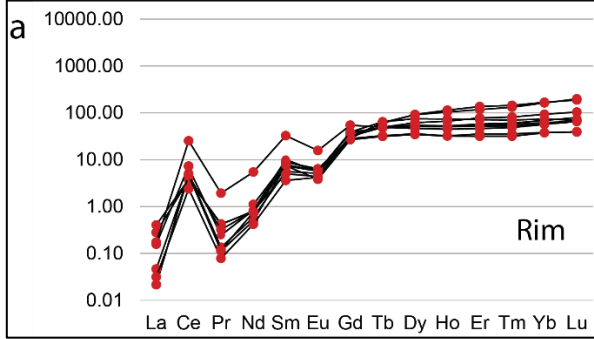
In xenolith sample XJ-9, the REE for zircon rim and core in figure 21c and d follow the same trend however, the core is slightly more scattered than the rim. Rim and core REE patterns have a positive Ce, negative La, Pr, and Eu anomalies, and a steep HREE enrichment curve. One zircon rim analysis has a less negative Pr anomaly relative to the other analyses.

Xenolith zircon rim from sample XJ-60 have positive Ce, negative La and Pr, and Eu anomalies on a REE plot (Fig. 21e). The HREE curves are flattened showing a lack of enrichment. Zircon core show the same element anomalies as the rim however, have contrasting HREE patterns (Fig. 21f). The dominant trend is a HREE curve is flattened similar to the rims, and a singular core analysis shows a HREE enrichment curve.

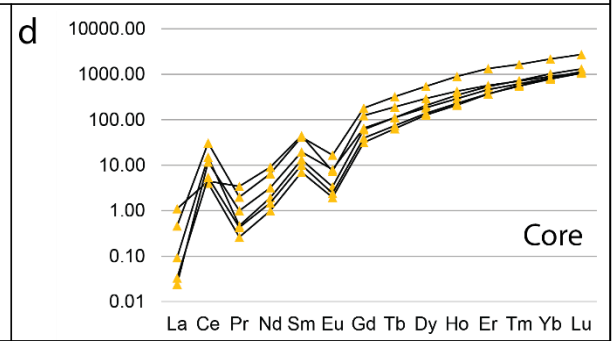
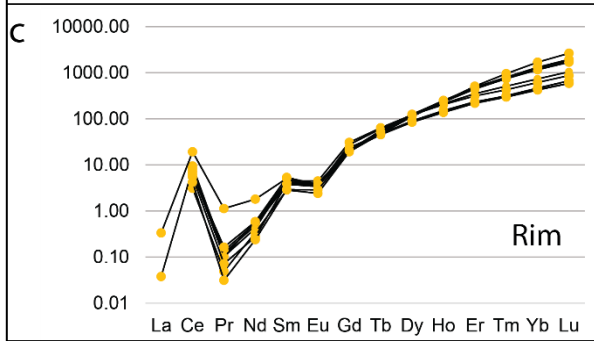
Trace element analysis was successfully collected for one zircon rim and several zircon core in xenolith sample XJ-100 (Fig. 21g and h). Both rim and core have a positive Ce, negative La and Pr, and Eu anomalies. The HREE curve for the zircon rim analysis is flat whereas the core has a slight HREE enrichment.

The REE patterns of zircon rim in xenolith zircon sample XJ-150 have a positive Ce and negative La, Pr, and Eu anomalies with a flat HREE curve (Fig. 21i). Zircon cores have positive Ce, negative La and Pr, and slightly less negative Eu anomalies (Fig. 21j). Each of the two zircon core analyses show two different HREE patterns: one being flattened, and the other is a steepened enrichment curve.

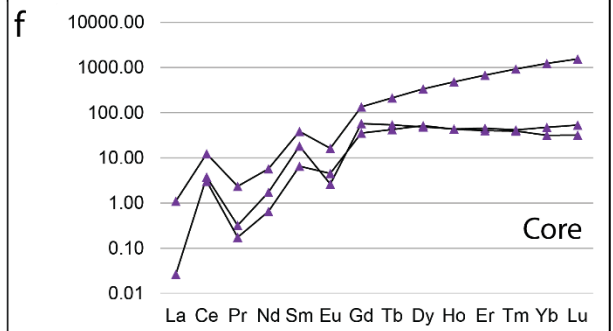
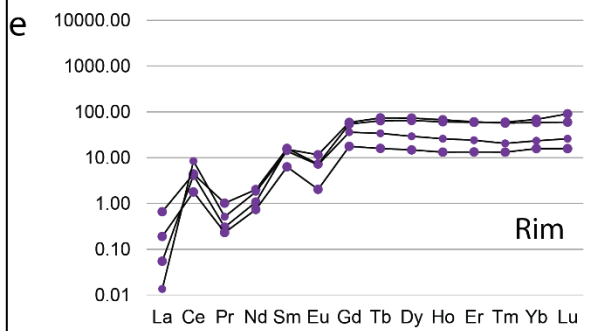
XC-9F



XJ-9



XJ-60



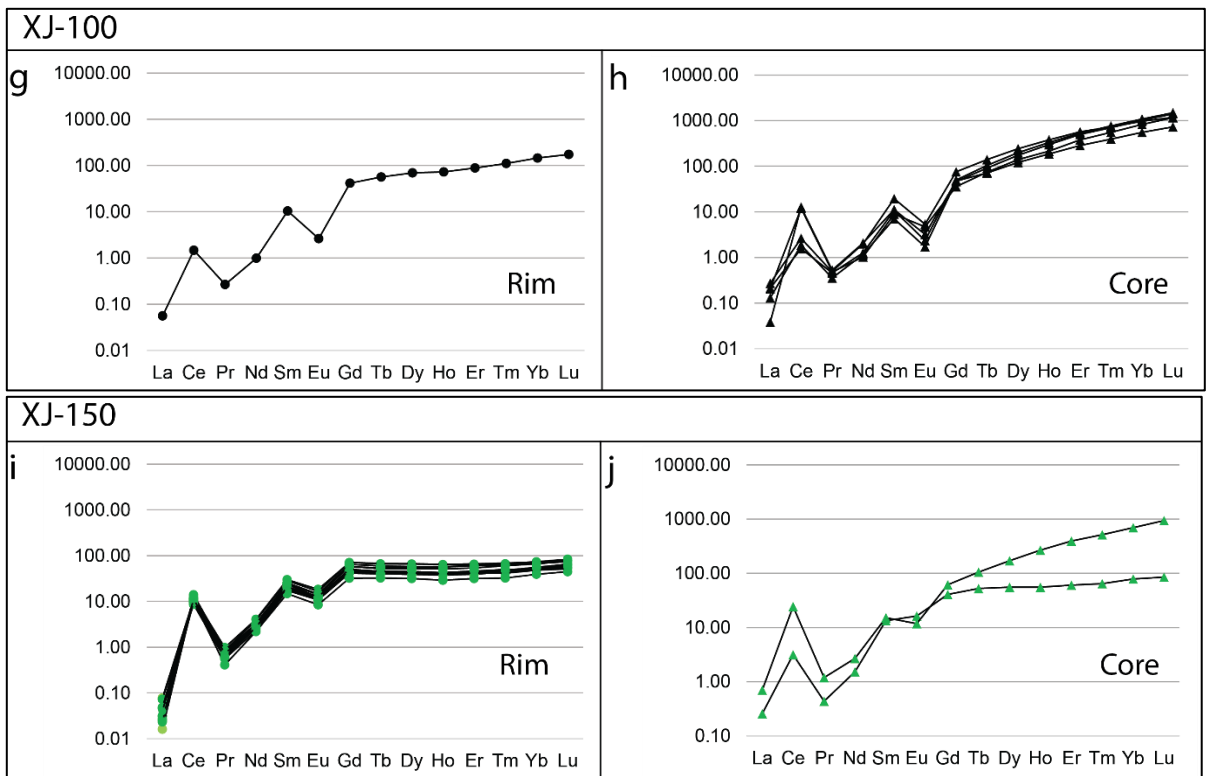


Figure 21. Chondrite-normalized REE plots for zircon rim and core.

2.4.8.2 Monazite

Rare earth element patterns in xenolith monazite from samples XC-9F and XJ-60 show the same trends on a chondrite-normalized diagram (Fig. 22). The REE curves show a steep depletion in HREE, an enrichment in LREE, and a slight negative Eu anomaly.

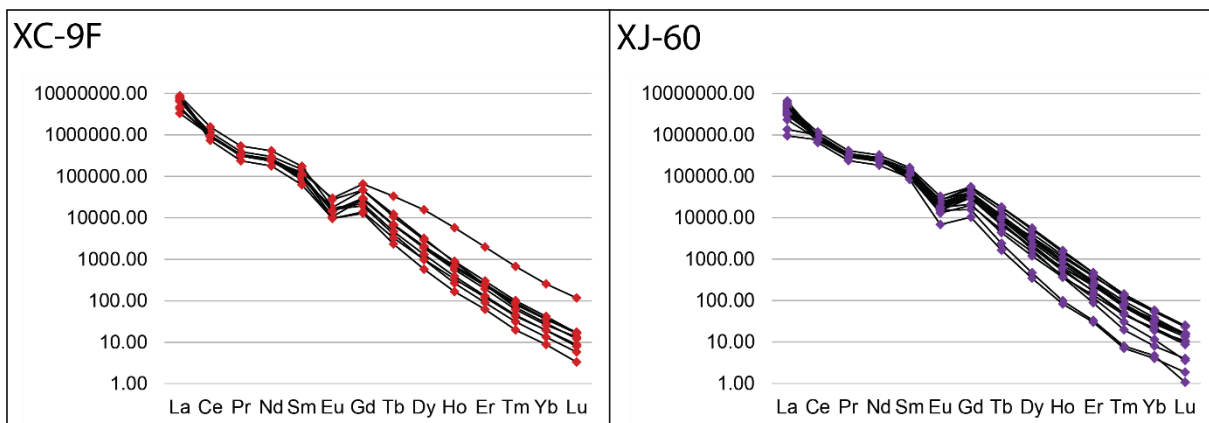


Figure 22. Monazite REE data from samples XC-9F and XJ-60 plotted on a chondrite-normalized diagram using chondrite values from Anders and Grevasse (1990).

2.5 Discussion

2.5.1 *P–T path and melt composition predictions*

P–T pseudosections calculated with actual and melt-reintegrated bulk rock composition were linked with data from mineral chemistry and microstructures to decipher the P–T evolution for the Mojave xenolith suite. The overall P–T path is inferred using the melt-reintegrated pseudosections (Fig. 23a–d). The peak P–T and retrograde path occurred after melt loss, however they can still be assessed in the melt-reintegrated pseudosections because the topology of the two sets of pseudosections (melt-reintegrated and those calculated with the actual bulk compositions of the xenoliths) is identical at conditions above the dry solidus (also shown in Figure 23). Predicted *P–T* paths will be discussed here in order of prograde, peak metamorphism, and retrograde evolution.

2.5.1.1 Prograde evolution

The trajectory of the prograde P–T path was predicted using microstructures consistent with prograde metamorphism, internal structures of aluminosilicate minerals mapped in CL, and the grossular content of garnet measured with the EPMA. The earlier stage of this path is recorded in XS-41a, where sillimanite inclusions in garnet imply that this phase was present before or during garnet growth. Therefore, the P–T path is inferred to pass through the sillimanite → kyanite boundary in the garnet absent fields at $P < 0.9$ GPa and $T < 690^{\circ}\text{C}$ (Fig. 23c). In addition, the pseudosection for sample XS-41a shows a stability field of staurolite at low P–T conditions, and that substantial amounts of kyanite formed (e.g., ~9 mode %) at T below the muscovite-out line. Therefore, the large kyanite clusters in this sample may represent the replacement of an earlier aluminous phase.

For all of the xenolith samples, the mean X_{grs} of between 5 and 6 mode % are used for P–T path predictions in P–T fields with garnet stable. These are the values measured in garnet interiors or in garnets with relatively flat zoning profiles from core to rim. This assumption is valid if garnet grew with constant grossular content but provides only an approximation if the grossular content was homogenized at the thermal peak. The grossular isopleths, representative of this value range, suggest a P–T path with a moderate positive dP/dT gradient with the path centered at the mean (Fig. 23). The portion of the prograde path thus constrained in XS-41a passes through muscovite-stable fields, and modes of aluminosilicate slightly increase crossing the muscovite-out line towards higher T (Fig. 23c). In the pseudosection of NPX-17-03, kyanite appears to mainly form by the muscovite-out reaction (see kyanite isomodes in Fig. 23d). This is consistent with the presence of large kyanite blades with relatively homogeneous internal structures in the CL maps (Fig. 5a,b). In contrast, the

prograde paths of XJ-150 and XJ-21 is inferred to pass through muscovite-absent fields and this is consistent with low (< 2 mode %) aluminosilicate proportions in these two samples. For all samples, the prograde path in all is inferred to reach, but not surpass, the biotite-out line. Along this path, isomodes of aluminosilicate decrease with increasing T towards the biotite-out reaction. This is consistent with the overall low mode % of biotite in samples XJ-21 and NPX-17-03A and the presence of resorbed kyanite and biotite in all samples.

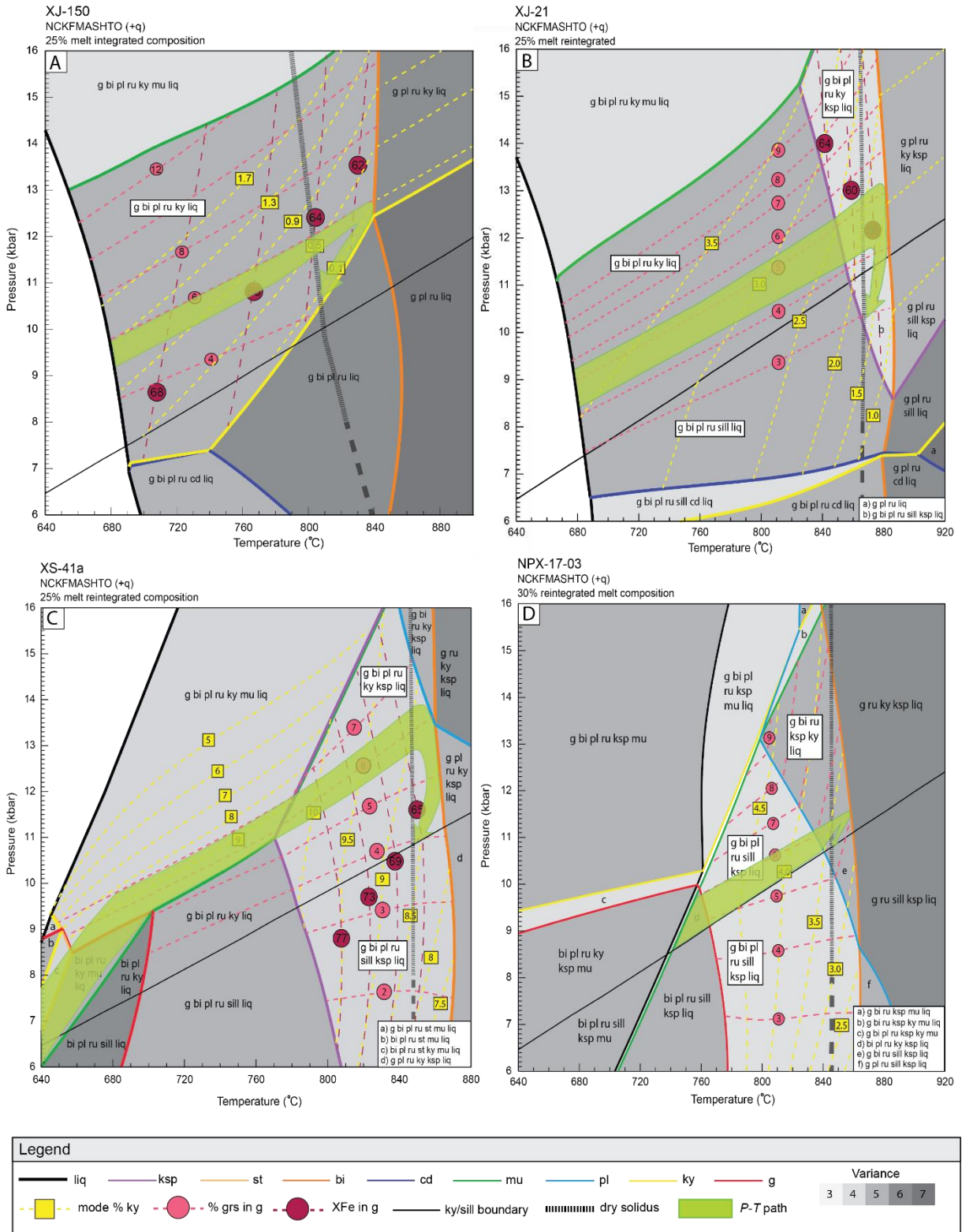


Figure 23. Predicted P–T paths for each sample overlain with melt-reintegrated pseudosections.

2.5.1.2 P–T constraints on the metamorphic peak

Peak P – T conditions are constrained by comparing modelled isopleths of X_{grs} and X_{Fe} in garnet with the measured EPMA values for these parameters. Only values from garnet interiors and relatively homogeneous, unzoned garnet grains, were considered for this. Select garnet grains show peaks of X_{grs} and X_{Fe} at the rims that are indicative of resorption and diffusion from cooling and therefore are not representative of peak P – T conditions. In the case that the composition of garnet was homogenized at peak T and continued into the early stages of cooling (Spear, 1988; 1991), the X_{Fe} , or the X_{grs} values are used here as a minimum peak- T estimates. The biotite-out line provides an additional minimum peak- T estimate due to the possibility that prograde biotite was exhausted during prograde metamorphism, as suggested by the microstructures. Based on these constraints, minimum peak T ranges from 841 – 858°C in XJ-150, 867 – 874°C in XJ-21, 842 – 862°C in XS-41a, and 847 – 859°C in NPX-17-03A along the grossular isopleths. The peak P estimate spans over grossular isopleth values of 5 and 6%. According to the ranges of measured X_{grs} values, the maximum and minimum P conditions at peak metamorphism ranges from 1.15-1.25 GPa in XJ-150, 1.1-1.3 GPa in XJ-21, 1.2-1.4 GPa in XS-41a, and 1.1-1.15 GPa in NPX-17-03. These estimated pressures are consistent with a lower crustal depth of 40–52 km which suggests that these xenoliths are from the pre-Tertiary extensional lower crust in the Mojave Desert (Coney and Harms, 1984).

2.5.1.3 Retrograde evolution

The retrograde P – T path is constrained using microstructures indicative of melt crystallization and the internal features of aluminosilicate minerals as revealed in CL in

conjunction with aluminosilicate isomodes in the field representative of the observed assemblage. For each pseudosection, this P–T path ends at the dry solidus, because sub-solidus microstructures were not observed. Late-stage kyanite overgrowths on the rims of pre-existing resorbed or corroded kyanite grains surrounded by a K-feldspar pseudomorph of former melt in sample NPX-17-03A are consistent with the retrograde path directed towards increasing aluminosilicate proportions during melt crystallisation towards the dry solidus. Additional microstructures related to melt crystallization include K-feldspar blebs adjacent to residual plagioclase and secondary carbonate, protoleucosomes of K-feldspar, and microgranophyres of plagioclase and quartz within residual or peritectic K-feldspar. In samples XJ-150, XS-41a, and NPX-17-03A the only aluminosilicate phase stable in the matrix is kyanite, meaning that the solidus was reached in the kyanite field (Figs. 23a,b,d). Sample XJ-21 provides a unique scenario in which both kyanite and late-stage sillimanite are coexisting within the matrix and are associated with partial melt crystallization microstructures such as protoleucosomes. This implies that in this sample, the last melt crystallized in the sillimanite field (Fig. 23b).

2.5.1.4 Modelled melt compositions

The chemical composition of anatectic melt produced by the xenoliths at specific P–T conditions was calculated using forward modelling with THERMOCALC (Powell & Holland, 1988) based on the pseudosection diagrams for samples XJ-150, XJ-21, and XS-41a. This was done to show how anatectic melt would evolve across different stability fields with increasing temperature conditions to better constrain the anatectic history of the xenoliths. In addition, modelled melt compositions are compared with those of Cretaceous metaluminous and peraluminous granites in the OWM region from Miller & Wooden (1994) to try to determine

if there is a source-melt connection. Melting was simulated using the melt-reintegrated compositions of samples XJ-150, XJ-21, and XS-41a at three specific settings in P–T space: 1) the water-saturated solidus where the melt volume is at its minimum; 2) muscovite disappearance (muscovite-out line); and 3) peak metamorphic temperature conditions, at the biotite-out line, where the melt volume is at its maximum. Sample NPX-17-03 was omitted from this because no water-saturated solidus was stable in the pseudosection. Each melt composition is calculated at a constant pressure of 1.25 GPa and assumes fluid absent conditions during melting (dehydration melting).

It is important to note that these compositions are not meant to be a perfect match to those of the OWM granites due to several factors that cannot be accounted for using equilibrium modelling. Those include: 1) fractional crystallization; 2) crustal assimilation; 3) interaction with entrained residual or peritectic minerals; and 4) the addition of an externally derived melt (Solar and Brown, 2001; Guernina and Sawyer, 2003; White and Powell, 2010; Taylor et al., 2014; Koblinger and Pattison, 2017). Additionally, because of inherent limitations with this kind of modeling, there is no way of knowing exactly the total amount of melt produced or lost and the number of melt loss pulses that occurred. Other studies have been done to account for open-system behaviour for partial melting (Yakymchuk & Brown, 2014; Koblinger & Pattison, 2017). However, this study only explores the modelled melt composition directly derived from the xenoliths and how it evolves in equilibrium with the residue. The modelled melt compositions are compared to the average compositions of Cretaceous metaluminous and peraluminous granites in the Mojave Desert from Miller and Wooden (1994) on binary and ternary diagrams.

On a K₂O vs. Na₂O binary diagram the melt compositions show K₂O and Na₂O wt% values to be inversely correlated (Fig. 24). Melts produced at the wet solidus have the highest Na₂O and the lowest K₂O contents (~ 7 wt. % and ~ 1 wt. %, respectively), whereas melt compositions at peak P–T are distinctively lower in Na₂O and higher in K₂O (~4–5 wt. % and ~3.5–5 wt. % respectively). Melt compositions at the muscovite-out line, depends on the pseudosection topology. Where muscovite disappears by the $\mu + \text{pl} + \text{q} \rightarrow \text{Ksp} + \text{Al}_2\text{SiO}_5 + \text{melt}$ reaction (sample XJ-41a; Fig. 23c), this composition is close to that of the peak P–T. In contrast, for sample XJ-21, in which the muscovite-out line at 12 kbars is close to the wet solidus (Fig. 23b), the calculated melt composition lies close to that of solidus. Metaluminous and peraluminous granites have K₂O and Na₂O wt. % similar to that of melt at peak metamorphism.

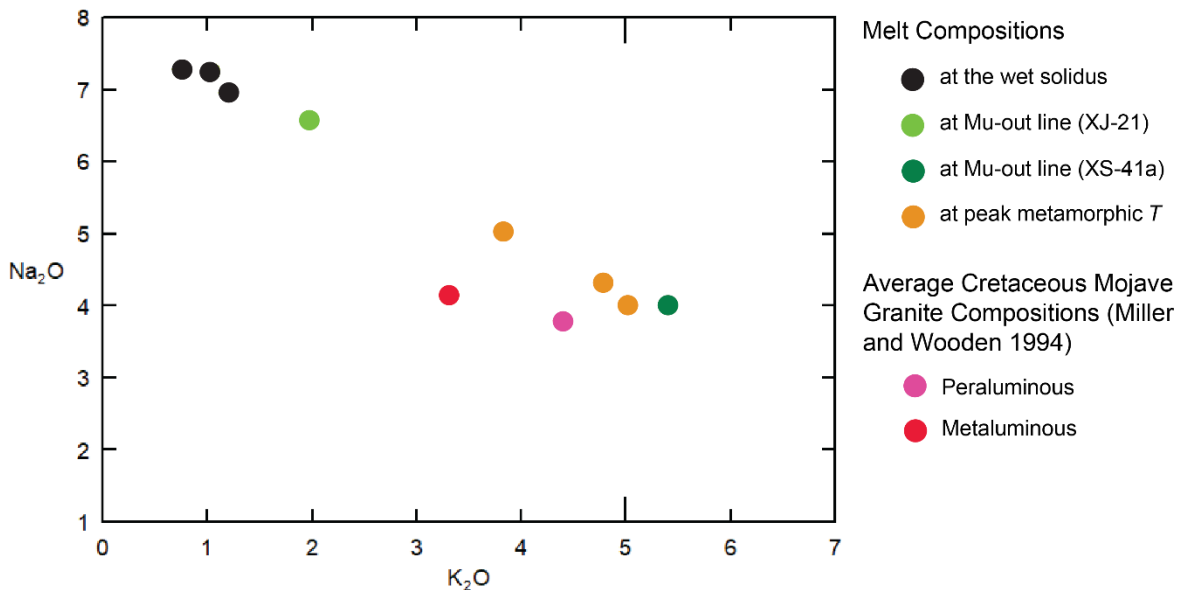


Figure 24. K₂O vs. Na₂O binary diagram for modelled anatectic melts and average Cretaceous metaluminous and peraluminous granite compositions from Miller and Wooden (1994). Oxides are in wt%.

The Na₂O+CaO vs. K₂O vs. FeO+MgO ternary diagram (Fig. 25) shows additional trends, with melt compositions at peak P–T and at the muscovite-out line for XJ-41a, having the highest FeO+MgO wt. % contents. However, the granites have distinctively higher FeO+MgO wt. % contents than any of the modelled melts.

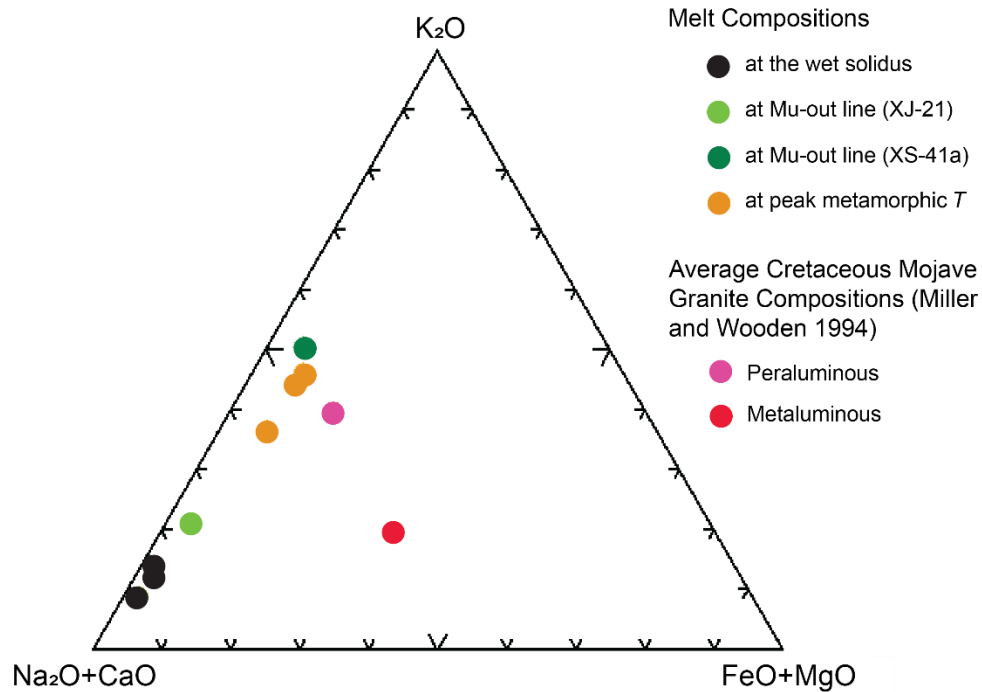


Figure 25. Na₂O+CaO vs. K₂O vs. FeO+MgO diagram in wt % oxides.

In terms of the Alumina Saturation Index (ASI) the modelled melts are classified as peraluminous (Fig. 26), and this is consistent with the peraluminous granites in the OWM region. The melts produced at peak P–T have the highest ASI values, suggesting that peraluminosity of the modelled melt compositions increases with increased melting temperature and melt volume.

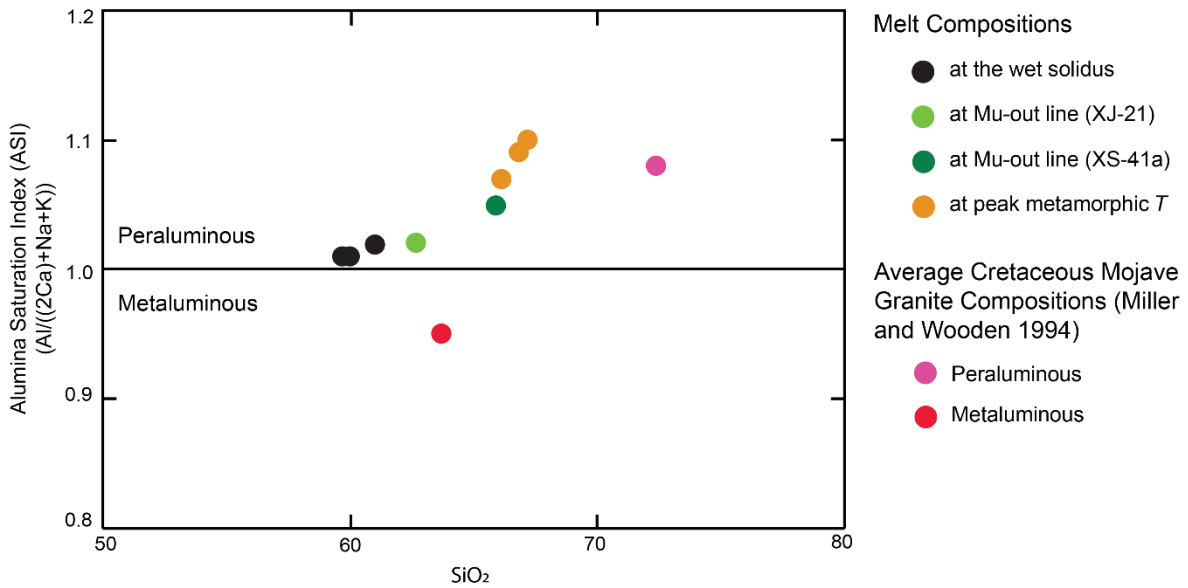


Figure 26. SiO₂ wt. % oxide vs. ASI (alumina saturation index) binary diagram modified from Frost and Frost (2008).

Normative quartz, alkali feldspar, and plagioclase, values for modelled melts are plotted on a QAP granitoid classification diagram (Fig. 27). Modelled melt compositions are for a melt phase and not a solid rock and should be treated as such. The compositions modelled at the water-saturated solidus and at peak metamorphism appear to show an evolutionary trend from quartz-diorite – quartz-monzodiorite to granodiorite and monzogranite. However, the melt composition at muscovite disappearance does not quite fit this trend as it has higher normative alkali feldspar than that at peak metamorphism.

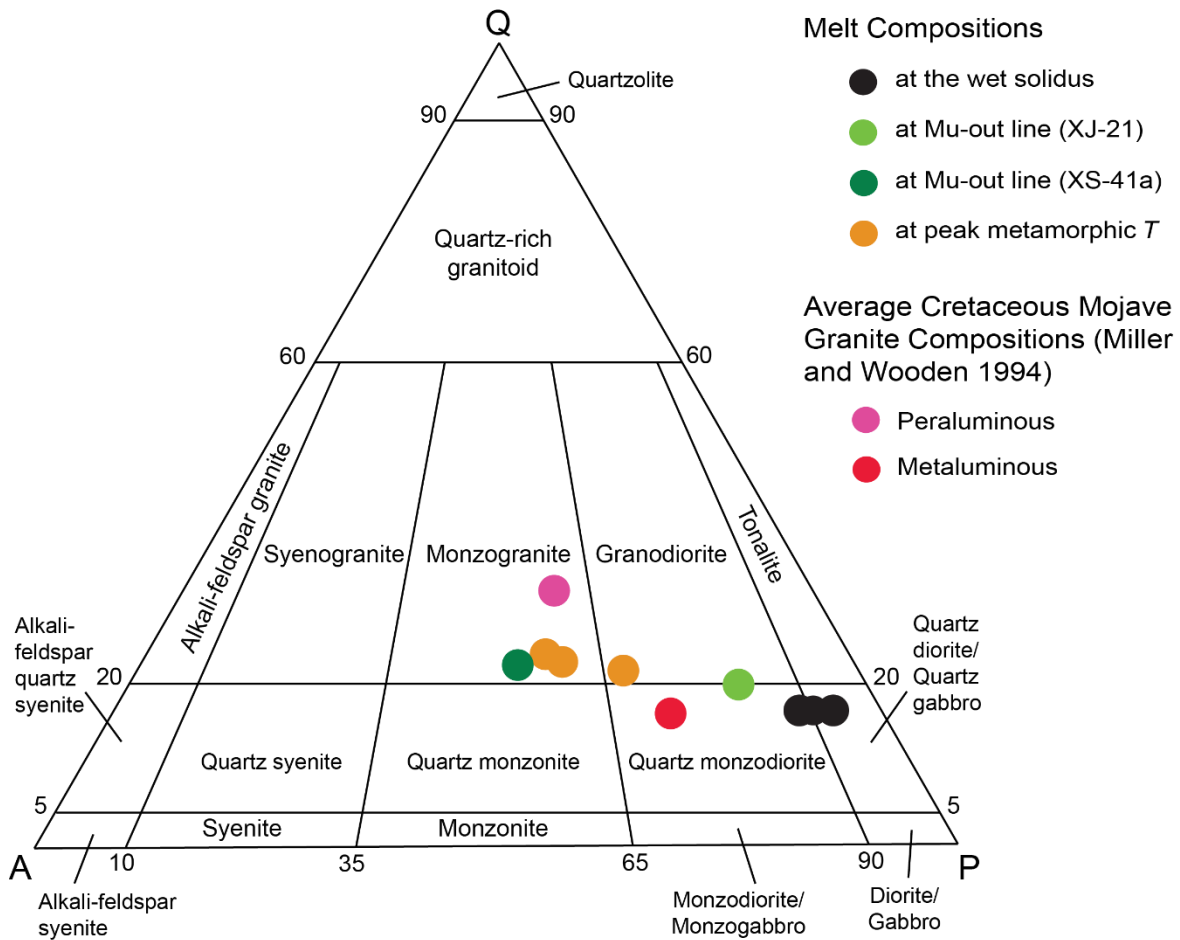


Figure 27. Normative alkali feldspar (orthoclase) vs. quartz vs. plagioclase ternary diagram with granitoid classification of plutonic rocks from International Union of Geological Sciences (IUGS). Normative mineralogy is calculated using scheme from Kelsey (1965)

Modelled anatexic melt compositions are consistent with the phase equilibria and observed microstructures linked to the consumption of muscovite and biotite from dehydration melting reactions and increasing melting temperature. The composition of <1 % volume melt produced at the wet solidus is attributed to melting of mainly quartz and plagioclase up to the

consumption of all free water. The composition of melt at the $\mu + pl + q \rightarrow Ksp + Al_2SiO_5 +$ melt reaction volume has the highest K_2O wt. % and is the most orthoclase normative.

According to the phase equilibria, the K_2O in this reaction is expected partition into the formation of peritectic K-feldspar with any remaining to partition into the anatectic melt. High K_2O contents are also characteristic of the melts modelled at peak P–T. These melts have in addition the highest $FeO+MgO$ wt. % contents, which is consistent with involvement of biotite in their production. Based on the diagrams above, the average composition of Cretaceous peraluminous granites in the OWM region best groups with anatectic melt compositions at peak metamorphism, aside from differences in SiO_2 .

2.5.2 Inheritance and Metamorphic Ages for the Mojave Xenoliths

The internal zoning and structures of zircon rims and monazite grains suggest that they grew during metamorphism or crystallization of an anatectic melt. $^{206}Pb/^{238}U$ dates are consistent with the crystallization age of metaluminous and peraluminous granites within the Old Woman Mountains region and the timing of the Laramide Orogeny (Dickinson & Snyder, 1978; Miller & Wooden, 1994; English & Johnston, 2004). Values of initial ϵ_{Hf} in zircon rims and ϵ_{Nd} in monazite are consistent with growth from an evolved melt extracted from a crustal reservoir (Hawkesworth & Kemp, 2006) and agree with those in Cretaceous peraluminous granite, the Sweetwater Wash Pluton from Fisher et al. (2017) and whole rock Nd analyses of the xenoliths from Hancher et al. (1994). The Hf and Nd isotopic compositions support the interpretation that the xenoliths represent the residue from which granitic melt was extracted, and that this melting occurred during the Laramide Orogeny.

Internal zoning and structures of zircon cores suggest that the cores were inherited from multiple sources. Rounded cores primarily in aluminous xenoliths are consistent with either dissolution in melt or sedimentary transport over long distance. Subangular cores in quartzose xenoliths suggest a shorter transport distance. Inherited zircon cores contain a spread of $^{207}\text{Pb}/^{206}\text{Pb}$ dates that are consistent with ages of detrital zircon, basement rocks, sedimentary sequences, and plutons in the region that are of Archean to Proterozoic in age (Fig. 17). The oldest zircon core age of 2748 ± 31 Ma, and those ranging between 1.9 to 1.8 Ga, can be linked with detrital zircon ages from recycled Archean and exposed Paleoproterozoic crustal components in the Mojave, respectively (Bennett & DePaolo, 1987; Barth et al., 2001; Wooden et al., 2012). Zircon cores ranging in age from 1.76 to 1.64 Ga could be related to two episodes of Paleoproterozoic crustal forming magmatism (1.79-1.73 and 1.69-1.64 Ga) and metamorphism from the Ivanpah Orogeny (Barth et al., 2000; Barth et al., 2009; Wooden et al., 2012; Duebendorfer, 2015). Dates around 1.43-1.40 Ga can be linked to Anorogenic magmatism (Anderson & Bender, 1989). The younger cores (< 1.22 Ga) are consistent with emplacement of AMCG suites (McLelland et al., 2010), anorthosite, syenite, and diabase dikes in the Mojave.

The chondrite-normalized REE patterns in the Mojave xenolith zircon rims and monazite grains are common for rocks derived from high-grade metamorphic environments (Rubatto, 2002; Whitehouse & Platt, 2003). Negative Eu anomalies have also been attributed to zircon and monazite having crystallized in a magmatic system that already had crystallized plagioclase, and thus Eu^{2+} removed from the system (Nagy et al., 2002). Depleted or flat chondrite-normalized HREE patterns observed in all monazite, the majority of zircon rims, and some zircon cores indicate growth in an HREE-depleted environment relative to LREE.

These conditions require the formation of another HREE-bearing mineral, such as garnet, or clinopyroxene, in equilibrium with or crystallizing prior to zircon crystallization (Whitehouse & Platt, 2003). This is consistent with the interpretation that U–Pb dates of zircon rims reflect timing of peak metamorphism and melting for the Pre-Tertiary extension, lower Mojave Crust. In the case of zircon cores, it is possible that grains with flat HREE patterns represent mixing of core and rim and are not representative of the Archean-Proterozoic zircon REE signatures of the Mojave lower crust. Enriched chondrite-normalized HREE patterns observed in most zircon cores, and the rims of XJ-9, are consistent with zircon growth in the absence or breakdown of another HREE-bearing phase (Schaltegger et al., 1999).

Archean - Proterozoic events linked to Mojave xenolith zircon core inheritance

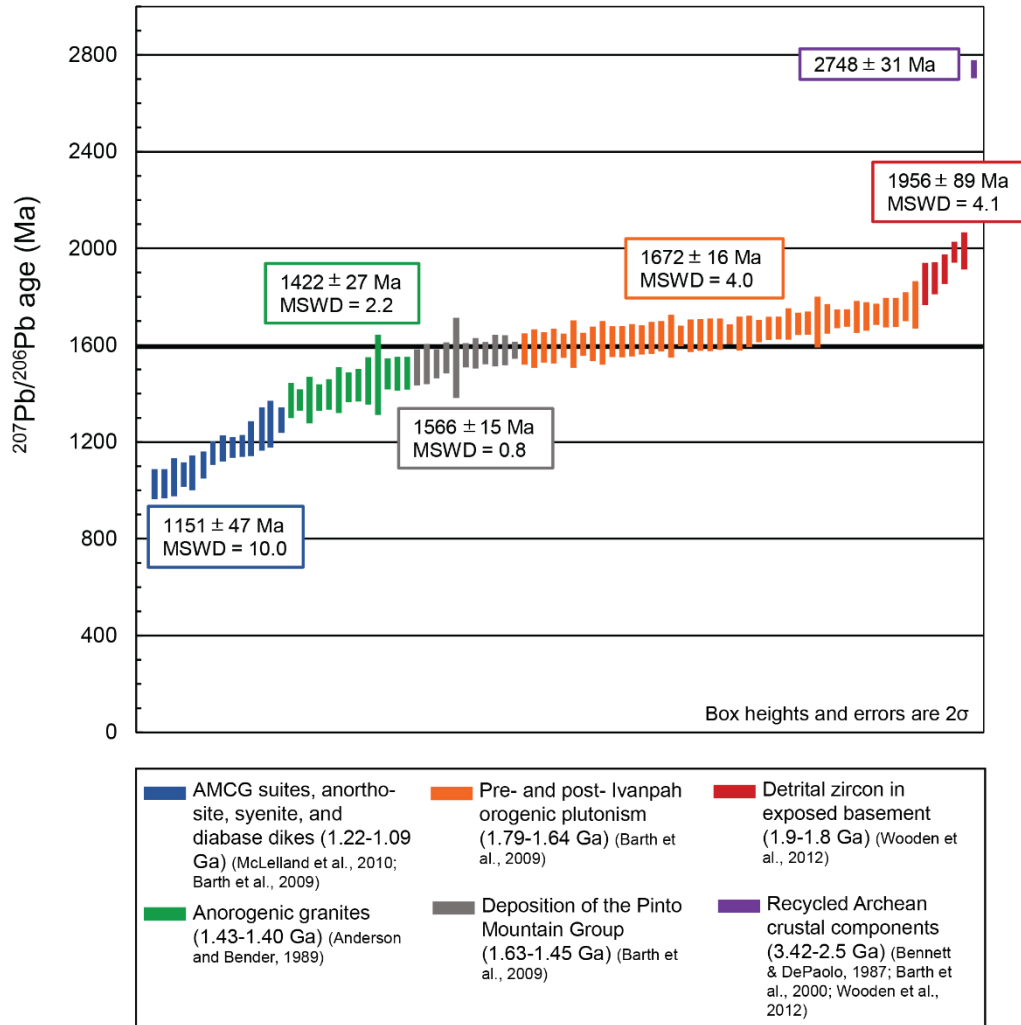


Figure 28. Zircon core $^{207}\text{Pb}/^{206}\text{Pb}$ dates plotted in age-order compared with documented Archean-Proterozoic events in the Mojave. Weighted mean dates shown in boxes are calculated from coloured data points and overlap with major geologic events known in the Mojave that occurred from the Precambrian to the Neoproterozoic.

2.6 Conclusions

The metamorphic evolution of the Mojave lower crust xenolith suite was determined in this study using detailed documentation of metamorphic microstructures, phase equilibria modelling, and simultaneous measurement U–Pb and Hf in zircon and Nd and monazite, and trace elements in zircon and monazite. This study places a particular importance on documenting metamorphic microstructures when predicting P–T history. The use of a variety of imaging techniques allows for assessment of microstructures and these are linked to mineral phases forming or breaking down. Without these imaging techniques, the predicted P–T path would not be as well constrained.

The proposed P–T–t path for the xenolith suite suggests significant melting of the pre-Tertiary extensional lower Mojave crust and this is confirmed by peak granulite facies mineralogy and phase equilibria, well-preserved metamorphic microstructures formed by melting of mica, and the growth of zircon rims and monazite from an evolved crustal melt in the late Cretaceous. The ages and trace element concentrations of zircon rims and monazite indicate that melting and peak metamorphism likely occurred during the timeframe of the Laramide Orogeny (English & Johnston, 2004)

It is difficult to confirm if an isolated suite of xenoliths is representative of an entire crustal level (Rudnick, 1992), however, the Mojave lower crustal xenolith suite paints a geologically reasonable image for the P–T–t history of the lower crust. The results from this study are consistent with, but more refined, than previous P–T estimates (Hanchar et al., 1994), depth estimates of the pre-Tertiary extensional Mojave lower crust (Coney & Harms, 1984; Bahadori et al., 2018), and the timing of magmatic and orogenic events in the Mojave

over the last 1.9 billion years (Dickinson & Snyder, 1978; Anderson & Bender, 1989; Miller & Wooden, 1994; Barth et al., 2009; McLelland et al., 2010; Wooden et al., 2012). This paper supports the idea that xenoliths are an essential component to crustal evolution studies and should be utilized to their full advantage.

References

- Anders, E., & Grevesse, N. (1989). Abundances of the elements: Meteoritic and solar. *Geochimica et Cosmochimica Acta*, 53(1), 197–214. [https://doi.org/10.1016/0016-7037\(89\)90286-X](https://doi.org/10.1016/0016-7037(89)90286-X)
- Anderson, J. L., & Bender, E. E. (1989). Nature and origin of Proterozoic A-type granitic magmatism in the southwestern United States of America. *Lithos*, 23(1–2), 19–52. [https://doi.org/10.1016/0024-4937\(89\)90021-2](https://doi.org/10.1016/0024-4937(89)90021-2)
- Bahadori, A., Holt, W. E., & Rasbury, E. T. (2018). Reconstruction modeling of crustal thickness and paleotopography of western North America since 36 Ma. *Geosphere*, 14(3), 1207–1231. <https://doi.org/10.1130/GES01604.1>
- Barth, P., Wooden, L., Coleman, D. S., & Fanning, C. M. (2000). Geochronology of the Proterozoic basement of the southwesternmost North America, and the origin and evolution of the Mojave crustal province. *Tectonics*, 19(4), 616–629
- Barth, A. P., Wooden, J. L., & Coleman, D. S. (2001). SHRIMP-RG U-Pb Zircon Geochronology of Mesoproterozoic Metamorphism and Plutonism in the Southwesternmost United States. *Journal of Geology*, 109(3), 319–327.
- Barth, A. P., Wooden, J. L., Coleman, D. S., & Vogel, M. B. (2009). Assembling and disassembling California: A zircon and monazite geochronologic framework for proterozoic crustal evolution in southern California. *Journal of Geology*, 117(3), 221–239. <https://doi.org/10.1086/597515>

- Barth, P., Wooden, L., Coleman, D. S., & Fanning, C. M. (2000). *Gabriel Mountains*. 19(4), 616–629.
- Bennett, V. C., & DePaolo, D. J. (1987). Proterozoic crustal history of the western United States as determined by neodymium isotopic mapping. *Bulletin of the Geological Society of America*, 99(5), 674–685. [https://doi.org/10.1130/0016-7606\(1987\)99<674:PCHOTW>2.0.CO;2](https://doi.org/10.1130/0016-7606(1987)99<674:PCHOTW>2.0.CO;2)
- Bright, R.M., Amato, J.M., Denyszyn, S.W. and Ernst, R.E., 2014. U-Pb geochronology of 1.1 Ga diabase in the southwestern United States: Testing models for the origin of a post-Grenville large igneous province. *Lithosphere*, 6(3), pp.135-156.
- Brown, M. (2002). Retrograde processes in migmatites and granulites revisited. *Journal of Metamorphic Geology*, 20(1), 25–40. <https://doi.org/10.1046/j.0263-4929.2001.00362.x>
- Brown, M. (2007). Crustal melting and melt extraction, ascent and emplacement in orogens: Mechanisms and consequences. *Journal of the Geological Society*, 164(4), 709–730. <https://doi.org/10.1144/0016-76492006-171>
- Brown, M. (2010). Melting of the continental crust during orogenesis: The thermal, rheological, and compositional consequences of melt transport from lower to upper continental crust. *Canadian Journal of Earth Sciences*, 47(5), 655–694. <https://doi.org/10.1139/E09-057>

- Buchan, K. L., Mertanen, S., Park, R. G., Pesonen, L. J., Elming, S. Å., Abrahamsen, N., & Bylund, G. (2000). Comparing the drift of Laurentia and Baltica in the Proterozoic: The importance of key palaeomagnetic poles. *Tectonophysics*, *319*(3), 167–198.
[https://doi.org/10.1016/S0040-1951\(00\)00032-9](https://doi.org/10.1016/S0040-1951(00)00032-9)
- Burchfiel, B. C., & Davis, G. A. (1972). Structural framework and evolution of the southern part of the Cordilleran orogen, western United States. *American Journal of Science*, *272*, 97–118.
- Caddick, M. J., Konopásek, J., & Thompson, A. B. (2010). Preservation of garnet growth zoning and the duration of prograde metamorphism. *Journal of Petrology*, *51*(11), 2327–2347. <https://doi.org/10.1093/petrology/egq059>
- Coggon, R., & Holland, T. J. B. (2002). Mixing properties of phengitic micas and revised garnet-phengite thermobarometers. *Journal of Metamorphic Geology*, *20*(7), 683–696.
<https://doi.org/10.1046/j.1525-1314.2002.00395.x>
- Coney, P. J., & Harms, T. A. (1984). Cordilleran metamorphic core complexes: Cenozoic extensional relics of Mesozoic compression. *Geology*, *12*(9), 550–554.
[https://doi.org/10.1130/0091-7613\(1984\)12<550:CMCCCE>2.0.CO;2](https://doi.org/10.1130/0091-7613(1984)12<550:CMCCCE>2.0.CO;2)
- Copeland, P., Currie, C. A., Lawton, T. F., & Murphy, M. A. (2017). Location, location, location: The variable lifespan of the laramide orogeny. *Geology*, *45*(3), 223–226.
<https://doi.org/10.1130/G38810.1>

Dickinson, W. R., & Snyder, W. S. (1978). Plate tectonics of the Laramide orogeny. *Memoir of the Geological Society of America*, 151, 355–366. <https://doi.org/10.1130/MEM151-p355>

Duebendorfer, E. M. (2015). Refining the early history of the mojave-yavapai boundary zone: Rifting versus arc accretion as mechanisms for paleoproterozoic crustal growth in southwestern laurentia. *Journal of Geology*, 123(1), 21–38. <https://doi.org/10.1086/678950>

Eaton, G. P. (1982). The Basin and Range Province: Origin and Tectonic Significance. *Annual Review of Earth and Planetary Sciences*, 10, 409–440.

English, J. M., & Johnston, S. T. (2004). The Laramide Orogeny: What Were the Driving Forces? *International Geology Review*, 46(9), 833–838. <https://doi.org/10.2747/0020-6814.46.9.833>

Fisher, C. M., Hanchar, J. M., Miller, C. F., Phillips, S., Vervoort, J. D., & Whitehouse, M. J. (2017). Combining Nd isotopes in monazite and Hf isotopes in zircon to understand complex open-system processes in granitic magmas. *Geology*, 45(3), 267–270. <https://doi.org/10.1130/G38458.1>

Foster, D. A., Miller, C. F., Harrison, T. M., & Hoisch, T. D. (1992). 40 Ar/ 39 Ar thermochronology and thermobarometry of metamorphism, plutonism, and tectonic denudation in the Old Woman Mountains area, California. *Geological Society of America Bulletin*, 104(2), 176–191. [https://doi.org/10.1130/0016-7606\(1992\)104<0176:AATATO>2.3.CO;2](https://doi.org/10.1130/0016-7606(1992)104<0176:AATATO>2.3.CO;2)

- Guernina, S., & Sawyer, E. W. (2003). Large-scale melt-depletion in granulite terranes: An example from the Archean Ashuanipi subprovince of Quebec. *Journal of Metamorphic Geology*, 21(2), 181–201. <https://doi.org/10.1046/j.1525-1314.2003.00436.x>
- Hanchar, J. M., Miller, C. F., Wooden, J. L., Bennett, V. C., & Staude, J. M. G. (1994). Evidence from xenoliths for a dynamic lower crust, eastern Mojave Desert, California. *Journal of Petrology*, 35(5), 1377–1415. <https://doi.org/10.1093/petrology/35.5.1377>
- Hawkesworth, C.J., and Kemp, A.I.S., 2006, Using hafnium and oxygen isotopes in zircons to unravel the record of crustal evolution: *Chemical Geology*, v. 226, p. 144–162, doi:10.1016/j.chemgeo.2005.09.018.
- Holland, T. J. B., & Powell, R. (1998). An internally consistent thermodynamic data set for phases of petrological interest. *Journal of Metamorphic Geology*, 16(3), 309–343. <https://doi.org/10.1111/j.1525-1314.1998.00140.x>
- Holland, T. J. B., & Powell, R. (2011). An improved and extended internally consistent thermodynamic dataset for phases of petrological interest, involving a new equation of state for solids. *Journal of Metamorphic Geology*, 29(3), 333–383. <https://doi.org/10.1111/j.1525-1314.2010.00923.x>
- Holland, T., & Powell, R. (2003). Activity-composition relations for phases in petrological calculations: An asymmetric multicomponent formulation. *Contributions to Mineralogy and Petrology*, 145(4), 492–501. <https://doi.org/10.1007/s00410-003-0464-z>

- Holness, M. B., & Sawyer, E. W. (2008). On the pseudomorphing of melt-filled pores during the crystallization of migmatites. *Journal of Petrology*, *49*(7), 1343–1363.
<https://doi.org/10.1093/petrology/egn028>
- Indares, A., White, R. W., & Powell, R. (2008). Phase equilibria modelling of kyanite-bearing anatectic paragneisses from the central Grenville Province. *Journal of Metamorphic Geology*, *26*(8), 815–836. <https://doi.org/10.1111/j.1525-1314.2008.00788.x>
- Kendrick, J., Indares, A., (2017). The reaction history of kyanite in high-P aluminous granulites. *Journal of Metamorphic Geology*, *36*, 125-146.
- Koblinger, B. M., & Pattison, D. R. M. (2017). Crystallization of heterogeneous pelitic migmatites: Insights from thermodynamic modelling. *Journal of Petrology*, *58*(2), 297–326. <https://doi.org/10.1093/petrology/egx017>
- MacRae, C. M., Wilson, N. C., & Torpy, A. (2013). Hyperspectral cathodoluminescence. *Mineralogy and Petrology*, *107*(3), 429–440. <https://doi.org/10.1007/s00710-013-0272-8>
- McLelland, J. M., Selleck, B. W., Hamilton, M. A., & Bickford, M. E. (2010). Late- to post-tectonic setting of some major proterozoic anorthosite - mangerite - charnockite - granite (AMCG) suites. *Canadian Mineralogist*, *48*(4), 729–750.
<https://doi.org/10.3749/canmin.48.4.729>

- Miller, C. F., Hanchar, J. M., Wooden, J. L., Bennett, V. C., Harrison, T. M., Wark, D. A., & Foster, D. A. (1992). Source region of a granite batholith: Evidence from lower crustal xenoliths and inherited accessory minerals. *Special Paper of the Geological Society of America*, 272, 49–62. <https://doi.org/10.1130/SPE272-p49>
- Miller, C. F., & Wooden, J. L. (1994). Anatexis, hybridization and the modification of ancient crust: Mesozoic plutonism in the Old Woman Mountains area, California. *Lithos*, 32(1–2), 111–133. [https://doi.org/10.1016/0024-4937\(94\)90025-6](https://doi.org/10.1016/0024-4937(94)90025-6)
- Mittlefehldt, D. W., & Miller, C. F. (1983). Geochemistry of the Sweetwater Wash Pluton, California: Implications for “anomalous” trace element behavior during differentiation of felsic magmas. *Geochimica et Cosmochimica Acta*, 47(1), 109–124. [https://doi.org/10.1016/0016-7037\(83\)90095-9](https://doi.org/10.1016/0016-7037(83)90095-9)
- Nagy, G., Draganits, E., Demény, A., Pantó, G., & Árkai, P. (2002). Genesis and transformations of monazite, florencite and rhabdophane during medium grade metamorphism: Examples from the Sopron Hills, Eastern Alps. *Chemical Geology*, 191(1–3), 25–46. [https://doi.org/10.1016/S0009-2541\(02\)00147-X](https://doi.org/10.1016/S0009-2541(02)00147-X)
- Otamendi, J. E., & Patiño Douce, A. E. (2001). Partial melting of aluminous metagreywackes in the Northern Sierra de Comechingones, Central Argentina. *Journal of Petrology*, 42(9), 1751–1772. <https://doi.org/10.1093/petrology/42.9.1751>
- Paton, C., Hellstrom, J., Paul, B., Woodhead, J., & Hergt, J. (2011). Iolite: Freeware for the visualisation and processing of mass spectrometric data. *Journal of Analytical Atomic Spectrometry*, 26(12), 2508–2518. <https://doi.org/10.1039/c1ja10172b>

- Powell, R., & Holland, T. J. B. (1988). An internally consistent dataset with uncertainties and correlations: 3. Applications to geobarometry, worked examples and a computer program. *Journal of Metamorphic Geology*, 6(2), 173–204.
<https://doi.org/10.1111/j.1525-1314.1988.tb00415.x>
- Rosenberg, C. L. & Handy, M. R. (2005). Experimental deformation of partially melted granite revisited: implications for the continental crust. *Journal of Metamorphic Geology*, 23(1), 19-28. <https://doi.org/10.1111/j.1525-1314.2005.00555.x>
- Rubatto, D. (2002). Zircon trace element geochemistry: Partitioning with garnet and the link between U-Pb ages and metamorphism. *Chemical Geology*, 184(1–2), 123–138.
[https://doi.org/10.1016/S0009-2541\(01\)00355-2](https://doi.org/10.1016/S0009-2541(01)00355-2)
- Rudnick, R. L. (1992). Xenoliths -- samples of the lower continental crust. In *The Continental Lower Crust* (Issue January 1992, pp. 269–316).
- Rudnick, R. L., & Taylor, S. R. (1987). The composition and petrogenesis of the lower crust: A xenolith study. *Journal of Geophysical Research: Solid Earth*, 92(B13), 13981–14005.
<https://doi.org/10.1029/jb092ib13p13981>
- Rudnick, Roberta L, & Fountain, D. M. (1995). Nature and composition of the continental crust: a lower crustal perspective. *Reviews of Geophysics*, 33(3), 267–309.
<https://doi.org/10.1029/95rg01302>

- Sawyer, E. W. (2001). Melt segregation in the continental crust: Distribution and movement of melt in anatectic rocks. *Journal of Metamorphic Geology*, 19(3), 291–309.
<https://doi.org/10.1046/j.0263-4929.2000.00312.x>
- Schaltegger, U., Fanning, C. M., Günther, D., Maurin, J. C., Schulmann, K., & Gebauer, D. (1999). Growth, annealing and recrystallization of zircon and preservation of monazite in high-grade metamorphism: Conventional and in-situ U-Pb isotope, cathodoluminescence and microchemical evidence. *Contributions to Mineralogy and Petrology*, 134(2–3), 186–201. <https://doi.org/10.1007/s004100050478>
- Solar, G. S., & Brown, M. (2001). Petrogenesis of migmatites in Maine, USA: Possible source of peraluminous leucogranite in Plutons? *Journal of Petrology*, 42(4), 789–823.
<https://doi.org/10.1093/petrology/42.4.789>
- Spear, F. S. (2014). The duration of near-peak metamorphism from diffusion modelling of garnet zoning. *Journal of Metamorphic Geology*, 32(8), 903–914.
<https://doi.org/10.1111/jmg.12099>
- Spear, Frank S., Kohn, M. J., & Cheney, J. T. (1999). P-T paths from anatectic pelites. *Contributions to Mineralogy and Petrology*, 134(1), 17–32.
<https://doi.org/10.1007/s004100050466>
- Spencer, J. E. (1985). Miocene low-angle normal faulting and dike emplacement, Homer Mountain and surrounding areas, southeastern California and southernmost Nevada (USA). *Geological Society of America Bulletin*, 96(9), 1140–1155.
[https://doi.org/10.1130/0016-7606\(1985\)96<1140:MLNFAD>2.0.CO;2](https://doi.org/10.1130/0016-7606(1985)96<1140:MLNFAD>2.0.CO;2)

- Stewart, J. H. (1972). Initial Deposits in the Cordilleran Geosyncline: Evidence of a Late Precambrian (<850 m.y.) Continental Separation. *Geological Society of America Bulletin*, 83(5)(May), 1345–1360.
- Taylor, J., Nicoli, G., Stevens, G., Frei, D., & Moyen, J. F. (2014). The processes that control leucosome compositions in metasedimentary granulites: Perspectives from the Southern Marginal Zone migmatites, Limpopo Belt, South Africa. *Journal of Metamorphic Geology*, 32(7), 713–742. <https://doi.org/10.1111/jmg.12087>
- Thompson, A. B. (1982). Dehydration melting of pelitic rocks and the generation of H₂O-undersaturated granitic liquids. In *American Journal of Science* (Vol. 282, Issue 10, pp. 1567–1595). <https://doi.org/10.2475/ajs.282.10.1567>
- Vermeesch, P. (2018). IsoplotR: A free and open toolbox for geochronology. *Geoscience Frontiers*, 9(5), 1479–1493. <https://doi.org/10.1016/j.gsf.2018.04.001>
- Vernon, R. H. (2011). Microstructures of melt-bearing regional metamorphic rocks. *Memoir of the Geological Society of America*, 207(01), 1–11. [https://doi.org/10.1130/2011.1207\(01\)](https://doi.org/10.1130/2011.1207(01))
- Vielzeuf, D., Clemens, J. D., Pin, C., & Moinet, E. (1990) Granites, granulites, and crustal differentiation. In D. Vielzeuf & PH. Vidal (Ed.) *Granulites and crustal evolution*. Kluwer Academic Publishers.

- Vielzeuf, D., & Holloway, J. R. (1988). Experimental determination of the fluid-absent melting relations in the pelitic system. *Contributions to Mineralogy and Petrology*, 98(3), 257–276. <https://doi.org/10.1007/bf00375178>
- White, R. W., & Powell, R. (2002). Melt loss and the preservation of granulite facies mineral assemblages. *Journal of Metamorphic Geology*, 20(7), 621–632. <https://doi.org/10.1046/j.1525-1314.2002.00206.x>
- White, R. W., & Powell, R. (2010). Retrograde melt-residue interaction and the formation of near-anhydrous leucosomes in migmatites. *Journal of Metamorphic Geology*, 28(6), 579–597. <https://doi.org/10.1111/j.1525-1314.2010.00881.x>
- White, R. W., Powell, R., & Clarke, G. L. (2002). The interpretation of reaction textures in Fe-rich metapelitic granulites of the Musgrave Block, Central Australia: Constraints from mineral equilibria calculations in the system. *Journal of Metamorphic Geology*, 20(1), 41–55. <https://doi.org/10.1046/j.0263-4929.2001.00349.x>
- White, R. W., Powell, R., & Holland, T. J. B. (2007). Progress relating to calculation of partial melting equilibria for metapelites. *Journal of Metamorphic Geology*, 25(5), 511–527. <https://doi.org/10.1111/j.1525-1314.2007.00711.x>
- White, R. W., Powell, R., Holland, T. J. B., & Worley, B. A. (2000). The effect of TiO₂ and Fe₂O₃ on metapelitic assemblages at greenschist and amphibolite facies conditions: Mineral equilibria calculations in the system K₂O-FeO-MgO-Al₂O₃-SiO₂-H₂O-TiO₂-Fe₂O₃. *Journal of Metamorphic Geology*, 18(5), 497–511. <https://doi.org/10.1046/j.1525-1314.2000.00269.x>

- Whitehouse, M. J., & Platt, J. P. (2003). Dating high-grade metamorphism - Constraints from rare-earth elements in zircon and garnet. *Contributions to Mineralogy and Petrology*, 145(1), 61–74. <https://doi.org/10.1007/s00410-002-0432-z>
- Wojtowicz, A. J., (1991). Luminescence of Cr³⁺ in kyanite. *Journal of Luminescence*, 50(4), 221-230.
- Wooden, J. L., Barth, A. P., & Mueller, P. A. (2012). Crustal growth and tectonic evolution of the Mojave crustal province: Insights from hafnium isotope systematics in zircons. *Lithosphere*, 5(1), 17–28. <https://doi.org/10.1130/L218.1>
- Yakymchuk, C. (2017). Applying phase equilibria modelling to metamorphic and geological processes: Recent developments and future potential. *Geoscience Canada*, 44(1), 27–46. <https://doi.org/10.12789/geocanj.2017.44.114>
- Yakymchuk, C., & Brown, M. (2014). Consequences of open-system melting in tectonics. *Journal of the Geological Society*, 171(1), 21–40. <https://doi.org/10.1144/jgs2013-039>

Chapter 3: Summary and conclusions

The Mojave lower crust xenolith suite located in the Old Woman Mountains (OWM), southeastern California, provides insight into the anatectic P–T–t history of the pre-Tertiary extensional lower Mojave crust and preserves Proterozoic inheritance linked to major crustal forming events. The metamorphic evolution of the Mojave xenolith suite was determined here using detailed documentation of metamorphic microstructures, phase equilibria modelling, and simultaneous measurement of U–Pb geochronology, radiogenic tracer isotopes and trace elements in zircon and monazite. This study places a particular importance on the interpretation of metamorphic microstructures when predicting P–T paths. The use of a variety of imaging techniques allows for microstructures to be identified in thin section and linked to minerals forming at the expense of another mineral breaking down. Without these imaging techniques, the predicted P–T path would not be as well constrained. The proposed P–T–t history for the xenolith suite suggests significant melting of the pre-Tertiary extensional lower crust inferred from well-preserved metamorphic microstructures formed by melting of mica and the growth of zircon rim and monazite from an evolved, likely peraluminous, crustal melt in the late Cretaceous. The U–Pb dates obtained, the Hf isotope composition of zircon rims, and the Nd isotopic composition of monazite grains, and the trace element concentrations of zircon rims and monazite indicate that melting and peak metamorphism likely occurred during the timeframe of the Laramide Orogeny (English & Johnston, 2004). Melt produced in the lower crust is expected to segregate to the upper crustal levels leading to the formation of peraluminous and possibly metaluminous granites in the OWM. Initial ϵ_{Hf} and ϵ_{Nd} from zircon rims and monazite grains, respectively, are consistent with that from the Sweetwater Wash Pluton granite (Fisher et al., 2017). Lost melt compositions modelled at peak metamorphism

are expected to produce peraluminous monzogranites like those of Cretaceous granites in the OWM including Sweetwater Wash Pluton (Mittlefehldt & Miller, 1983; Miller & Wooden, 1994).

It is difficult to confirm if a suite of xenoliths is representative of an entire crustal level (Rudnick, 1992), however, the Mojave xenolith suite paints a geologically reasonable image for the P–T–t history of the lower crust in that part of the Mojave in southeastern California. The results from this study are consistent, but more refined, with previous P–T constraints (Hancher et al., 1994) depth estimates of the pre-Tertiary extensional Mojave lower crust (Coney & Harms, 1984; Bahadori et al., 2018) and the timing of magmatic and orogenic events in the Mojave over the last 1.9 billion years (Dickinson & Snyder, 1978; Anderson & Bender, 1989; Miller & Wooden, 1994; Barth et al., 2009; McLelland et al., 2010; Wooden et al., 2012). This study emphasizes the importance of studying lower crustal xenoliths when constraining lower crustal evolution and they should be utilized to their full potential.

References

- Anderson, J. L., and Bender, E. E. (1989). Nature and origin of Proterozoic A-type granitic magmatism in the southwestern United States of America. *Lithos*, 23(1–2), 19–52. [https://doi.org/10.1016/0024-4937\(89\)90021-2](https://doi.org/10.1016/0024-4937(89)90021-2).
- Bahadori, A., Holt, W. E., and Rasbury, E. T. (2018). Reconstruction modeling of crustal thickness and paleotopography of western North America since 36 Ma. *Geosphere*, 14(3), 1207–1231. <https://doi.org/10.1130/GES01604.1>.
- Barth, A. P., Wooden, J. L., Coleman, D. S., and Vogel, M. B. (2009). Assembling and disassembling California: A zircon and monazite geochronologic framework for Proterozoic crustal evolution in southern California. *Journal of Geology*, 117(3), 221–239. <https://doi.org/10.1086/597515>.
- Coney, P. J., and Harms, T. A. (1984). Cordilleran metamorphic core complexes: Cenozoic extensional relics of Mesozoic compression. *Geology*, 12(9), 550–554. [https://doi.org/10.1130/0091-7613\(1984\)12<550:CMCCCE>2.0.CO;2](https://doi.org/10.1130/0091-7613(1984)12<550:CMCCCE>2.0.CO;2).
- Dickinson, W. R., and Snyder, W. S. (1978). Plate tectonics of the Laramide orogeny. *Memoir of the Geological Society of America*, 151, 355–366. <https://doi.org/10.1130/MEM151-p355>.
- English, J. M., and Johnston, S. T. (2004). The Laramide Orogeny: What Were the Driving Forces? *International Geology Review*, 46(9), 833–838. <https://doi.org/10.2747/0020-6814.46.9.833>.

- Fisher, C. M., Hanchar, J. M., Miller, C. F., Phillips, S., Vervoort, J. D., and Whitehouse, M. J. (2017). Combining Nd isotopes in monazite and Hf isotopes in zircon to understand complex open-system processes in granitic magmas. *Geology*, 45(3), 267–270.
<https://doi.org/10.1130/G38458.1>.
- Hanchar, J. M., Miller, C. F., Wooden, J. L., Bennett, V. C., and Staude, J. M. G. (1994). Evidence from xenoliths for a dynamic lower crust, eastern Mojave Desert, California. *Journal of Petrology*, 35(5), 1377–1415. <https://doi.org/10.1093/petrology/35.5.1377>.
- McLelland, J. M., Selleck, B. W., Hamilton, M. A., and Bickford, M. E. (2010). Late- to post-tectonic setting of some major Proterozoic anorthosite - mangerite - charnockite - granite (AMCG) suites. *Canadian Mineralogist*, 48(4), 729–750.
<https://doi.org/10.3749/canmin.48.4.729>
- Miller, C. F., and Wooden, J. L. (1994). Anatexis, hybridization and the modification of ancient crust: Mesozoic plutonism in the Old Woman Mountains area, California. *Lithos*, 32(1–2), 111–133. [https://doi.org/10.1016/0024-4937\(94\)90025-6](https://doi.org/10.1016/0024-4937(94)90025-6).
- Mittlefehldt, D. W., and Miller, C. F. (1983). Geochemistry of the Sweetwater Wash Pluton, California: Implications for “anomalous” trace element behavior during differentiation of felsic magmas. *Geochimica et Cosmochimica Acta*, 47(1), 109–124.
[https://doi.org/10.1016/0016-7037\(83\)90095-9](https://doi.org/10.1016/0016-7037(83)90095-9).
- Rudnick, R. L. (1992). Xenoliths -- samples of the lower continental crust. In *The Continental Lower Crust* (Issue January 1992, pp. 269–316).

Wooden, J. L., Barth, A. P., and Mueller, P. A. (2012). Crustal growth and tectonic evolution of the Mojave crustal province: Insights from hafnium isotope systematics in zircons.

Lithosphere, 5(1), 17–28. <https://doi.org/10.1130/L218.1>.